UNIVERSITY OF OKLAHOMA

GRADUATE COLLEGE

INTEGRATION OF SURFACE SEISMIC, MICROSEISMIC, AND PRODUCTION LOGS FOR SHALE GAS CHARACTERIZATION: METHODOLOGY AND FIELD APPLICATION

A THESIS

SUBMITTED TO THE GRADUATE FACULTY

in partial fulfillment of the requirements for the

Degree of

MASTER OF SCIENCE

By

JOHN HENRY ALZATE BUITRAGO
Norman, Oklahoma
2012

INTEGRATION OF SURFACE SEISMIC, MICROSEISMIC, AND PRODUCTION LOGS FOR SHALE GAS CHARACTERIZATION: METHODOLOGY AND FIELD APPLICATION

A THESIS APPROVED FOR THE
MEWBOURNE SCHOOL OF PETROLEUM AND GEOLOGICAL ENGINEERING

BY

Dr.Deepak Devegowda, Chair

Dr.Kurt J. Marfurt

Dr.Chandra Rai

Acknowledgements

I would like to thank Dr Deepak Devegowda for his invaluable advice and continued support during my time at OU. I feel honored to have had such a great adviser. Thanks for all the effort devoted towards this project.

To Dr Kurt Marfurt, my most sincere gratitude not only for being part of my committee but for adopting me in his research group and having managed to get this privileged data set. I feel lucky for having had the chance of working under your supervision.

My acknowledgements to Dr. Chandra Rai; School director and member of my thesis committee. Your leadership has found a way to help keep our school within the top ranked Petroleum Engineering Schools.

To Roderick Perez, thanks a lot for providing the 3D seismically inverted products used throughout the thesis and always being open to discuss any technical question that arose during the research.

I especially want to thank the people at DEVON Energy for releasing this unique data set that lead to an exciting research study.

The seismic interpretation, the production log analysis and microseismic analysis were done using Petrel provided to OU by Schlumberger.

The prestack seismic inversion was done using Hampson-Rusell software provided by CGGVeritas.

To all the staff and faculty from CPSGG and MPGE, particularly those that I had the privilege of receiving classes from and/or interact with. Definitely, the professionalism that characterizes all the College of Earth and Energy team have made my stay in Norman quite more pleasant and rewarding.

To the amazing people at the Oklahoma Petroleum Information Center (OPIC): Vy, Gene, Jon, and Angel, thank you very much for welcoming and having had me during a full school year as your job mate. The friendship we started during those days is going to be a lifelong relationship.

I am always thankful to life for having been given the most wonderful family in the world. Parents and siblings! Your continuous support has encouraged me to pursue my dreams.

Not the least at all…! Thanks Paula for being a great support and motivation!

Table of Contents

Acknowledgements iv

List of Tables viii

List of Figures ix

Abstract xix

Chapter 1 1

Introduction 1

Barnett Shale Petrophysics 4

Chapter 2 7

Geology of the Barnett Shale 7

Geological Setting 10

Stratigraphy 14

Chapter 3 16

Overview of Available Field Data 16

Production Logs 19

Seismic Data 22

Microseismic Data: Monitoring the Hydraulic Fracture Process 26

Microseismic Data Available 29

Chapter 4 37

Chapter 5 49

Methodology 49

Results and Analysis 54

Conclusions 73

References 75

Appendix A: MATLAB Code 82

Appendix A1: Reading the Data 82

Appendix A2: Filtering the Data 83

"NaN" Cleaning 83

Distance calculation and partitioning the data. 85

Removing data below the viewing limit 92

Appendix A3: Exporting the Data 99

Appendix B: Geologic Time Scale 101

List of Tables

Table 1. General petrophysical characteristics of petro-types identified on the basis of core measurements (Kale, 2009). 5

Table 2. Inventory of data used in this thesis. 18

Table 3. Acquisition parameters used to allow subsequent azimuthal processing. From Thompson (2010). 23

Table 4. Summary of microseismic viewing limit and list of the corresponding figures for each stimulated well. 39

Table 5. Gas production rate per well and perforation. The colored cells are following the reservoir quality classification proposed. 70

List of Figures

Figure 1. Average porosity, average total organic carbon (TOC), and average calcite content of the three petrotypes defined by Kale et al., 2010a, 2010b. 5

Figure 2. Location of the Mississippian Barnett Shale, Fort Worth Basin, showing the major geological features that influence the Barnett Shale and structural contours. The main producing area of the Newark East field is indicated by darker shading. Contours are drawn on top of the Ordovician Ellenburger Group; contour intervals equal 1,000 feet. Bruner and Smosna (2011). 8

Figure 3. North-south and west-east cross sections through the Fort Worth Basin illustrating the structural position of the Barnett Shale between the Muenster Arch, Bend Arch, and Llano Uplift. Bruner and Smosna (2011). 9

Figure 4. Location of Mississippian Barnett Shale, Fort Worth Basin. The top right square details a zoom in to the area of study, green circle. Modified from Bruner and Smosna (2011). 10

Figure 5. Regional paleogeography of the southern mid-continent region during the Late Mississippian (325 Ma), showing the approximate position of the Fort Worth Basin. Modified from Blakey (2005) Loucks and Ruppel (2007)...................... 11

Figure6. Middle Mississippian paleogeographic map of the United States indicating that the Fort Worth Basin was relatively deep. Modified from Gutschick and Sandberg (1983), Loucks and Ruppel (2007).. 12

Figure 7. Thickness of Barnett Shale, isopach lines in red, contour interval equals 50 and 100 ft. Line A-A’ marks the approximate axis of deposition. Modified from Barnett Shale Maps, 2007; Bruner and Smosna (2011). 13

Figure 8. General stratigraphy of the Ordovician to Pennsylvanian section in the Fort Worth Basin. (A) Diagrammatic cross section of the stratigraphy of the Fort Basin after Montgomery et al. (2005). (B)Wire-line log with major stratigraphic units. (Modified from Loucks and Ruppel, 2007) 15

Figure 9. Differential gas production (MSCF/d) indicated by the color and diameter of the discs along the wellbores. The background is a depth slice matching the depth at which Well B is completed of a seismic attribute called ant-tracked coherence. Ant track is particularly well suited to detect discontinuities in the subsurface. 21

Figure 10. Top view of wells showing the temperature along the horizontal section of the four parallel horizontal wells drilled in the Lower Barnett Shale. 22

Figure 11. Sketch of a typical configuration of treatment and monitoring wells during a hydraulic fracture monitoring process. The data collected at the monitoring well are processed to determine the azimuth and distance from the receiver to the acoustic emission. (Bennett et al., 2006). 28

Figure 12. Depth slice (8090 ft.) of ant tracked coherence. Monitor (vertical) and treatment (horizontal) wells completed in the Lower Barnett Shale are displayed along with the microseismic data recorded during the hydraulic fracturing. Microseismic events are colored according to their stage. 31

Figure 13. Location of the microseismic events recorded during the hydraulic fracturing process of Wells A, B, C, and D. The size of the dots is proportional to the event magnitude and the color represents the fracture stage during which they were recorded. The figure also shows the location of the monitoring wells. Well V174

served as the monitor well for Well A and Well C while Well V33 was the monitor well for Well B and Well D. 32

Figure 14. Location of the microseismic events recorded during the hydraulic fracturing process of Well A. The size of the dots is proportional to the event magnitude and the color represents the fracture stage during which they were recorded. Four fracture stages were initiated starting from toe to heel. Well V174 is the monitor well. Note the events are skewed to the west of the wellbore. 33

Figure 15. Location of the microseismic events recorded during the hydraulic fracturing process of Well B. The size of the dots is proportional to the event magnitude and the color represents the fracture stage during which they were recorded. Four fracture stages were initiated starting from toe to heel. Well V33 is the monitor well. Note the events are centered about the wellbore 34

Figure 16. Location of the microseismic events recorded during the hydraulic fracturing process of Well C. The size of the dots is proportional to the event magnitude and the color represents the fracture stage during which they were recorded. Five fracture stages were initiated starting from toe to heel. Well V174 is the monitor well. Note the events are skewed to the west of the wellbore 35

Figure 17. Location of the microseismic events recorded during the hydraulic fracturing process of Well D. The size of the dots is proportional to the event magnitude and the color represents the fracture stage during which they were recorded. Five fracture stages were initiated starting from toe to heel. Well V33 is the monitor well. Note the events are skewed to the east of the wellbore 36

Figure 18. Microseismic event distance versus magnitude crossplot for Well H3. The color bar indicates the stage during the fracturing process when the events were recorded. The size of the dots indicates the moment magnitude. 40

Figure 19. Microseismic event distance versus magnitude crossplot for Well H15. The color bar indicates the stage during the fracturing process when the events were recorded. The size of the dots indicates the moment magnitude. 40

Figure 20. Microseismic event distance versus magnitude crossplot for Well H18. The color bar indicates the stage during the fracturing process when the events were recorded. The size of the dots indicates the moment magnitude. 41

Figure 21. Microseismic event distance versus magnitude crossplot for Well A. The color bar indicates the stage during the fracturing process when the events were recorded. The size of the dots indicates the moment magnitude. 41

Figure 22. Microseismic event distance versus magnitude crossplot for Well B. The color bar indicates the stage during the fracturing process when the events were recorded. The size of the dots indicates the moment magnitude. 42

Figure 23. Microseismic event distance versus magnitude crossplot for Well C. The color bar indicates the stage during the fracturing process when the events were recorded. The size of the dots indicates the moment magnitude. 42

Figure 24. Microseismic event distance versus magnitude crossplot for Well D. The color bar indicates the stage during the fracturing process when the events were recorded. The size of the dots indicates the moment magnitude. 43

Figure 25. Microseismic event distance versus magnitude crossplot for Well V258. The color bar indicates the stage during the fracturing process when the events were recorded. The size of the dots indicates the moment magnitude. 43

Figure 26. Microseismic event distance versus magnitude crossplot for Well V259. The color bar indicates the stage during the fracturing process when the events were recorded. The size of the dots indicates the moment magnitude. 44

Figure 27. Microseismic event distance versus magnitude crossplot for Well H3 after removing the location biased points. The color bar indicates the stage during the fracturing process when the events were recorded. The size indicates the moment magnitude. The color bar indicates the fracturing stage. 44

Figure 28. Microseismic event distance versus magnitude crossplot for Well H15 after removing the location biased points. The color bar indicates the stage during the fracturing process when the events were recorded. The size indicates the moment magnitude. The color bar indicates the fracturing stage. 45

Figure 29. Microseismic event distance versus magnitude crossplot for Well H18 after removing the location biased points. The color bar indicates the stage during the fracturing process when the events were recorded. The size indicates the moment magnitude. The color bar indicates the fracturing stage. 45

Figure 30. Microseismic event distance versus magnitude crossplot for Well A after removing the location biased points. The color bar indicates the stage during the fracturing process when the events were recorded. The size indicates the moment magnitude. The color bar indicates the fracturing stage. 46

Figure 31. Microseismic event distance versus magnitude crossplot for Well B after removing the location biased points. The color bar indicates the stage during the fracturing process when the events were recorded. The size indicates the moment magnitude. The color bar indicates the fracturing stage. 46

Figure 32. Microseismic event distance versus magnitude crossplot for Well C after removing the location biased points. The color bar indicates the stage during the fracturing process when the events were recorded. The size indicates the moment magnitude. The color bar indicates the fracturing stage. 47

Figure 33. Microseismic event distance versus magnitude crossplot for Well D after removing the location biased points. The color bar indicates the stage during the fracturing process when the events were recorded. The size indicates the moment magnitude. The color bar indicates the fracturing stage. 47

Figure 34. Microseismic event distance versus magnitude crossplot for Well V258 after removing the location biased points. The color bar indicates the stage during the fracturing process when the events were recorded. The size indicates the moment magnitude. The color bar indicates the fracturing stage. 48

Figure 35. Microseismic event distance versus magnitude crossplot for Well V259 after removing the location biased points. The color bar indicates the stage during the fracturing process when the events were recorded. The size indicates the moment magnitude. The color bar indicates the fracturing stage. 48

Figure 36. Heuristic template to interpret seismic, well log, or laboratory rock properties in terms of EUR, Original Gas in place (OGIP), recovery factor (Rf), pore pressure, and fracture density. After Perez et al. (2011). 51

Figure 37. Lambda-rho/Mu-rho cross plot for the Lower Barnett Shale. Color indicates the Poisson's ratio, ν. Lines of fixed Poisson's ratio converge at the origin. 52

Figure 38. Seismic Lambda-rho/Mu-rho crossplot for the Lower Barnett Shale. Color indicates the Young's modulus, *E*, decreasing towards the origin. 52

Figure 39. Lower Barnett reservoir quality classification based on seismically inverted rock properties. Four groups are defined: Group "0" or Brittle and Rich, Group 1 or Rich and Ductile, Group 2 or Brittle and Poor, and Group 3 or Ductile and Poor. Cut offs selected to make each group as even as possible. 53

Figure 40. Seismic Lambda-rho/Mu-rho extracted along the wellbores with production logs. The color indicates the gas rate at each individual perforation. 54

Figure 41. Seismic Lambda-rho/Mu-rho extracted along the wellbores with production logs. The color indicates the well temperature at each individual perforation... 55

Figure 42. Lambda-rho/mu-rho cross plot for the Lower Barnett Shale. Color indicates the Poisson's ratio. Ovals indicate the range of values observed in the producing zones for each well. 56

Figure 43. Seismic Lambda-rho/Mu-rho extracted along the wellbores with production logs. The color indicates the gas rate at each individual perforation in WELL A. 57

Figure 44. Seismic Lambda-rho/Mu-rho extracted along the wellbores with production logs. The color indicates the gas rate at each individual stage in WELL B. 57

Figure 45. Seismic Lambda-rho/Mu-rho extracted along the wellbores with production logs. The color indicates the gas rate at each individual stage in WELL C. 58

Figure 46. Seismic Lambda-rho/Mu-rho extracted along the wellbores with production logs. The color indicates the gas rate at each individual stage in WELL D. 58

Figure 47. East-west vertical slice through the reservoir quality volume showing the location of the wells having production logs. The color in the layers is following the rock classification proposed. WELL B is entirely completed in a Brittle-Rich (red) layer, while most of WELL A, WELL C, and WELL D rest in a Ductile-Poor (blue) layer. 59

Figure 48. Stratal slice through the reservoir quality volume at the level where most of Well A, C, and D are completed (top right corner). The colors represent the rock quality distribution according to the rock classification proposed. The black square corresponds to a "no permit" zone where seismic data are missing. 60

Figure 49. Stratal slice through the reservoir quality volume at the level where most of Well B is completed (top right corner). The colors represent the rock quality distribution according to the rock classification proposed. The black square corresponds to a "no permit" zone where seismic data are missing.................. 61

Figure 50. Map view of the stratal slice through the reservoir quality volume at the level where Well A is completed. The colors represent the rock quality distribution according to the rock classification proposed. 62

Figure 51. Map view of the stratal slice through the reservoir quality volume at the level where Well B is completed. The colors represent the rock quality distribution according to the rock classification proposed. 63

Figure 52. Map view of the stratal slice through the reservoir quality volume at the level where Well C is completed. The colors represent the rock quality distribution according to the rock classification proposed. 64

Figure 53. Map view of the stratal slice through the reservoir quality volume at the level where Well D is completed. The colors represent the rock quality distribution according to the rock classification proposed. 64

Figure 54. Lambda-rho/Mu-rho cross plots showing the microseismic events recorded while hydraulically fracturing WELL A. About 73% of the microseismic events recorded while stimulating WELL A fall in portions of the rock classified as Brittle according to this reservoir quality classification. Compare to Figure 43 which shows the stages were completed in Brittle-Poor and Ductile-Poor zones. 65

Figure 55. Lambda-rho/Mu-rho cross plots showing the microseismic events recorded while hydraulically fracturing WELL B. About 70% of the MS events recorded while stimulating WELL B fall in portions of the rock classified as Brittle according to this reservoir quality classification. Compare to Figure 44 which shows the stages were completed in Brittle-Rich zones..................................... 66

Figure 56. Lambda-rho/Mu-rho cross plots showing the microseismic events recorded while hydraulically fracturing WELL C. About 64% of the MS events recorded while stimulating Well C fall in portions of the rock classified as Brittle according to this reservoir quality classification. Compare to Figure 45 which shows the stages were completed in Brittle-Poor, Ductile-Poor, and Rich-Ductile zones. 67

Figure 57. Lambda-rho/Mu-rho cross plots showing the microseismic events recorded while hydraulically fracturing WELL D. About 65% of the microseismic events recorded while stimulating Well D fall in portions of the rock classified as Brittle according to this reservoir quality classification. Compare to Figure 46 which shows the stages were completed in Brittle-Poor, Ductile-Poor, and Rich-Ductile zones. 68

Figure 58. Lambda-rho/Mu-rho cross plots showing the microseismic events recorded while hydraulically fracturing WELL H18. About 57% of the microseismic events recorded while stimulating the well fall in portions of the rock classified as Brittle according to this reservoir quality classification. 71

Figure 59. Lambda-rho/Mu-rho cross plots showing the microseismic events recorded while hydraulically fracturing WELL H3. About 62% of the microseismic events recorded while stimulating the well fall in portions of the rock classified as Brittle according to this reservoir quality classification. 72

Figure 60. Geologic Time Scale: The Geological Society of America. Walkerand Geissman (2009)... 101

Abstract

Horizontal drilling and hydraulic fracturing are two key technologies key to unlocking the enormous amount of hydrocarbons retained in the source rock. Efficient drilling and completion programs require quantitative estimates of the vertical and lateral variation of the drillability and fracability of the rock.

Previous studies have shown that Lambda-rho/Mu-rho cross plots from surface seismic data can be used to quantitatively grade reservoir rocks in unconventional plays. In this thesis, I examine the utility of these cross plots with actual field data acquired from the Lower Barnett Shale play. I use seismically inverted Poisson's ratio as a fracability discriminator and Young's modulus as an indicator of Total Organic Carbon (TOC) richness and porosity. I classify the Lower Barnett Shale in the study area into four rock groups: Brittle-Rich, Rich-Ductile, Brittle-Poor, and Ductile-Poor. I validate these results using production logs recorded in four horizontal wells and microseismic data acquired while fracturing six horizontal wells. Production logs directly measure the rates coming from each perforation cluster while microseismic events directly measure locations where the rock breaks.

Integration of seismic data, production logs and microseismic data indicates that Brittle-Rich zones are the most suitable locations to drill wells in this particular shale play because they exhibit two components: significant hydrocarbon in place and sufficient strength to sustain effective fractures. On the other hand, rock zones characterized as Ductile-Poor should be avoided during drilling and fracturing since once the fracturing pressure is released, the rock will close back against the proppant resulting in ineffective completions.

Chapter 1

Introduction

In an attempt to reduce the United States' dependence on energy imports and to satisfy the ever growing demand for energy, there has been an increasing emphasis on developing the vast hydrocarbon resources in unconventional accumulations of oil and gas, primarily in shale oil and shale gas plays. (Bruner and Smosna, 2011; Schenk and Pollastro, 2002). Traditionally, gas production from shale was virtually non-existent because gas shales are characterized by extremely low permeabilities on the order of a few nano-Darcies. However with the rapid evolution of drilling and completion technology over the past two decades, shale gas plays now constitute a significant percentage of overall US gas production (EIA, 2011).

A key development critical to making shale wells economically productive over extended periods of time is hydraulic fracture treatment. In combination with horizontal well technology, shale gas wells are now orders of magnitude more productive than wells completed in similar settings in the 1990s to the early 2000s. Shale wells are now routinely completed with a suite of hydraulic fracture treatments in several stages (Bennett et al., 2006; Bruner and Smosna, 2011; EIA, 2011). The stages are designed to contact as much of the reservoir rock as possible thereby creating effective gas migration pathways between the reservoir rock and the wellbore (Daniels et al., 2007; Cipolla et al., 2008; Mayerhofer et al., 2010; Zimmer, 2011; Cipolla et al., 2012; Yu and Aguilera, 2012).

Traditionally shales were considered to be homogenous in nature and consequently efforts to characterize gas shales were fairly limited. In the recent past, laboratory experiments on cores (Kale, 2009), the drilling process and seismic-derived images (Sullivan et al., 2006; Elebiju et al., 2010) have clearly demonstrated the need for improved characterization of gas shales because of the short-range and long-range heterogeneities that impact gas storage, transport and completion effectiveness (Cipolla et al., 2008; Cipolla et al., 2012). By mapping these heterogeneities and identifying the location and distribution of significant gas accumulations within these shales, engineers and geoscientists are attempting to extract these resources more efficiently and economically. This thesis is also organized around this main theme - to identify optimal locations for infill drilling and for hydraulic fracture treatments.

Although the Barnett Shale is the most studied and well known shale play in the US (Boyer et al., 2006), several knowledge gaps related to integrating geologic, geophysical, petrophysical and engineering data still exist (Gupta et al., 2012). Perez et al. (2011) generated templates for shales of varying compositions and porosities based on seismic-derived rock properties to enable targeting the most productive volumes of the reservoir which are also most conducive to hydraulic fracture stimulation. Other studies (Kale, 2009 and Gao, 2011) are centered on petrophysical characterization and rock-typing based on cores and well log information. Singh (2008) instead relied on well logs to generate stratigraphic cross-sections of the Barnett shale along with classification of the shale into 10 lithofacies.

To identify sweet spots in unconventional gas shale reservoirs it is of utmost importance to have both; high reservoir quality defined by high porosity and high Total Organic Carbon (TOC) rock, as well as good completion effectiveness defined by the potential for fracture initiation and the ability for the fractures to remain open with time

(Cipolla et al. 2011a). In the 2011a paper, Cipolla et al. did a comprehensive analysis of the factors affecting the reservoir quality and the completion effectiveness. They used a wide variety of field information from sonic well logs to microseismic and seismic data, but they did not validate their model with production data in a perforation cluster by perforation cluster basis as I did in this thesis.

In 2012, Maity and Amizadeh presented a similar approach of data integration for reservoir characterization. They also used seismically inverted rock properties to extend the well log data to the inter-well volumes, but they failed to validate their workflow with microseismic or production data.

Refunjol et al. (2012) using a Barnett Shale case study, present a methodology to correlate the hydraulically induced microseismic events with some seismic attributes such as curvature. They also explored the Lambda-rho/Mu-rho cross plots but they did not link the microseismic event distribution to rock brittleness. For their case study they did not have production logs available.

The work presented in this thesis is unique in the sense that nobody has merged production logs, which enable us to analyze the completion effectiveness variation along the horizontal section of the wellbores, with microseismic and seismic data. Also unique is the way in which I used the microseismic data recorded while fracturing the wells. I used them to map the stimulated volume of rock as most studies have done before, but I also came up with a very ingenious way to validate the claim that shale rocks exhibiting low values of Poisson's ratio are more brittle and fracture prone than shale rocks having high values of Poisson's ratio without needing to break an inch of rock.

Barnett Shale Petrophysics

Petrophysical characterization of a reservoir involves identifying rock types with similar flow and storage capacities (Kale et al., 2010a; Kale et al., 2010b). According to Gunter et al. (1997) a rock type is a unit of rock deposited under similar geological conditions that underwent similar diagenetic processes resulting in unique porosity-permeability relationships, capillary pressure profile and water saturations above free water.

A comprehensive summary of the Barnett Shale properties compared to the Marcellus Shale properties can be found in Table 9 of Bruner and Smosna (2011).

Conventional methods of rock typing based on porosity-permeability cross plots do not work in shales due to the lack of dynamic range and the difficulties involved in the direct measurements of most of the petrophysical properties (Kale et al., 2010a; Kale et al., 2010b). Aware of this limitation, different attempts have been done to appropriately do the petrophysical classification in shales.

For example, Kale (2009) and Gao (2011) performed petro-typing based on core measurements acquired from 3 vertical wells located in the Newark East field. Kale (2009) did measurements on 800 feet of core and identified 3 key measurements such as: porosity (φ), total organic carbon (TOC), and total carbonate (TC). Clustering analyses indicated 3 petro-types which were ranked as (1) good, (2) intermediate, (3) poor based on petrophysical properties and through correlation with cumulated production data in the cored wells. General characteristic of petrotype 1 through 3 are provided in Table 1 and Figure 1. Hoeve et al. (2011) attempted to identify "sweet-spots" through the use of well-logs. Their basic premise was that the porosity–thickness obtained from wireline logs are a fairly good indicator of reservoir quality.

Table 1. General petrophysical characteristics of petro-types identified on the basis of core measurements (Kale, 2009).

	TOC (wt%)	φ (%)	TC (wt%)
Petrofacies 1	Average 4.5 Range:1.5 - 7.5	Average 6.5 Range:1.0 – 13.0	Average 12 Range:0 – 83
Petrofacies 2	Average 4.7 Range:1.3 - 67	Average 6.0 Range:0.6 – 9.0	Average 20 Range:0.7 – 64
Petrofacies 3	Average 2.5 Range:1.6 – 4.0	Average 4.3 Range:1.0 – 8.0	Average 50 Range:5 – 86

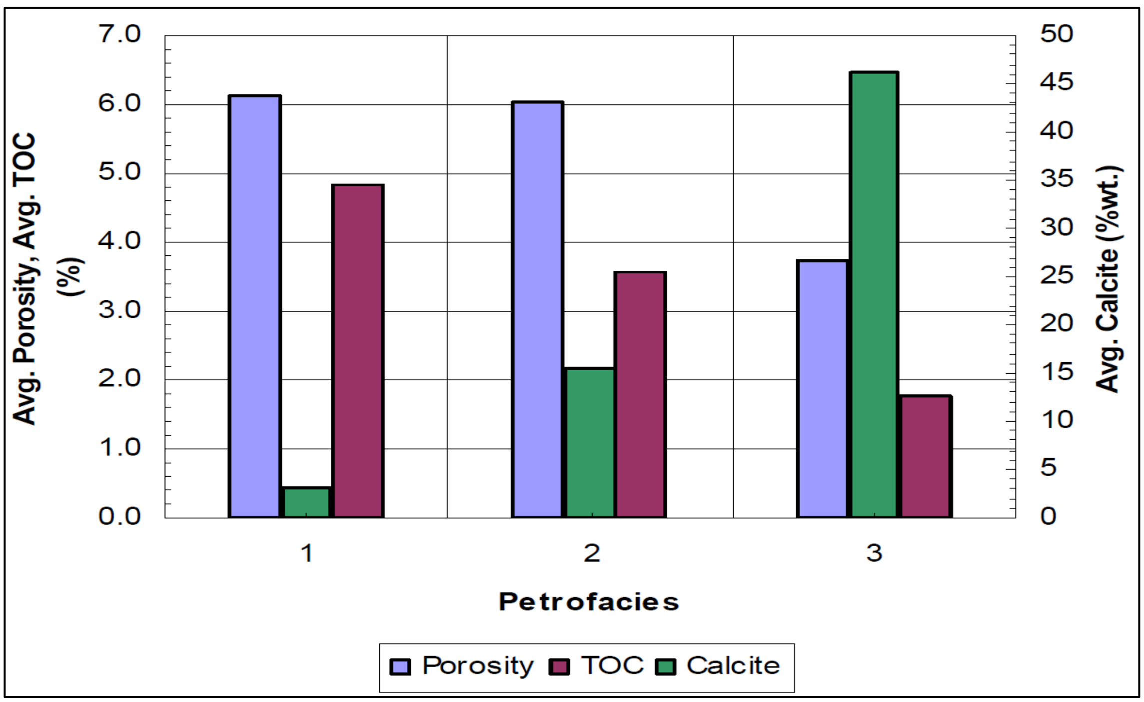

Figure 1. Average porosity, average total organic carbon (TOC), and average calcite content of the three petrotypes defined by Kale et al., 2010a, 2010b.

The work presented in this thesis documents my approach to develop a reservoir rock quality classification template for locating infill wells and hydraulic fracture treatments successfully by integrating seismically inverted rock properties such as Lambda-rho, Mu-rho, Young's modulus and Poisson's ratio with microseismic and production log data. Following an analogous approach to the one presented in the rock physics templates developed by Perez et al. (2011), I propose the use of Young's modulus and Poisson's ratio in the Lambda-rho/Mu-rho cross plots to identify the most suitable places to drill and fracture across all the seismic volume.

Not surprisingly, the vertical distribution of my best and worst rock class groups which I defined as Brittle and Rich (best), and Ductile and Poor (worst); correspond in general terms to petrotype 1 and petrotype 3 defined by Kale et al. (2010a, 2010b). This reflects the direct relationship between mineralogy and rock properties. Particularly in the Barnett Shale, high porosity and high TOC zones are associated to low total carbonate content (petrotype 1) while low porosity and low TOC zones are associated to high total carbonate content (petrotype 3).

In Chapter 3 I describe the data available for this study. I also present a brief overview of how the data are typically acquired and processed for analysis. Because microseismic data is critical to the validation of the template that I propose, Chapter 4 is entirely devoted to post-processing and data quality control of the microseismic data. Chapter 5 focuses on development of the rock quality template and is followed by validation of the template using production logs and microseismic data in a field application in the Lower Barnett Shale.

In summary, this thesis describes a workflow to integrate multidisciplinary and multiscale subsurface data (3D seismic, production logs, and microseismic) to characterize twenty (20) square miles in the Lower Barnett Shale play resulting in a rock classification model that was properly validated.

Chapter 2

Geology of the Barnett Shale

The Barnett Shale is present across most of the Fort Worth Basin and extends over a total area of 28,000 square miles (Bruner and Smosna, 2011). Figure 2 shows the major geological features that influence the Barnett Shale and the structural contours. The gray zone represents the main producing area of the Newark East field and the yellow shaded area is the potential Barnett Shale play which roughly represents one third of the entire Barnett. The potential shale play is located toward the northeast, where the Barnett becomes thicker. According to Durham (2005), The Newark East field, the sweet spot of shale-gas production, covers 500 sq. miles on parts of Denton, Wise, and Tarrant Counties. The Newark East field is currently the largest gas field in Texas covering 500 sq. miles, with over 2,400 producing wells and 2.7 tcfg of proven reserves. Contour lines in Figure 2 are drawn on top of the Ellenburger Group, the base of the Barnett Shale.

The Barnett outcrops on the Llano Uplift at the southern limit of the basin and dips northward until the Muenster Arch and Red River Arch. These last two represent the northern limit of the basin. The other two geographic limits of the Barnett are the Ouachita Thrust front to the east, and the Eastern shelf and Concho Arch to the west (Pollastro, 2007). Figure 3 shows north-south and west-east cross sections through the Fort Worth Basin, illustrating the structural position of the Barnett Shale between the Muenster Arch, Bend Arch, and the Llano Uplift.

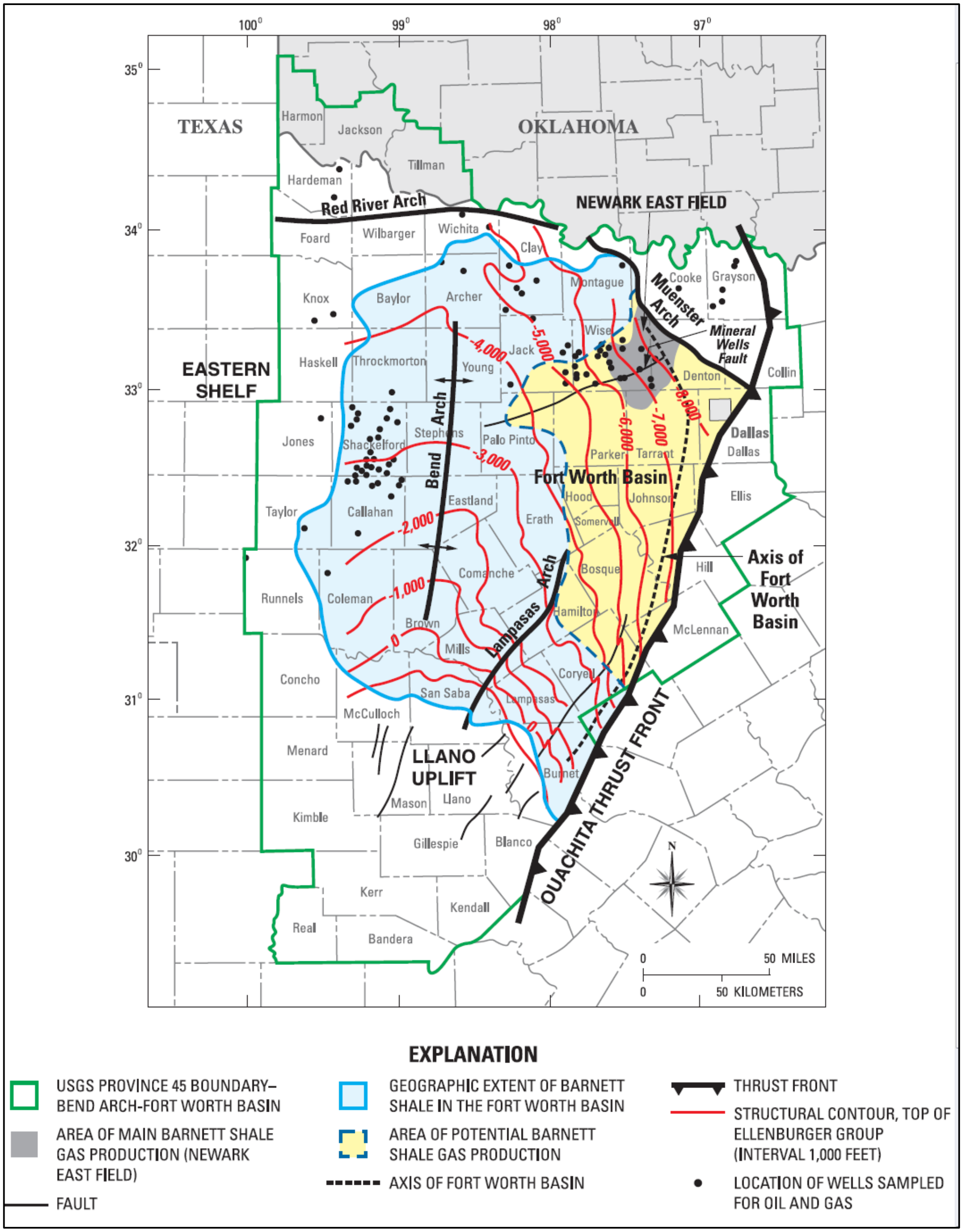

Figure 2. Location of the Mississippian Barnett Shale, Fort Worth Basin, showing the major geological features that influence the Barnett Shale and structural contours. The main producing area of the Newark East field is indicated by darker shading. Contours are drawn on top of the Ordovician Ellenburger Group; contour intervals equal 1,000 feet. Bruner and Smosna (2011).

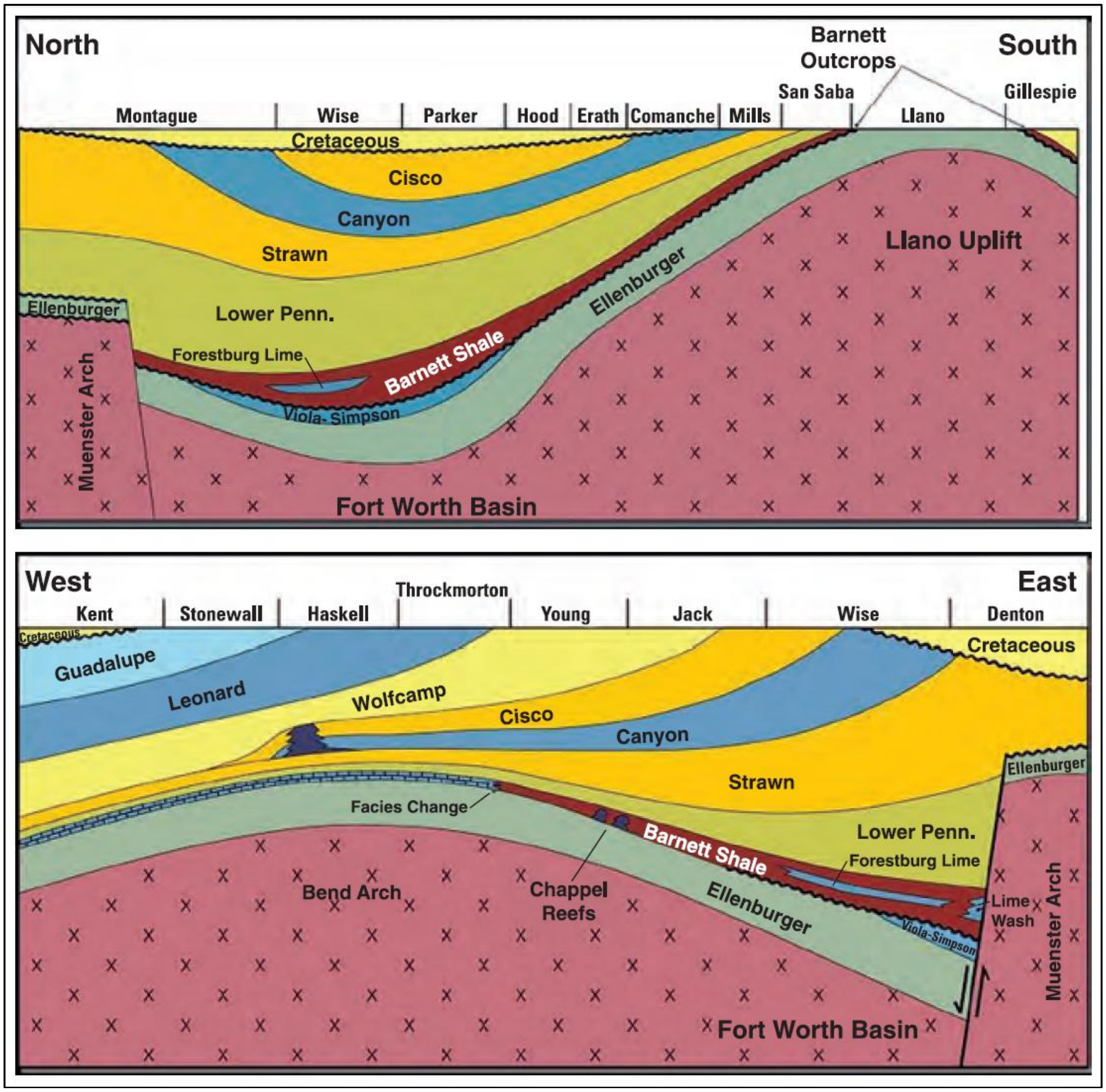

Figure 3. North-south and west-east cross sections through the Fort Worth Basin illustrating the structural position of the Barnett Shale between the Muenster Arch, Bend Arch, and Llano Uplift. Bruner and Smosna (2011).

The study area, part of The Newark East field, is located north of The Mineral Wells Fault, and covers around 20 square miles in Wise and Denton counties. The quality of the 3D seismic data is good enough to identify the main stratigraphic units, but this thesis will focus exclusively on the lower member of the Barnett Shale play. Figure 4 shows the detailed location of the area of study (green shaded region on top right square).

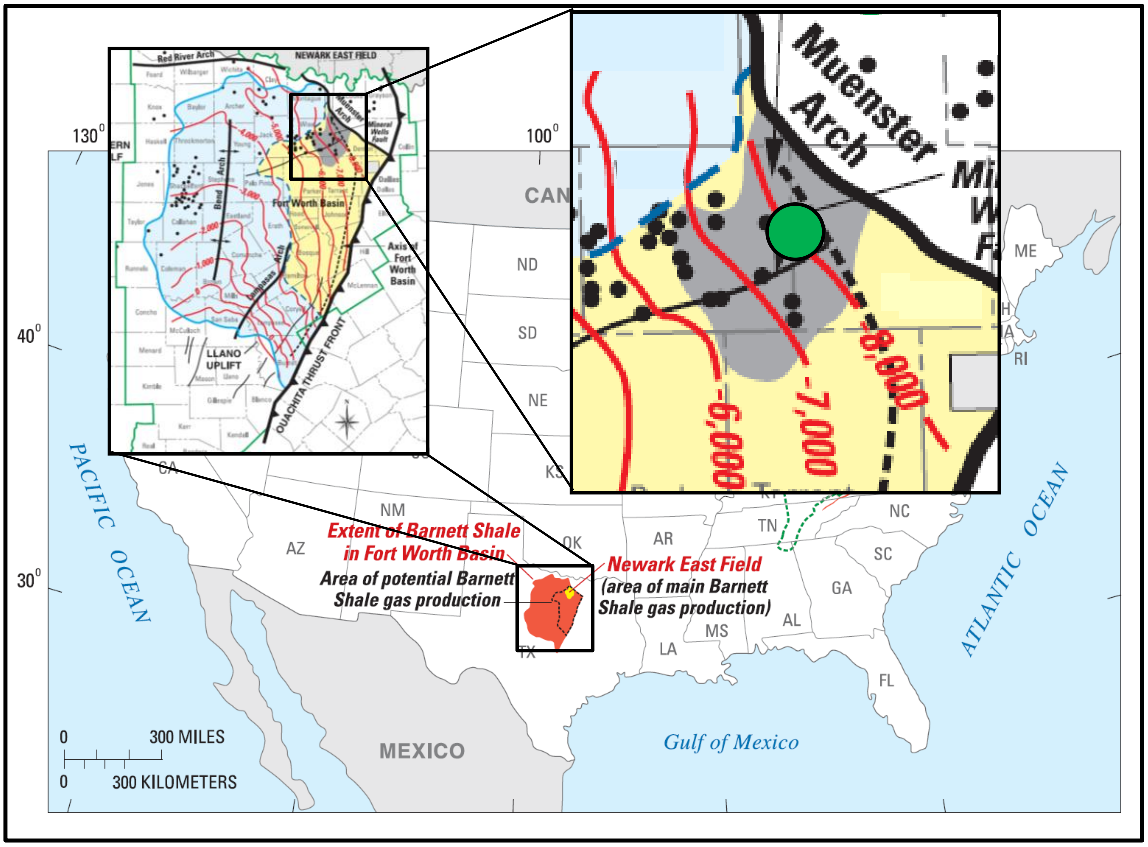

Figure 4. Location of Mississippian Barnett Shale, Fort Worth Basin. The top right square details a zoom in to the area of study, green circle. Modified from Bruner and Smosna (2011).

Geological Setting

The Fort Worth Basin formed during the late Paleozoic Ouachita Orogeny (See Appendix B for the geologic time scale); as a result of the Laurassia and Gondwana plate convergence. According to paleogeographic reconstruction by Gutschick and Sandberg (1983), Arbenz (1989), and Blakely (2005), it used to be a narrow, restricted, inland seaway that underwent the main deposition during the middle to late Mississippian (around 340 to 325 Ma) in relatively deep waters (600 to 1000 ft.) (Figures 5 and 6).

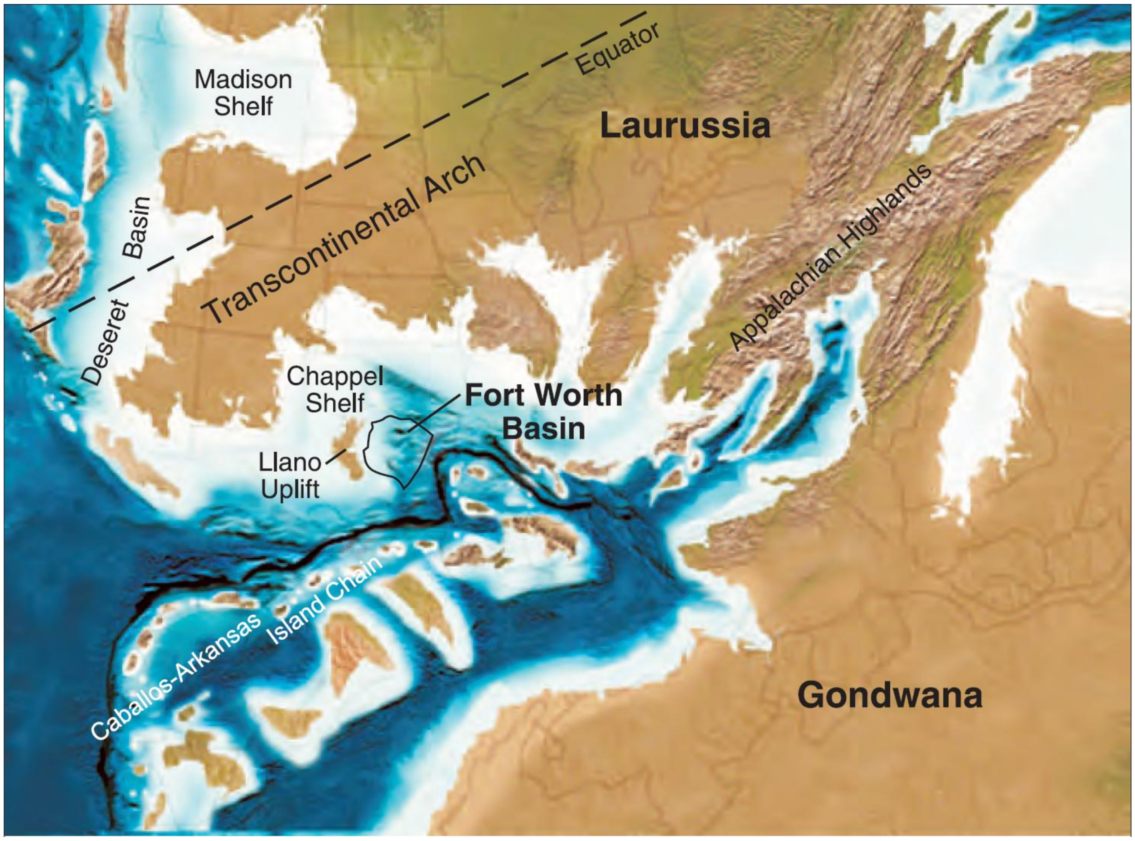

Figure 5. Regional paleogeography of the southern mid-continent region during the Late Mississippian (325 Ma), showing the approximate position of the Fort Worth Basin. Modified from Blakey (2005) Loucks and Ruppel (2007).

Nowadays, the basin is elongated northeast-southwest, dipping towards the northeast (Lancaster et al., 1993). The Ouachita Trust Front represents the east limit. Parallel to the Ouachita Trust Front lays the original axis of deposition (Figure 6) (Montgomery et al., 2005). The Red River and Muenster arches enclose the basin in the north. The shallow Bend Arch represents the western basin limit. The Barnett Shale also thins and vanishes towards the top of the Bend Arch as can be observed in Figure 3. The Llano uplift is a dome that exposes The Barnett Shale and The Ellemburger group (Figure 3) (Loucks and Ruppel, 2007) and forms the natural limit of the basin in the south.

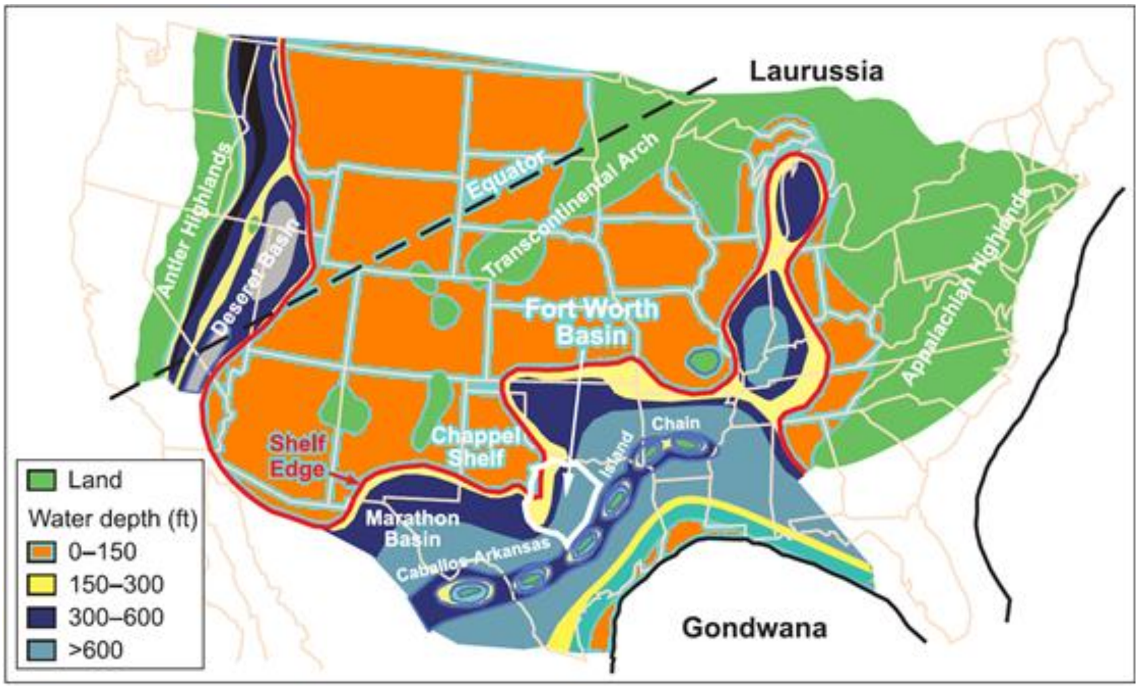

Figure6. Middle Mississippian paleogeographic map of the United States indicating that the Fort Worth Basin was relatively deep. Modified from Gutschick and Sandberg (1983), Loucks and Ruppel (2007).

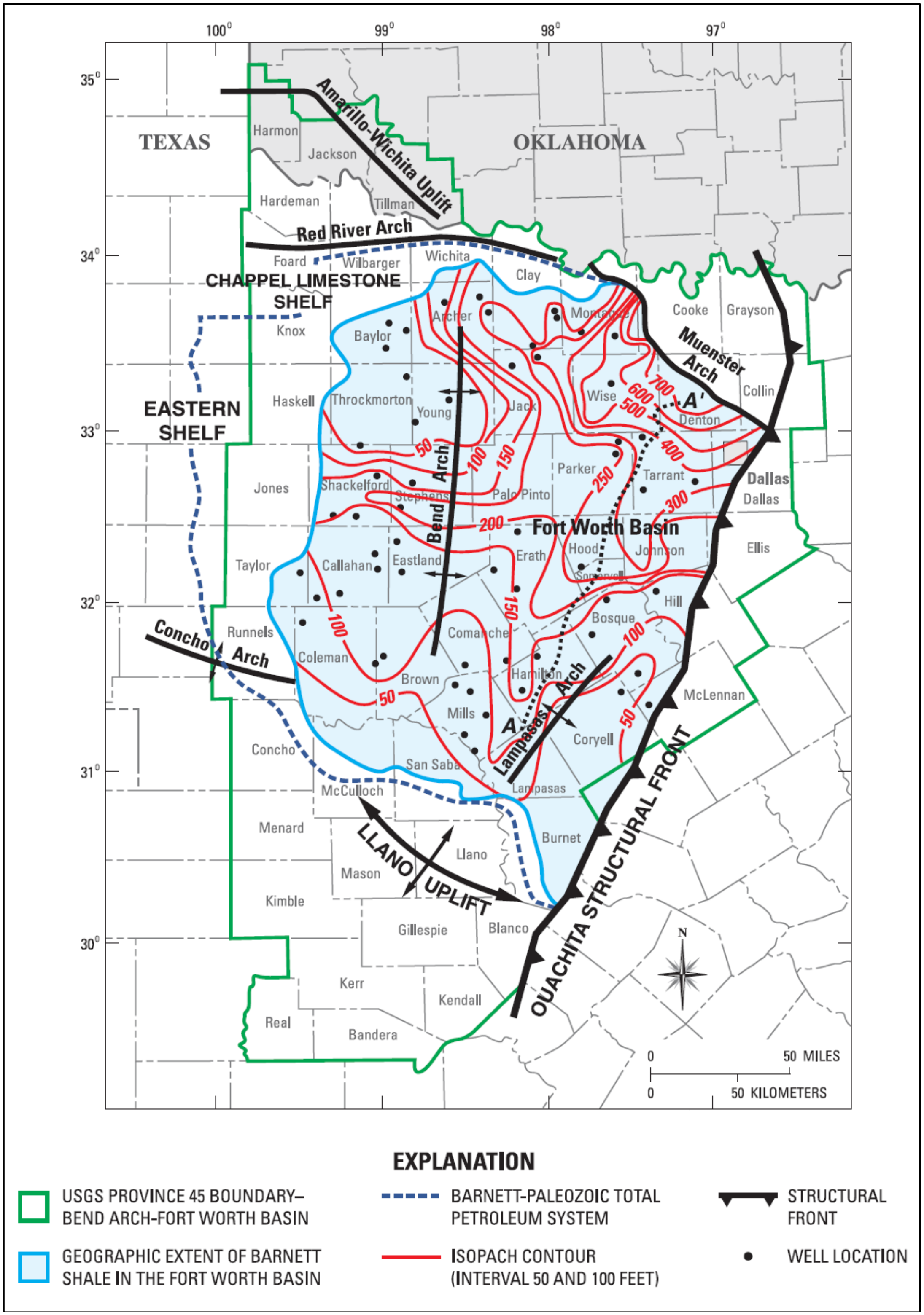

Figure 7. Thickness of Barnett Shale, isopach lines in red, contour interval equals 50 and 100 ft. Line A-A' marks the approximate axis of deposition. Modified from Barnett Shale Maps, 2007; Bruner and Smosna (2011).

Stratigraphy

In the northeast portion of the Fort Worth Basin where my area of study is, the Pennsylvanian Barnett Shale play is considered to be divided into Upper and Lower members by the intervening Forestburg Limestone (Hayden and Pursell, 2005; Loucks and Ruppel, 2007). The upper member is thinner and dolomite rich compared to the Lower member. Some authors (Loucks and Ruppel, 2007); consider that the Lower member is subdivided into five different shale packs interlayered with limestone. The results from this research are in agreement with Loucks and Ruppel (2007) observation as I will show in the Results and Analysis chapter.

The Lower Barnett shale, in the area of study is unconformably underlain by the Ordovician Viola-Simpson Limestones. Devonian and Silurian aged rocks are absent in this zone (Loucks and Ruppel, 2007). The Viola-Simpson Limestone and the Forestburg Limestone are considered to be fracture barriers but the microseismic data recorded during the stimulation of some of the wells show that the fractures are migrating towards the underlying and overlaying limestones.

The Lower Ordovician Ellenburger group which is a porous, water-bound dolomite and chert-rich limestone occurs below the Viola-Simpson Limestones in the area of interest, or directly in contact with the Barnett Shale towards the southwest after the Viola-Simpson pinches out (Pollastro et al., 2003; Bruner and Smosna, 2011).

The Barnett is conformably overlaid by the Marble Falls Formation, mostly Pennsylvanian in age although the lowest strata may be Late Mississippian. The Marble Falls is limestone comprising an upper and a lower member differentiated by the mineralogical composition (Montgomery et al., 2005).

Figure 8(A) shows a diagrammatic cross section of the stratigraphy of the Fort Basin according to Montgomery et al. (2005).Figure 8(B) shows a wire-line log from a well in the Newark East field with the major stratigraphic units (Loucks and Ruppel, 2007)

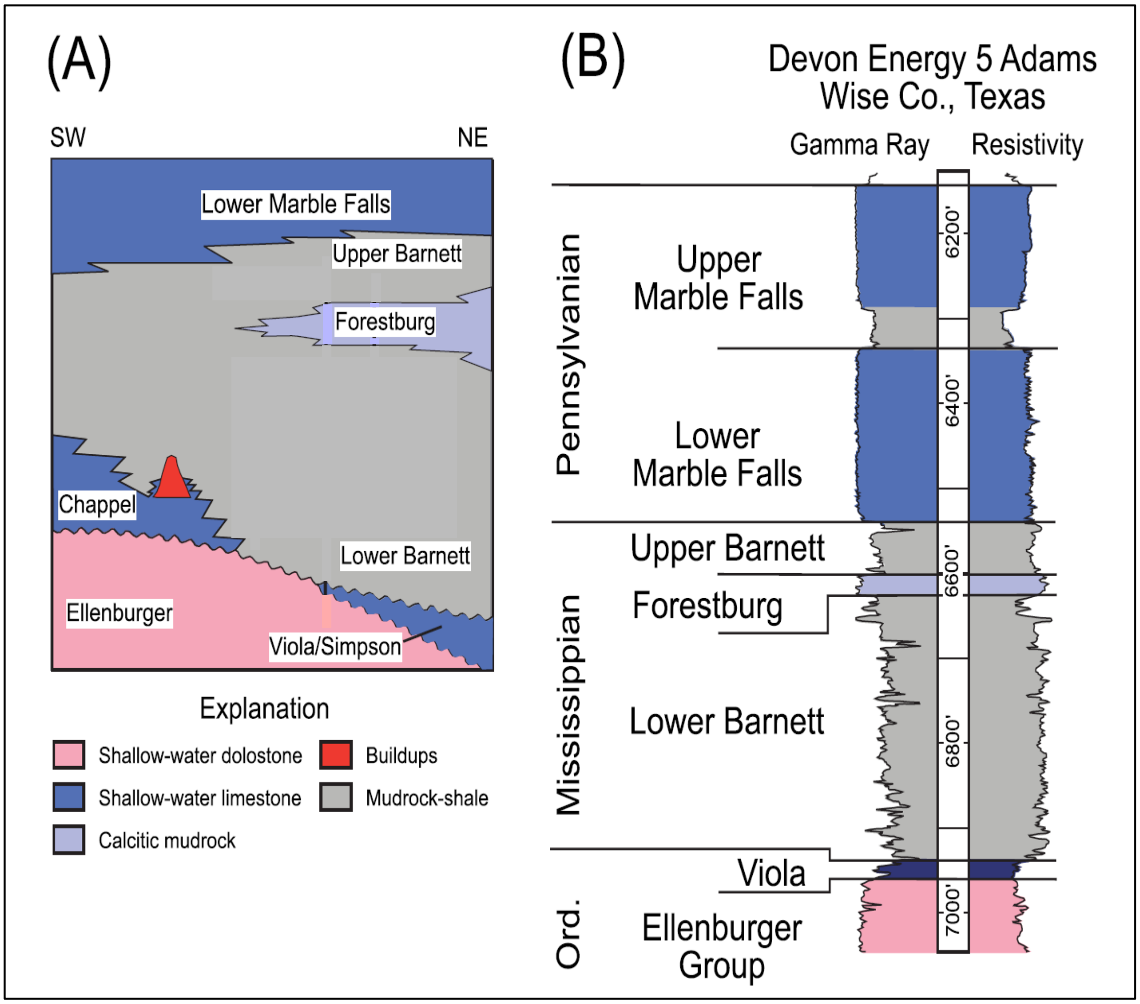

Figure 8. General stratigraphy of the Ordovician to Pennsylvanian section in the Fort Worth Basin. (A) Diagrammatic cross section of the stratigraphy of the Fort Basin after Montgomery et al. (2005). (B)Wire-line log with major stratigraphic units. (Modified from Loucks and Ruppel, 2007)

Chapter 3

Overview of Available Field Data

In this chapter, I present an overview of the data available for the study area located in the Newark East Field. The thesis is centered around the development of a predictive tool based on surface seismic data analysis to rapidly demarcate the most prolific reservoir volumes, to identify zones more amenable to hydraulic fracturing and to provide a methodology to locate productive infill wells for further development. Prior work related to large-scale reservoir characterization has typically centered on the use of well logs and cores and may be of limited value in inter-well volumes. By integrating information derived from seismic data, microseismic data and production logs, larger reservoir volumes may be probed to locate infill wells and hydraulic fractures more effectively.

This project integrates engineering tools like production logs from four horizontal wells completed in the Lower Barnett Shale and microseismic data recorded to monitor the hydraulic fracturing process with geophysical data such as time-migrated 3D seismic volumes. Seismic-derived rock properties such as Lambda-rho, Mu-rho, Young's modulus, and Poisson's ratio are key parameters that extend rock classification beyond the near wellbore region. The methodology is validated with microseismic data and production log analysis and in general, the workflow outlined in this thesis may be applicable to other shale plays. Although microseismic data are now routinely recorded during hydraulic fracture stimulation, my work also underscores the relevance of recording production logs in a few select wells in order to directly link seismic-derived properties to fracture effectiveness and productivity along the length of the lateral, which may be several thousand feet in length and completed with multiple hydraulic fracture stages.

The study area included four production wells where production logs were recorded about five months after a multi-stage hydraulic fracture treatment was carried out. The suite of production logs for the four horizontal wells comprises of the directional survey, temperature log, and the spinner flowmeter log. This work did not have access to the raw production logs; instead, previously interpreted production logs such as differential gas production and gas and water hold up were used. These logs were recorded along the horizontal section where the wells were completed

In the study area, microseismic data are available for nine horizontal wells, including the four wells with production logs and also includes two other vertical wells. The main information provided within the microseismic dataset includes the estimated XYZ-t coordinates and magnitude of the microseismic events. A weighting factor indicating the reliability of the microseismic moment magnitudes is also included. It is not said but my interpretation is that this reliability factor is calculated from the signal to noise ratio of the traces.

The seismic volume consists of 365 in-lines, 269 cross-lines with a bin size of 110 x 110 feet, covering around 20 square miles in the northeast part of the Fort Worth Basin (FWB). Within this volume 308 vertical and 127 horizontal wells were drilled before the seismic data were acquired. The list of wells with data recorded in each of them is provided in Table 2. Horizontal wells, A, B, C and D were the only wells where production logs were recorded.

Table 2. Inventory of data used in this thesis.

WELL	SEISMIC	MICROSEISMIC	PRODUCTION LOGS	OBSERVATION
A	↙	↙	↙	
B	↙	↙	↙	
C	↙	↙	↙	
D	↙	↙	↙	
H10	↙	↙		The microseismic Magnitudes corresponding to Well H10 were not recorded
H15	↙	↙		This well is completed in the Upper Barnett
H18	↙	↙		
H3	↙	↙		
H30	↙	↙		The microseismic Magnitudes corresponding to Well H30 were not recorded
V258	↙	↙		Vertical well located in the south-east limit of the seismic survey
V259	↙	↙		Vertical well located in the south-east limit of the seismic survey
V82	↙			Monitor well for microseismic data in well H3
V234	↙			Monitor well for microseismic data in well H10
V16	↙			Monitor well for microseismic data in well H15
V290	↙			Monitor well for microseismic data in well H18
V120	↙			Monitor well for microseismic data in well H30
V174	↙			Monitor well for microseismic data in Well A and Well C
V33	↙			Monitor well for microseismic data in Well B and Well D
JV41				Monitor well for microseismic data in well V258. This well is outside the limits of the seismic survey
JV40				Monitor well for microseismic data in well V259. This well is outside the limits of the seismic survey

Production Logs

Reservoir performance monitoring, well completion evaluation, and planning and evaluation of well workovers are the most common applications of production logs. The purpose of production logs is to evaluate the fluid flow inside and outside the pipe (Hill 1990). In this case study, the production logs were recorded in four neighboring horizontal wells completed in the Lower Barnett Shale with the main purpose of evaluating the effectiveness of the hydraulic fracturing process.

Even though the stimulation process was very similar across all four horizontal wells with similar number of fracturing stages, similar volumes of fluid and proppant pumped, similar treatment times and pressures with the assumption that the formation was relatively homogeneous in the zone, the disparity in the production rates between the wells motivated the operator to acquire production logs to assess fracture effectiveness.

The production logging suite for the four wells comprised the temperature log, pressure log, deviation survey and spinner flow meter log. These were then analyzed for gas flow rates along the lateral, incremental gas production along the lateral and gas and water hold up. These logs were recorded along the horizontal section where the wells were hydraulically fractured. Figures 9 and 10 show the incremental gas production log and the temperature log respectively for the four horizontal wells.

In Figure 9, the differential gas production, or gas production rate at each perforated interval, is indicated by the color and diameter of the discs along the wellbores. The differential gas rate varies from a minimum of 80 MSCF/d to a maximum of 1250 MSCF/d. The background is a seismic attribute called ant-tracked coherence which is particularly well suited to demarcate faults and existing fractures at the time the seismic survey is recorded. Further details are provided in Chopra and Marfurt (2008). These logs were recorded with the FloScan Imager (FSI) ™ (Schlumberger, 2012) which is capable of determining multiphase flow rates in horizontal and deviated wells. The liquid and gas holdup logs are also determined with this tool.

Figure 10 is showing the temperature along the horizontal section for the four horizontal wells. Temperature logs are very useful to identify injection or production zones and are very sensitive to gas entry along the wellbore. When comparing Figures 9 and 10, every point of gas production in Figure 9 corresponds to a sharp temperature decrease in Figure 10. This is a common observation in gas wells and makes temperature logs of considerable significance to identify gas entry. The cooling effect is due to the Joule-Thomson effect which describes the increase or decrease in the temperature of a real gas (as differentiated from an ideal gas) or a liquid when allowed to expand freely through a valve or other throttling device while kept insulated so that no heat is transferred to or from the fluid, and no external mechanical work is extracted from the fluid (Hill 1990). As gas enters the wellbore from the formation through the casing perforations, Joule-Thomson cooling is often observed due to the throttling effect of the perforations.

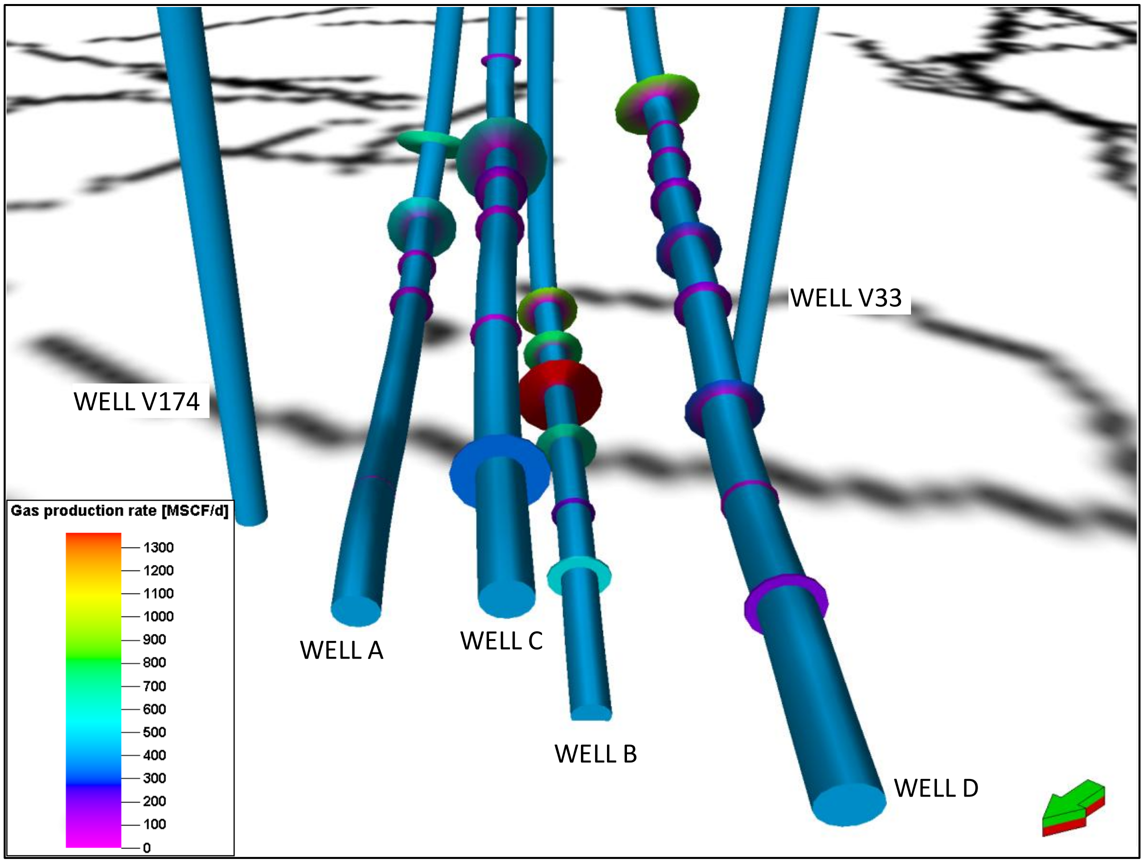

Figure 9. Differential gas production (MSCF/d) indicated by the color and diameter of the discs along the wellbores. The background is a depth slice matching the depth at which Well B is completed of a seismic attribute called ant-tracked coherence. Ant track is particularly well suited to detect discontinuities in the subsurface.

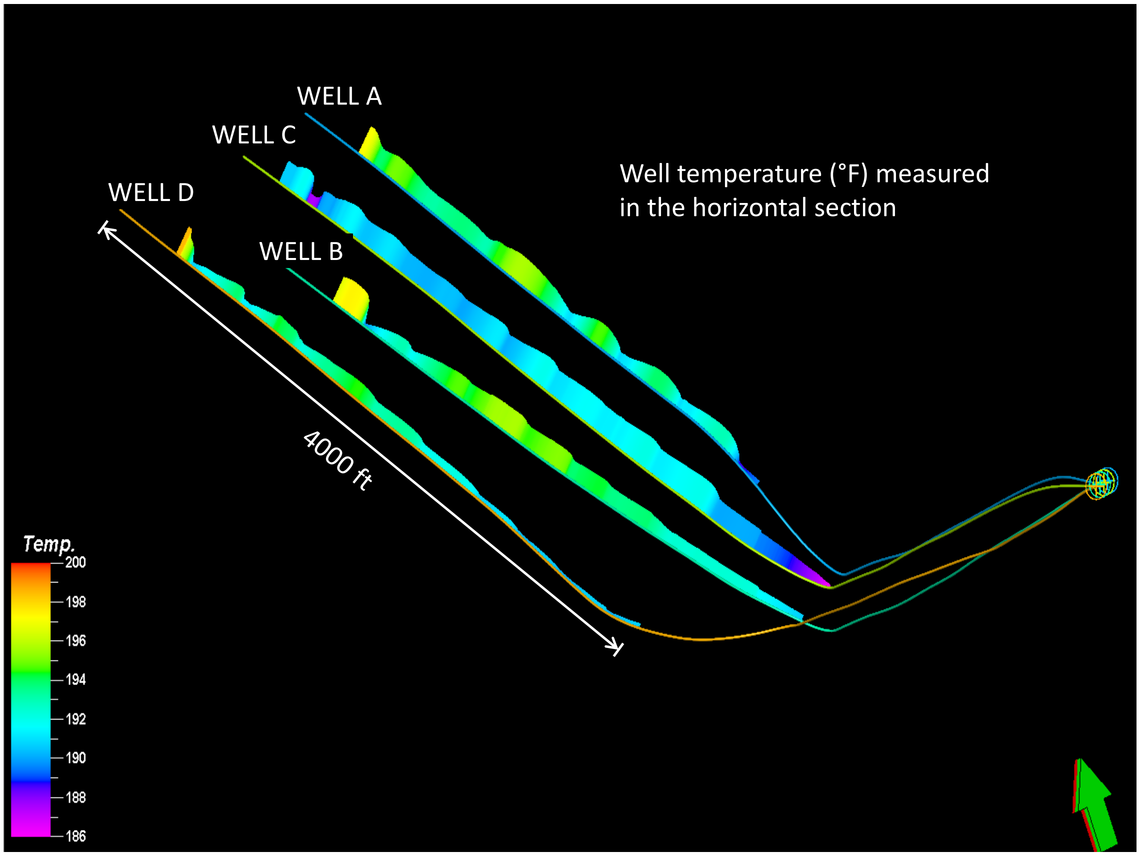

Figure 10. Top view of wells showing the temperature along the horizontal section of the four parallel horizontal wells drilled in the Lower Barnett Shale.

Seismic Data

The original seismic data were acquired by Devon in April 2009, about three months after the wells A, B, C, and D were hydraulically fractured. Overall, the seismic data are high quality, with frequencies approaching 100 Hz (Thompson 2010). Table 2 summarizes the acquisition parameters.

Automatic Gain Control (AGC) was applied using a one second window, followed by a time variant filter interpolated between the following control points (Thompson, 2010): 0.0-1000 ms: 10/15-90/110 Hz; 1000-1400 ms: 10/15-80/100 Hz; 1400-1800 ms: 10/15-75/95 Hz, 1800-3000 ms: 10/15-45/58 Hz. Since the Barnett

Shale, which is the focus of this thesis, shows up in the 1100 to 1400 ms time window, the frequency content is restricted to the 10-100 Hz band due to the filters applied.

Table 3. Acquisition parameters used to allow subsequent azimuthal processing. From Thompson (2010).

Number of live lines	30
Number of stations per line	120
Receiver line interval	660 ft.
Receiver group spacing	220 ft.
Shot line interval	880 ft.
Vibrator array interval	220 ft.
Patch size	26,180 ft. by 25,520 ft.
Nominal bin size	110 ft. by 110 ft.
Number of vibrator sweeps	8
Number of vibrators per array	3
Sweep range	10-110 Hz, 10 s duration, 3 dB/octave
Number of geophones per group	6 in a 6 ft. circle around station.

Using near offset (0°-15°) and mid-offset (15°-30°) components independently, Refunjol (2010) extracted the zero phase wavelets across an older Barnett Shale survey to the south finding the peak amplitudes between 38 Hz and 50 Hz. Through seismic inversion he also found average density of 2.52 g/cm^3 and average P-wave velocity of 13095 ft/s for the lower Barnett Shale. The same analysis carried out on my survey resulted in a peak seismic amplitude of 40 Hz, an average density of 2.5 g/cm^3 and an average P-wave velocity of 12651 ft/s. This implies that the average or most likely vertical resolution that should be expected within this zone is,

$$\frac{wave\ legth}{4} = \frac{V_P}{4f} = \frac{12651\ ft/s}{4 * 40\ s^{-1}} = 79ft. \qquad (1)$$

Therefore, I can expect to resolve intervals of 79 ft. and thicker.

The seismic survey consists of 365 in-lines, 269 cross-lines with a bin size of 110 x 110 feet, covering around 20 square miles in a region where 308 vertical and 127 horizontal wells were drilled before the seismic data were acquired

For this thesis I was provided (Perez, 2010) with pre-stack time migrated volumes of P- and S-impedance, Lambda-rho, Mu-rho, Young's modulus, and Poisson's ratio. These products resulted from seismic inversion processes applied on offset components ranging between 3°-43° pre-stack migrated survey.

Properly tied or calibrated to well measurents, seismic inversion is a powerful tool that allow us to characterize the interwell regions. Seismic inversion using a "global" optimization algorithm is based on convolving the seismic wavelet and the Earth's reflectivity through a forward model until a match to the measured data is found.

The seismic data were inverted using a commercial inversion algorithm that requires angle-dependent wavelets and angle stacks and results in estimates of P-impedance, S-impedance and density. This algorithm starts with an initial low frequency background impedance model of the Earth that is updated using a simulated annealing method until the derived synthetic seismic section best fits the observed seismic data (Hampson and Rusell, 2005).

The three assumptions implicit in the algorithm used in the commercial software are: (i) the linearized approximation for reflectivity holds, (ii) reflectivity as a function of angle can be approximated by the Aki-Richards equations, and (iii) there is a linear relationship between P-impedance and S-impedance with density.

Once the P and S impedance volumes have been generated they can be used to calculate the Lamé parameters of imcompressibility, λ, and rigidity, μ. Incompressibility is more sensitive to the pore fluids than to the matrix, and for elastic materials rigidity is only influenced by the matrix connectivity (Dufor et al., 2002; Goodway et al., 1997).

For homogeneous isotropic linear elastic materials,

$V_P^2 = \frac{(\lambda + 2\mu)}{\rho}$ is the compressional wave velocity, (2)

ρ is the density,

$V_S^2 = \frac{\mu}{\rho}$ is the shear wave velocity, (3)

$Z_P = \rho V_P$ is the P-wave impedance, and (4)

$Z_S = \rho V_S$ is the S-wave impedance. (5)

The velocities can be related to impedance in the following manner;

$\lambda\rho = Z_P^2 - 2Z_S^2$, and (6)

$\mu\rho = Z_S^2$. (7)

Similarly

$\upsilon = \frac{V_P^2 - 2V_S^2}{2(V_P^2 - V_S^2)}$ is the Poisson's ratio, and (8)

$E = \frac{\rho V_S^2(3V_P^2 - 4V_S^2)}{(V_P^2 - V_S^2)}$ is the Young's modulus. (9)

Microseismic Data: Monitoring the Hydraulic Fracture Process

In an attempt to reduce the reliance on oil imports, several countries have been developing technologies to target production from unconventional sources shale gas and shale oil plays. (Schenk and Pollastro, 2002; EIA, 2011; Bruner and Smosna, 2011).

The development of these unconventional plays has led to further advances in drilling and completion technologies in order to mitigate environmental concerns, to optimize production and often, to allow drilling in urban areas. One example of such a development is to drill four or more horizontal and parallel wellbores from a single drilling site which reduces the environmental impact while also contacting increasingly larger reservoir volumes (Guo et al., 2012; Agrawal et al., 2012). However, for shales in particular, this may not be sufficient due to the extremely low permeabilities on the order of nano-Darcies (Bennett et al., 2006; Kale et al., 2010a, 2010b; Sondergeld et al., 2010; Bust et al., 2011). Economically viable production rates may therefore not be possible without some form of stimulation. Consequently, the industry has routinely completed these horizontal wells with one or more hydraulic fracture stages. Typical hydraulic fracture treatments tend to consist of more than three stages along the horizontal section of the wellbore (Bennett et al., 2006; Bruner and Smosna, 2011; EIA, 2011). The stages are designed to contact as much reservoir rock as possible thereby creating effective pathways between the reservoir rock and the wellbore (Daniels et al., 2007; Cipolla et al., 2008;Cipolla et al., 2012; Mayerhofer et al., 2010; Yu and Aguilera, 2012; Zimmer, 2011).

From an engineering standpoint, it is critical to assess the effectiveness of the stimulation treatment in order to optimize operating procedures for subsequent wells and shale gas plays and to control fracture growth. Although there are several techniques to map fracture growth, microseismic monitoring is increasingly being adopted in the industry (Waters et al., 2009) and is now commercially available. By utilizing a real time monitoring option and some diversion techniques it is also possible to have a high degree of control for fracture growth (Waters et al., 2009; Ramakrishnan et al., 2011). Additionally, it is always desirable to contact portions of the reservoir that have not been previously stimulated by another fracture stage or by fractures created from a neighboring well. Another objective of fracture mapping is to keep them away from water bearing zones or any other previously identified geo-hazards. All of these goals can be achieved with some level of success due to the real time mapping with the microseismic monitoring technique (Waters et al., 2009).

The microseismic mapping technique is a passive seismic imaging technique and records microseisms generated as a consequence of processes within the reservoir such as fluid flow, hydraulic fracturing, and enhanced oil recovery processes (McGillivray, 2005; Daugherty et al., 2009; Noe, 2011). These microseisms are characterized by a very small energy radiated in the form of seismic waves with frequencies in the range of 50 to 500 Hz (Hanks and Kanamori, 1979; Baig and Urbancic, 2010; Goodway, 2012). These seismic waves include shear and compressional events traveling at their associated velocities. For hydraulic fracturing processes, microseisms are generated when the rock fails in the shear mode (Cipolla et al., 2011; Cipolla et al., 2012). The shear failure may be a slip or tear failure and may be attributed to changes in the effective stress state (Cipolla et al., 2011). The stress state disturbance is generally caused by pore pressure changes due to any of the processes listed above.

The microseisms generated emit shear and compressional waves. By processing the data collected in the monitoring array, the location and magnitude of the generated microseisms can be determined (Bennett et al., 2006). The monitoring arrays comprises of multicomponent geophones. Figure 11 sketches a typical configuration of treatment and monitoring wells during a hydraulic fracture mapping process.

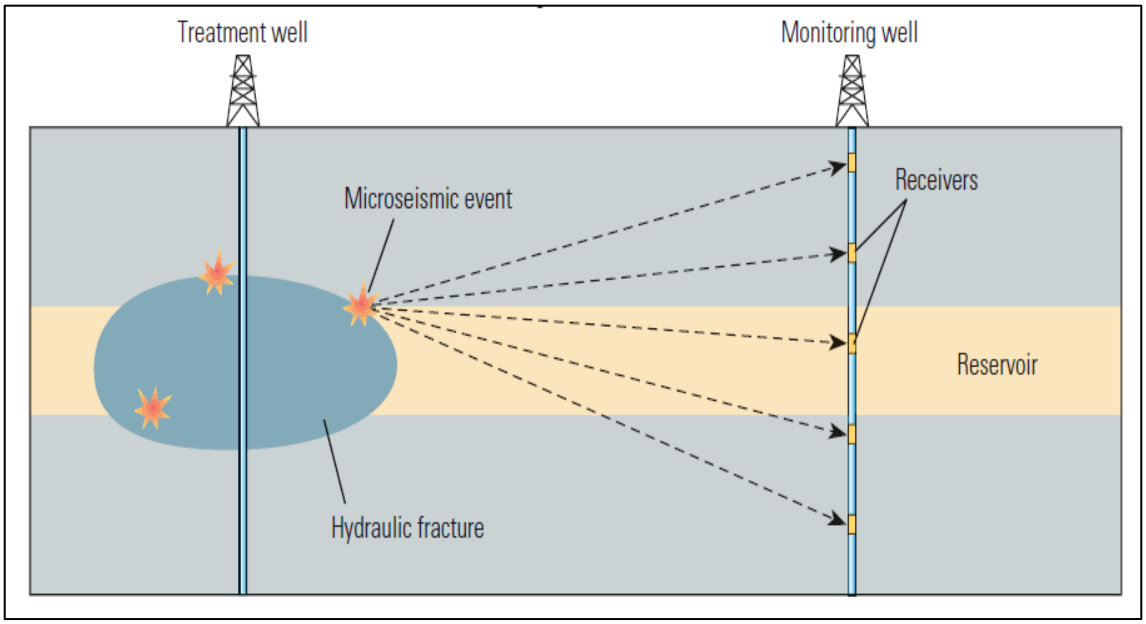

Figure 11. Sketch of a typical configuration of treatment and monitoring wells during a hydraulic fracture monitoring process. The data collected at the monitoring well are processed to determine the azimuth and distance from the receiver to the acoustic emission. (Bennett et al., 2006).

Although microseismic monitoring holds immense value for the petroleum industry, its application and interpretation is associated with several challenges. The most important aspect of quality control for acquiring microseismic data is related to the location of the monitoring array or monitoring well. The recorded data tend to be biased as smaller magnitude events are recorded near the monitoring array. In contrast, at large distances from the monitoring well, only larger magnitude events tend to be recorded. (Baig and Urbancic, 2010; Cipolla et al., 2011b; Cipolla et al., 2012; Shemeta and Anderson, 2010; Warpinski, 2009). This is due to seismic attenuation or energy dissipated per wavelength traveled in the reservoir. With this in mind, the industry practice is to retain only those points having magnitudes greater than the smallest magnitude recorded at the farthest point from the monitoring (Cipolla et al., 2011). The remaining points are typically discarded from the analysis due to potential problems such as overestimation of the stimulated volume and erroneous fracture geometry mapping. Retaining all the recorded points tends to result in mapped fractures that are elongated in the direction of the monitoring well and overestimated stimulated volumes (Cipolla et al., 2011).

Additionally, in order to ensure that the analysis is meaningful, microseismic data need to be filtered by the signal to noise ratio, SNR. When the SNR is very low, identifying the locations of the microseisms may be inaccurate and are often associated with large error ellipsoids which can render fracture mapping challenging. (Cipolla et al., 2011; Kidney et al., 2010).

Microseismic Data Available

There are microseismic data available for nine horizontal wells, among which the four wells (Wells A, B, C, and D) with production logs are included, and for two vertical wells. The microseismic data were recorded to monitor the fracturing process. Wells C and D were fractured simultaneously. Five fracture stages were practiced starting from toe (stage 1) to heel (stage 5) (Figure 13, 16, and 17). Once finished the fracturing of

Wells C and D, Wells A and B were fractured simultaneously as well. Similarly to wells C and D the fracture stages were placed from toe to heel but in this case only four stages were executed (Figure 13, 14, and 15).

The main information provided within the microseismic data includes the estimated XYZ coordinates, the local time of occurrence, and magnitude of the microseismic events. A weighting factor indicating the reliability of the microseismic moment magnitudes is also included. This reliability factor is calculated from the signal to noise ratio of the traces.

From the nine horizontal wells having microseismic data; Well H15 is completed in the Upper Barnett Shale and therefore, is not included in my analysis. Since Well H10 and Well H30 do not have magnitude readings in the microseismic data, they were excluded from my analysis as well.

Figure 12 shows a depth slice at 8090 ft., true vertical depth (TVD), which is the depth where Well B is completed, of ant tracked coherence. Figure 12 also shows the location of the monitor (vertical) wells V33, V82, V174, and V290 and the reminder six stimulated (horizontal) wells A, B, C, D, H3, and H18 along with the microseismic events recorded during the hydraulic fracturing.

Figure 13 shows the location of the microseismic events recorded during the hydraulic fracturing process of Wells A, B, C, and D. The size of the dots is proportional to the event magnitude and the color represents the fracture stage during which it was recorded. Figure 13 also shows the location of the monitoring wells. Well V174 served as the monitor well for Well A and Well C while Well V33 was the monitor well for Well B and Well D.

Figures 14, 15, 16, and 17 (Well A, B, C, and D correspondingly) show the same information displayed in Figure 13 discriminating the points by stimulated well.

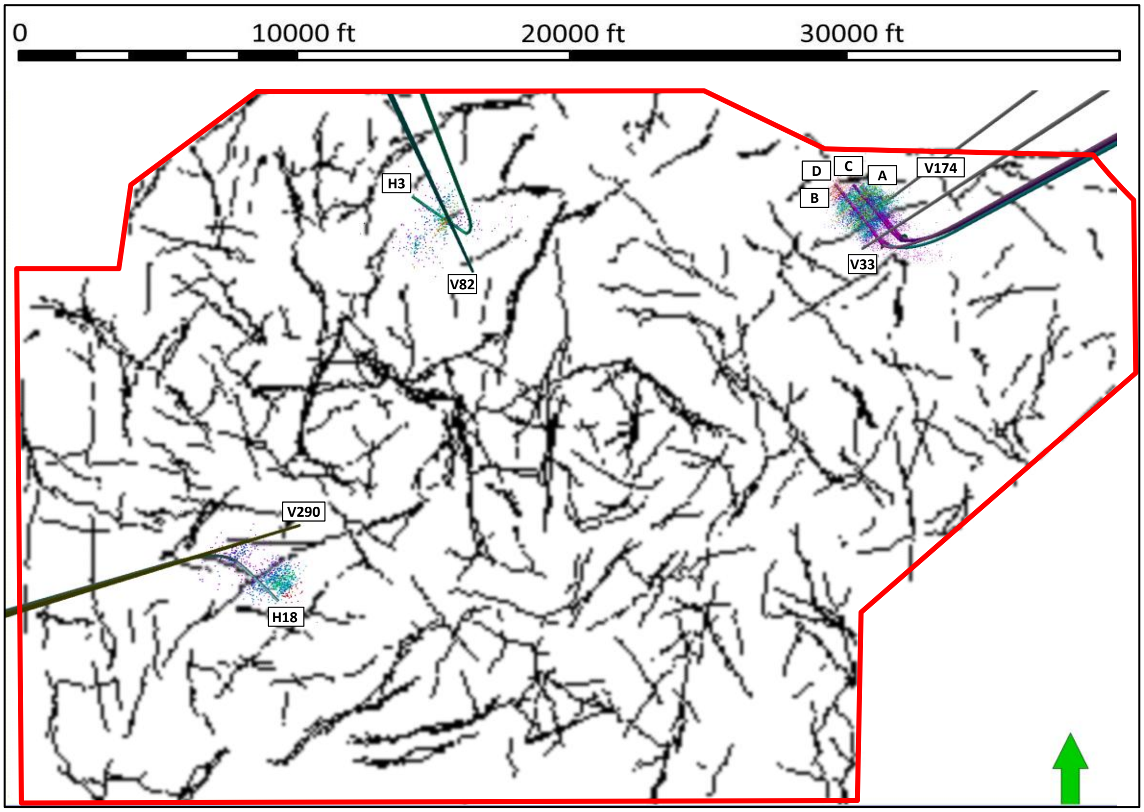

Figure 12. Depth slice (8090 ft.) of ant tracked coherence. Monitor (vertical) and treatment (horizontal) wells completed in the Lower Barnett Shale are displayed along with the microseismic data recorded during the hydraulic fracturing. Microseismic events are colored according to their stage.

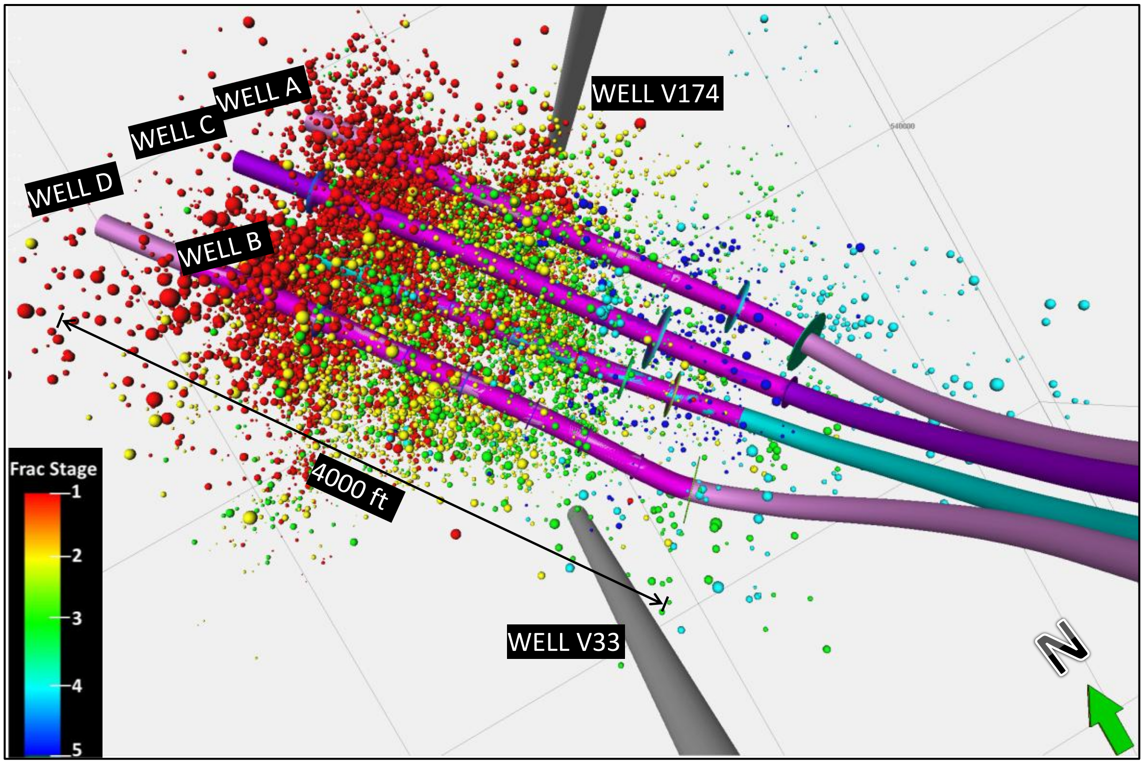

Figure 13. Location of the microseismic events recorded during the hydraulic fracturing process of Wells A, B, C, and D. The size of the dots is proportional to the event magnitude and the color represents the fracture stage during which they were recorded. The figure also shows the location of the monitoring wells. Well V174 served as the monitor well for Well A and Well C while Well V33 was the monitor well for Well B and Well D.

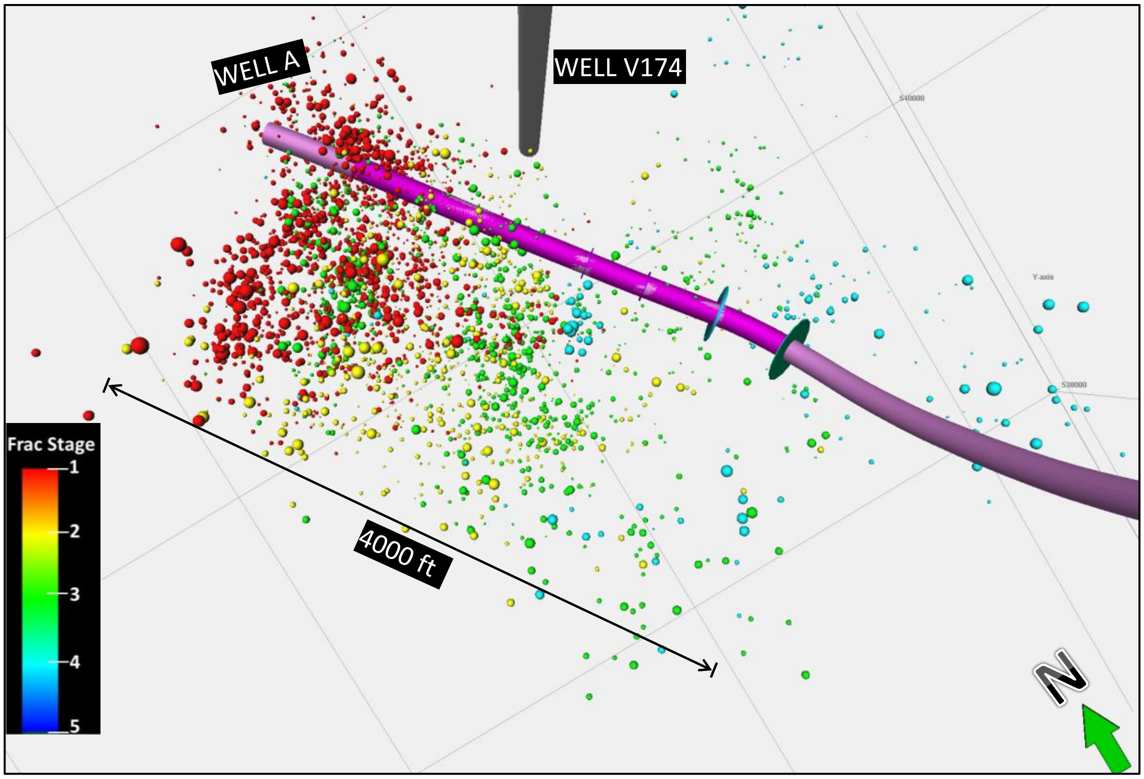

Figure 14. Location of the microseismic events recorded during the hydraulic fracturing process of Well A. The size of the dots is proportional to the event magnitude and the color represents the fracture stage during which they were recorded. Four fracture stages were initiated starting from toe to heel. Well V174 is the monitor well. Note the events are skewed to the west of the wellbore.

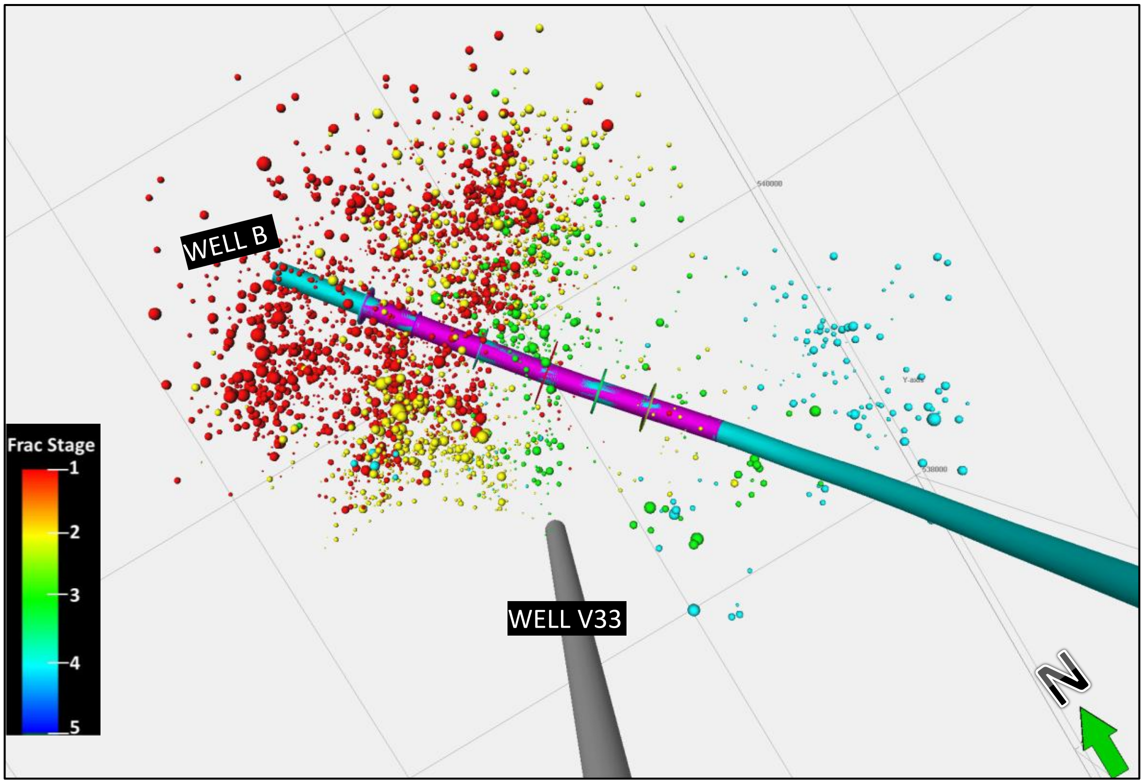

Figure 15. Location of the microseismic events recorded during the hydraulic fracturing process of Well B. The size of the dots is proportional to the event magnitude and the color represents the fracture stage during which they were recorded. Four fracture stages were initiated starting from toe to heel. Well V33 is the monitor well. Note the events are centered about the wellbore

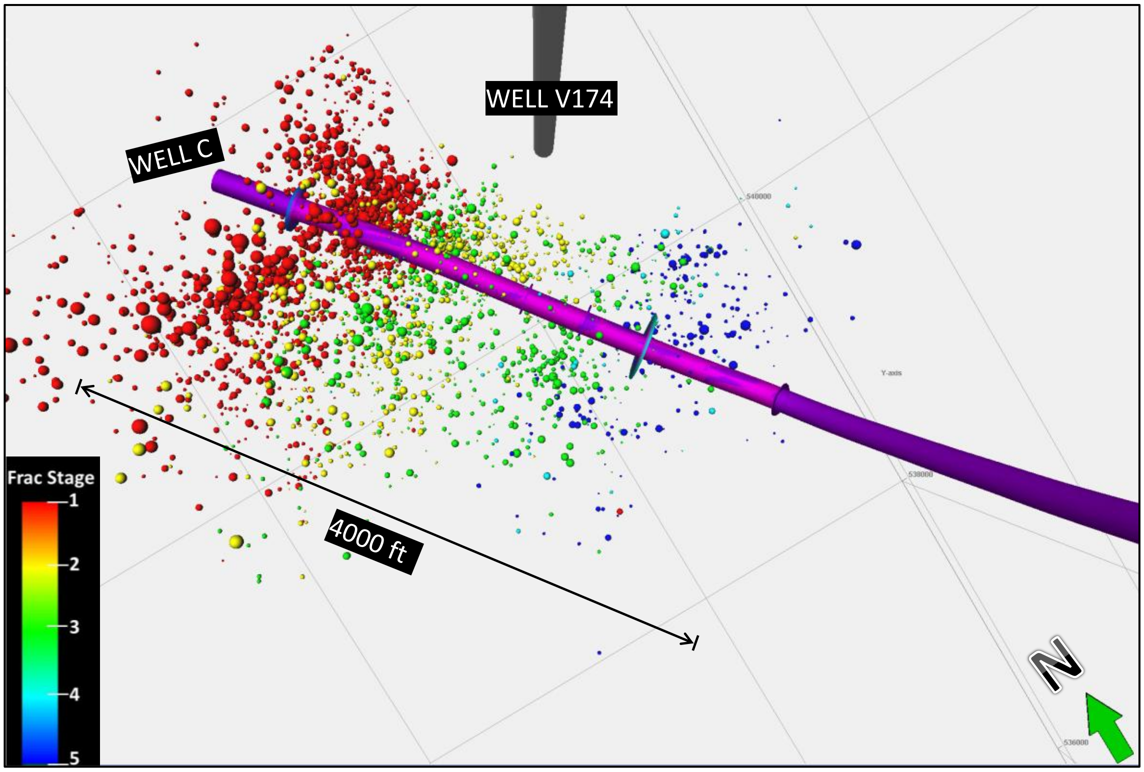

Figure 16. Location of the microseismic events recorded during the hydraulic fracturing process of Well C. The size of the dots is proportional to the event magnitude and the color represents the fracture stage during which they were recorded. Five fracture stages were initiated starting from toe to heel. Well V174 is the monitor well. Note the events are skewed to the west of the wellbore

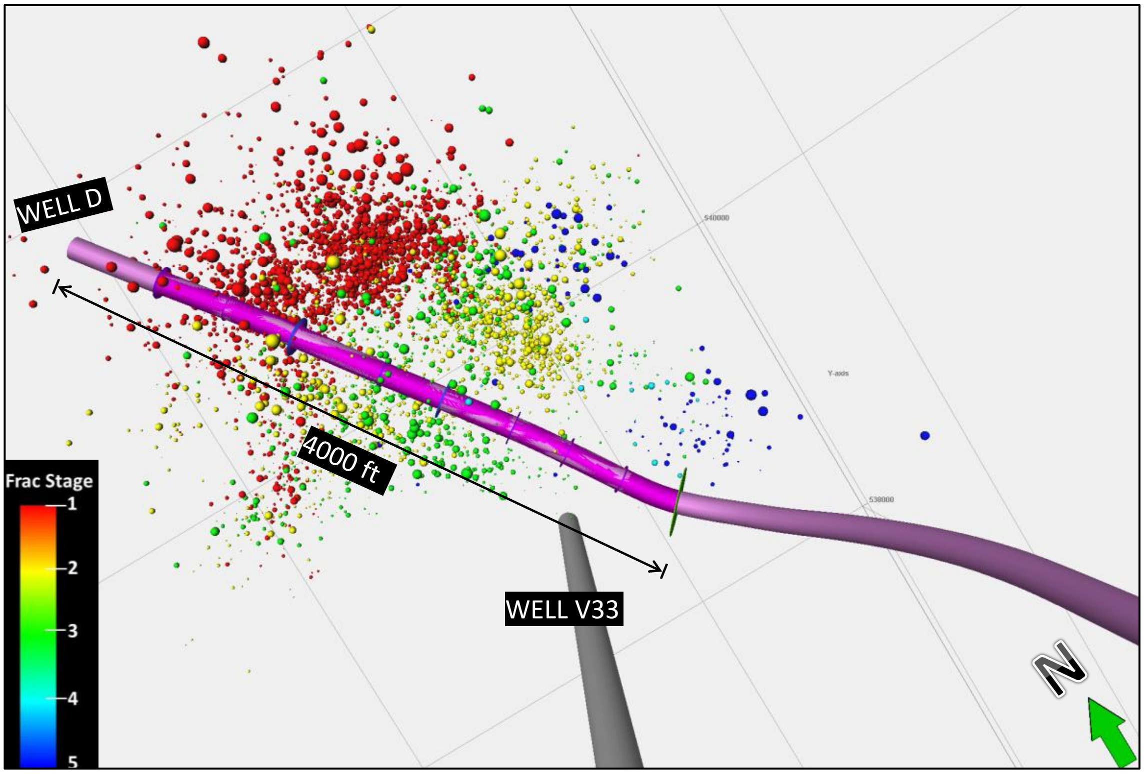

Figure 17. Location of the microseismic events recorded during the hydraulic fracturing process of Well D. The size of the dots is proportional to the event magnitude and the color represents the fracture stage during which they were recorded. Five fracture stages were initiated starting from toe to heel. Well V33 is the monitor well. Note the events are skewed to the east of the wellbore

Chapter 4

Microseismic Data Quality Control and Filtering

In this chapter, I describe the procedures used prior to interpretation of the microseismic data. I focus on the procedures behind data quality control and filtering in order to make the analysis more meaningful. As mentioned in Chapter 3, microseismic data analysis is susceptible to problems associated with sensor placement bias. Due to the location of the sensors and seismic attenuation, only larger magnitude events are recorded at locations distant from the monitor wells while a large number of small magnitude events are recorded close to the monitoring wells.

In this dataset, the raw microseismic data consisted of 51767 events registered in all the hydraulic fracturing processes available. Because of formatting issues and problems with missing pieces of information for a commercial microseismic analysis package, to use for data import, it was necessary to perform data preparation and pre-filtering with specially designed computer code which is provided in Appendix A. A brief description of the four subroutines is provided here.

The first subroutine reads and assigns variables to each and every one of the 51767 events available. The information available for each event includes: Well name, Stage (within the fracturing process), Event Density, Event Date, Event Time, Event TVD Subsea (ft.), Event X Coordinate (ft.), Event Y Coordinate (ft.), Moment Log (J), Vertical Distance (ft.), Azimuth (degree), Event Magnitude (Hanks and Kanamori, 1979 scale), Max Stress Azimuth (degree), Max Stress Inclination (degree), Measured Depth (ft.), Min Stress Azimuth (degree), Min Stress Inclination (degree), Polar Angle (degree), and Event Magnitude Reliability.

The second subroutine does three things. First, entries with missing data are deleted from the dataset and only points having all the relevant information such as the event magnitude, moment log and spatial coordinates are preserved. Second, it computes the distance of each recorded event from the observation array. The data are partitioned and grouped with the appropriate treatment well facilitating the creation of a scatter plot of magnitude versus distance to the monitor array for each well independently. These scatter plots provide information about the viewing limit for each fracture stage. In general terms, the viewing limit is the smallest magnitude microseismic event that can be seen at the farthest point from the monitor well. Third, based on the viewing limit previously determined, the subroutine removes all the events having moment magnitudes below the viewing limit for each well independently and redraws the refined scatter plots of distance versus magnitude. The new plots now show an even distribution of the events free of the bias inherent to the location of the monitor well. Figures 27 to 35 show the filtered microseismic plots for each well. Table 4 summarizes the viewing limit and the list of figures corresponding to each stimulated well.

Figures 18 to 26 show the plots and the corresponding viewing limit for the stimulated wells. From Figure 18 I can observe that the viewing limit in Well H3 is -1.7 because this is the smallest magnitude that is recorded at the farthest point from the monitor well (approximately at a distance of 3300 ft.). From Figure 19, considering only the data from stage 1, the viewing limit in H15 is -1.9; from Figure 20, the viewing limit in Well H18 is -1.3; from Figure 21 the viewing limit in Well A is -2.4; from Figure 22 the viewing limit in Well B is -2.7; from Figure 23 the viewing limit in Well

C is -2.5; from Figure 24 the viewing limit in Well D is -2.7; from Figure 25 the viewing limit in Well V258 is -2.1 and from Figure 26 the viewing limit in Well V259 is -1.5. Figure 19 for Well H15 is the only one not following the expected behavior of monotonically increasing event magnitudes recorded as the distance from the monitor well increases. Based on discussions with the operator, the well was hydraulically fractured in two stages and the locations of the monitor arrays were different for each of the treatments.

The third subroutine exports the filtered data into a spread sheet with the information corresponding to each well in a different tab in the file. The data can now be read into the interpretation package.

Table 4. Summary of microseismic viewing limit and list of the corresponding figures for each stimulated well.

WELL	VIEWING LIMIT	RAW MICROSEISMIC	FILTERED MICROSEISMIC	OBSERVATION
A	-2.4	Figure 21	Figure 30	
B	-2.7	Figure 22	Figure 31	
C	-2.5	Figure 23	Figure 32	
D	-2.7	Figure 24	Figure 33	
H10				The microseismic Magnitudes corresponding to Well H10 were not recorded
H15	-1.9	Figure 19	Figure 28	This well is completed in the Upper Barnett
H18	-1.3	Figure 20	Figure 29	
H3	-1.7	Figure 18	Figure 27	
H30				The microseismic Magnitudes corresponding to Well H30 were not recorded
V258	-2.1	Figure 25	Figure 34	Vertical well located in the south-east limit of the seismic survey
V259	-1.5	Figure 26	Figure 35	Vertical well located in the south-east limit of the seismic survey

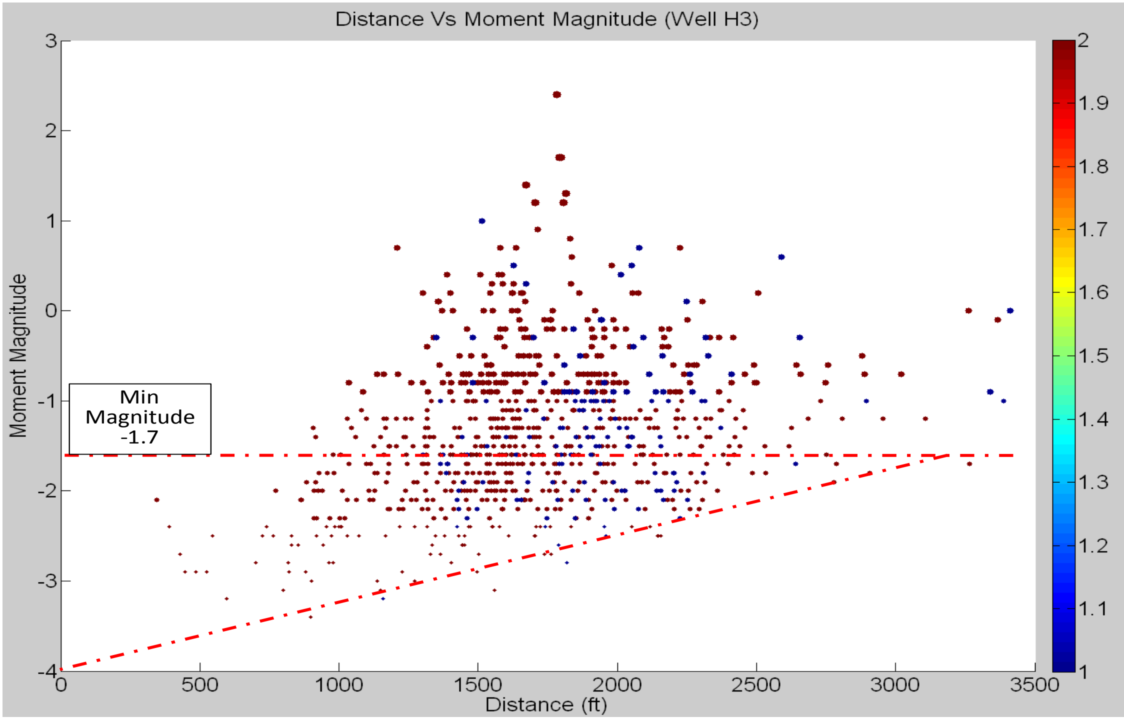

Figure 18. Microseismic event distance versus magnitude crossplot for Well H3. The color bar indicates the stage during the fracturing process when the events were recorded. The size of the dots indicates the moment magnitude.

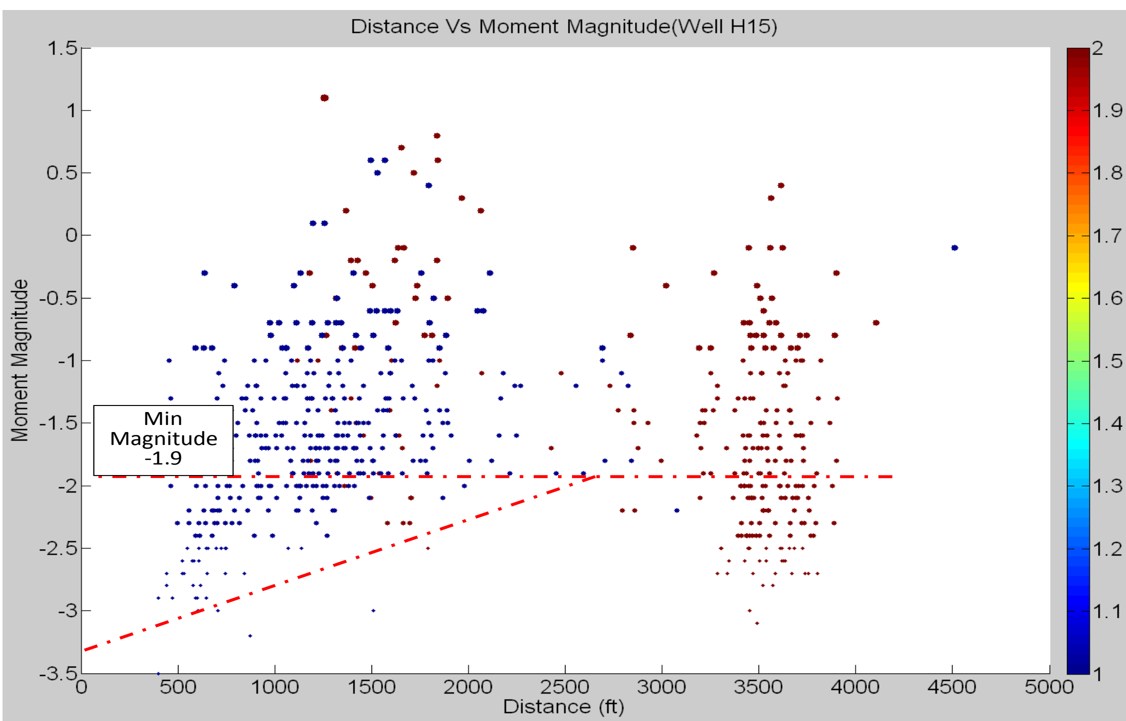

Figure 19. Microseismic event distance versus magnitude crossplot for Well H15. The color bar indicates the stage during the fracturing process when the events were recorded. The size of the dots indicates the moment magnitude.

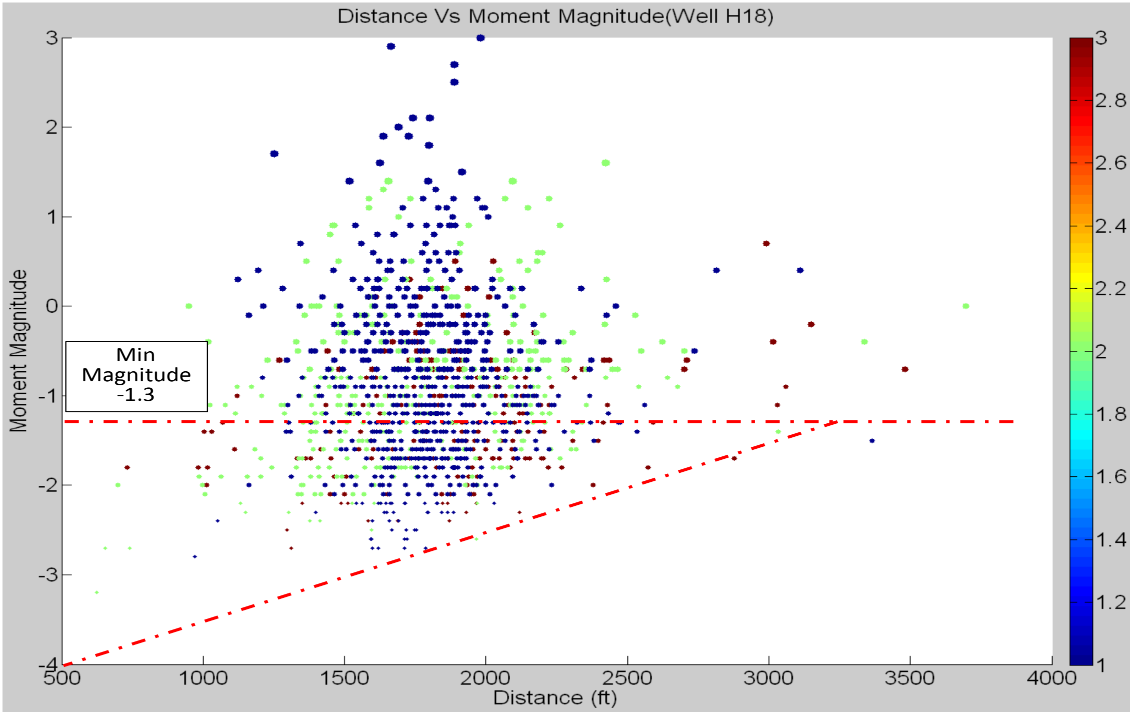

Figure 20. Microseismic event distance versus magnitude crossplot for Well H18. The color bar indicates the stage during the fracturing process when the events were recorded. The size of the dots indicates the moment magnitude.

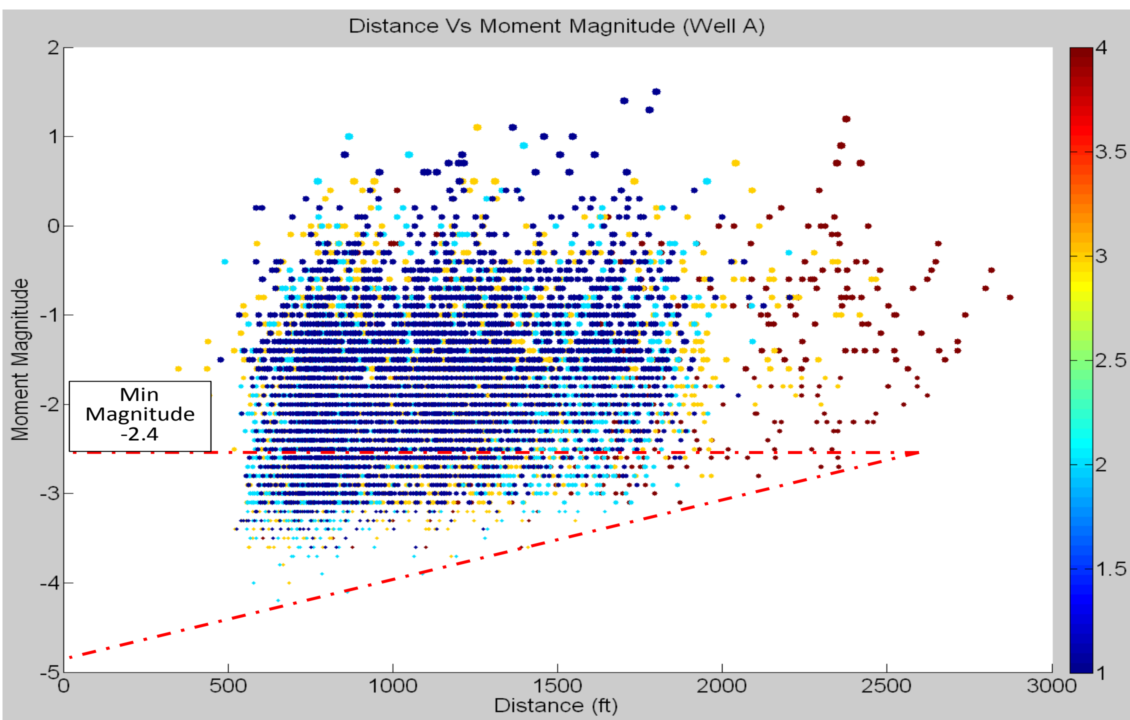

Figure 21. Microseismic event distance versus magnitude crossplot for Well A. The color bar indicates the stage during the fracturing process when the events were recorded. The size of the dots indicates the moment magnitude.

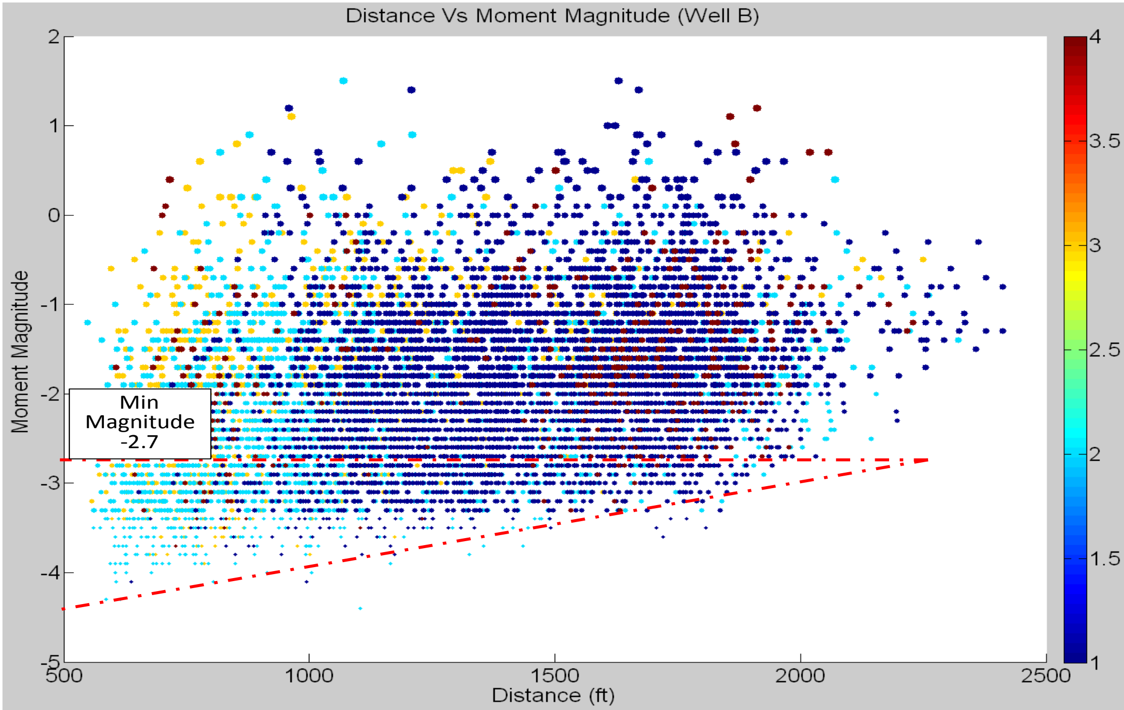

Figure 22. Microseismic event distance versus magnitude crossplot for Well B. The color bar indicates the stage during the fracturing process when the events were recorded. The size of the dots indicates the moment magnitude.

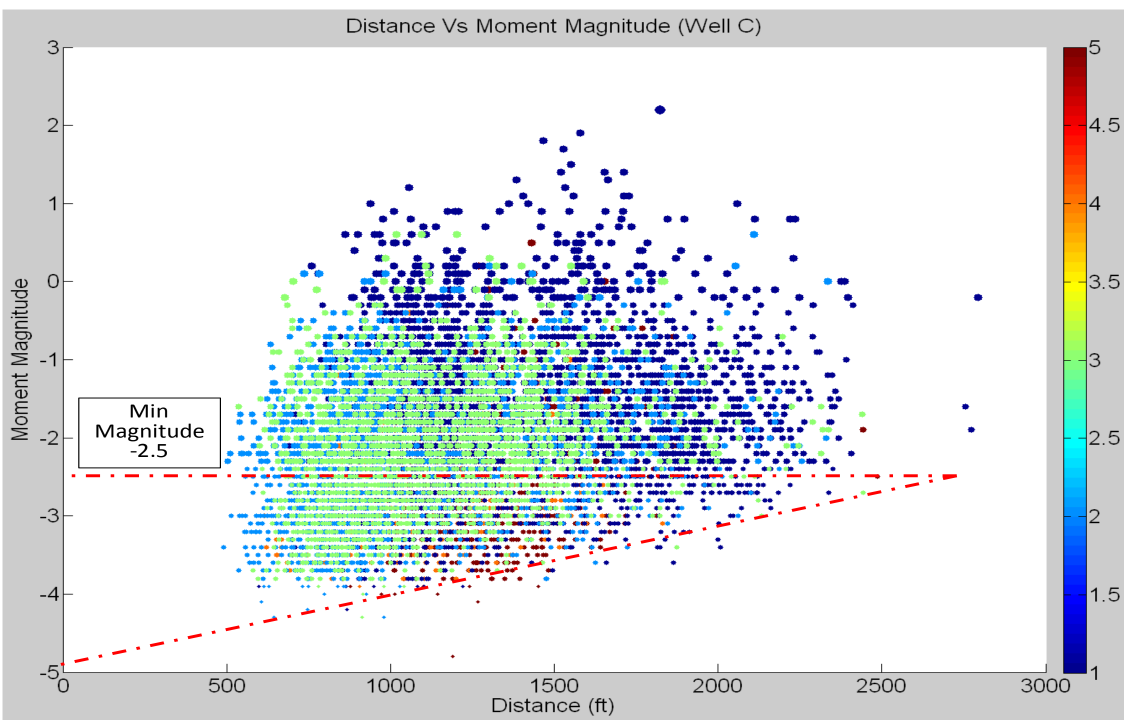

Figure 23. Microseismic event distance versus magnitude crossplot for Well C. The color bar indicates the stage during the fracturing process when the events were recorded. The size of the dots indicates the moment magnitude.

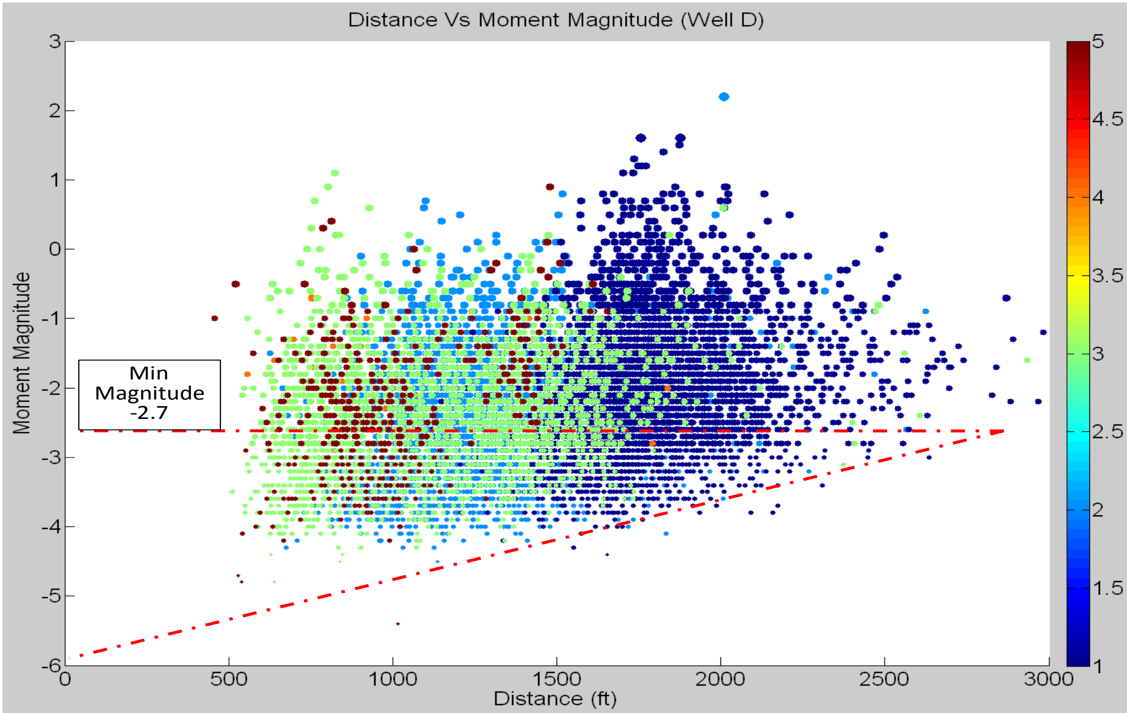

Figure 24. Microseismic event distance versus magnitude crossplot for Well D. The color bar indicates the stage during the fracturing process when the events were recorded. The size of the dots indicates the moment magnitude.

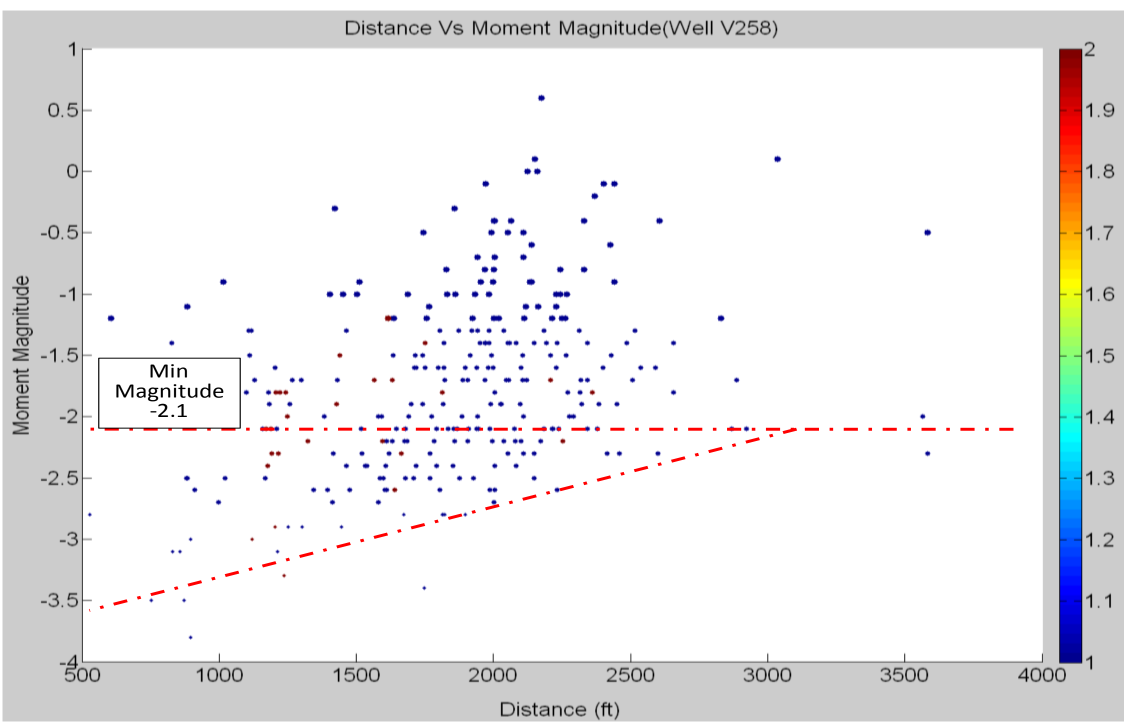

Figure 25. Microseismic event distance versus magnitude crossplot for Well V258. The color bar indicates the stage during the fracturing process when the events were recorded. The size of the dots indicates the moment magnitude.

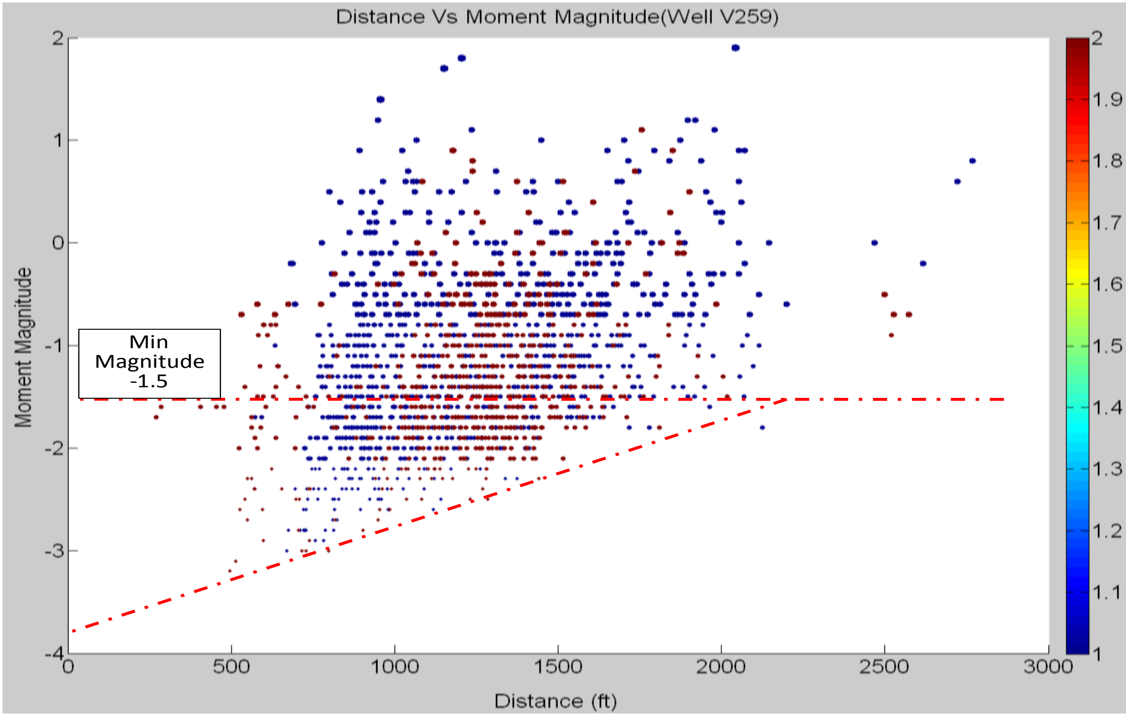

Figure 26. Microseismic event distance versus magnitude crossplot for Well V259. The color bar indicates the stage during the fracturing process when the events were recorded. The size of the dots indicates the moment magnitude.

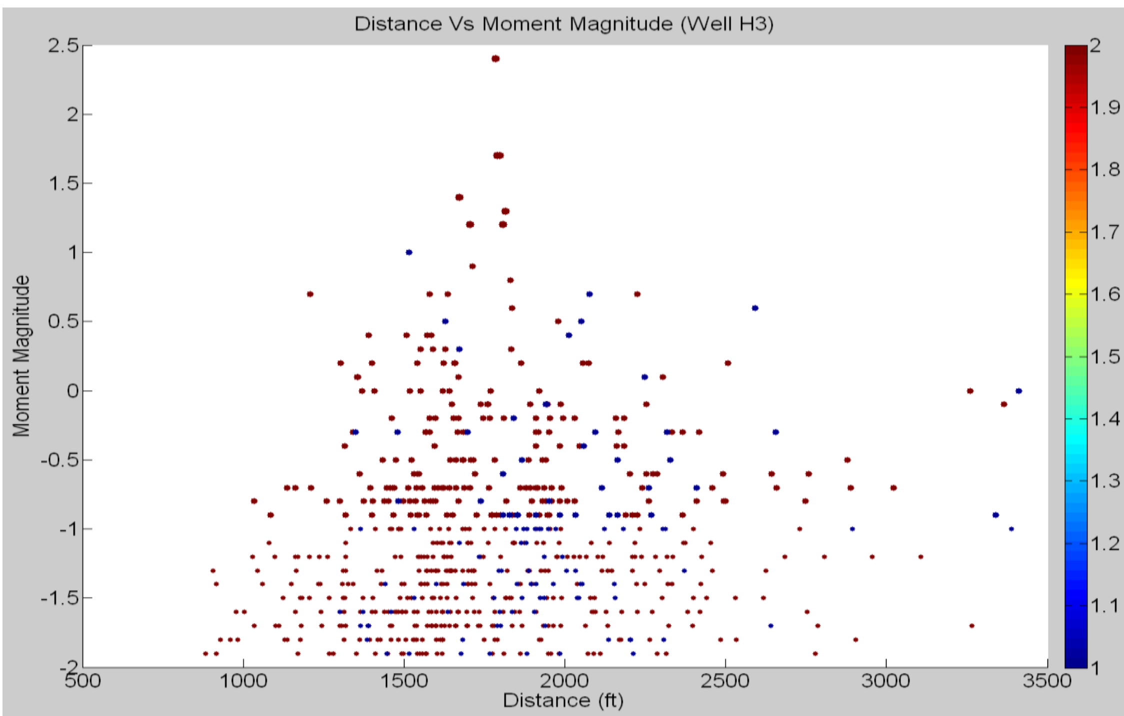

Figure 27. Microseismic event distance versus magnitude crossplot for Well H3 after removing the location biased points. The color bar indicates the stage during the fracturing process when the events were recorded. The size indicates the moment magnitude. The color bar indicates the fracturing stage.

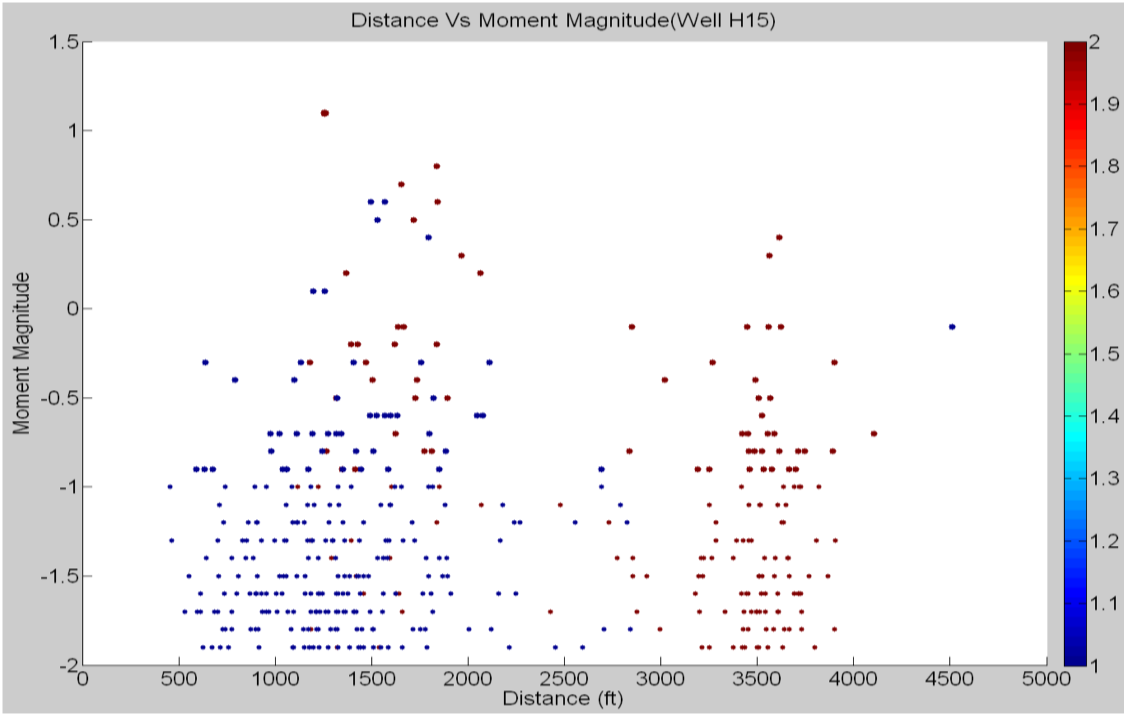

Figure 28. Microseismic event distance versus magnitude crossplot for Well H15 after removing the location biased points. The color bar indicates the stage during the fracturing process when the events were recorded. The size indicates the moment magnitude. The color bar indicates the fracturing stage.

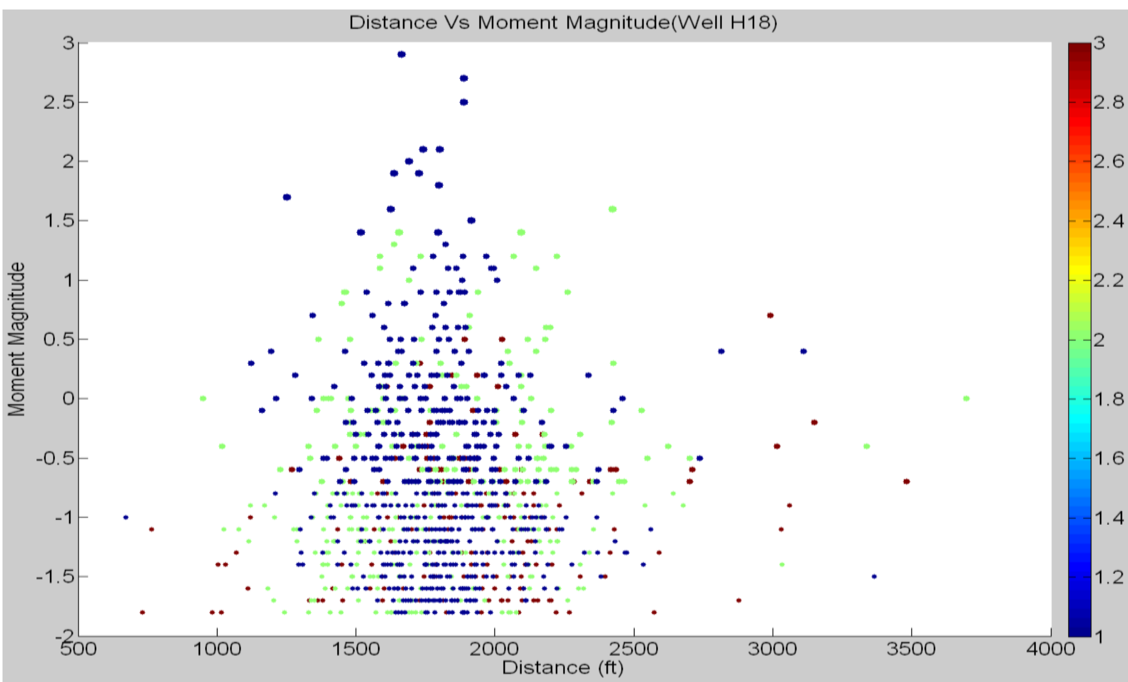

Figure 29. Microseismic event distance versus magnitude crossplot for Well H18 after removing the location biased points. The color bar indicates the stage during the fracturing process when the events were recorded. The size indicates the moment magnitude. The color bar indicates the fracturing stage.

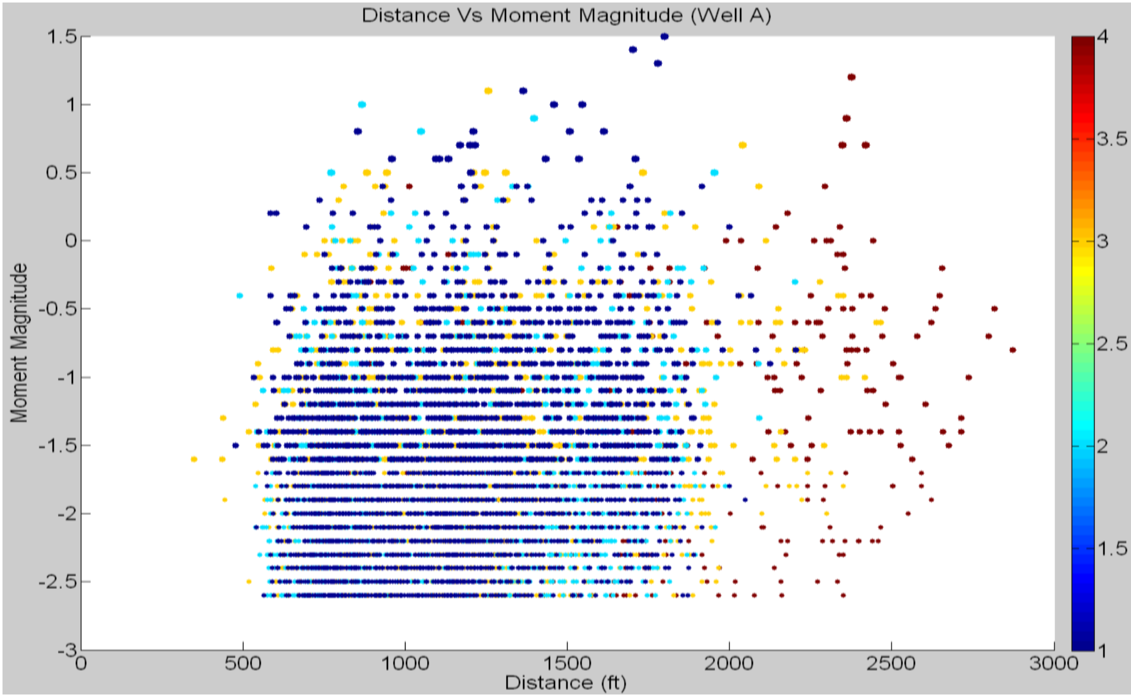

Figure 30. Microseismic event distance versus magnitude crossplot for Well A after removing the location biased points. The color bar indicates the stage during the fracturing process when the events were recorded. The size indicates the moment magnitude. The color bar indicates the fracturing stage.

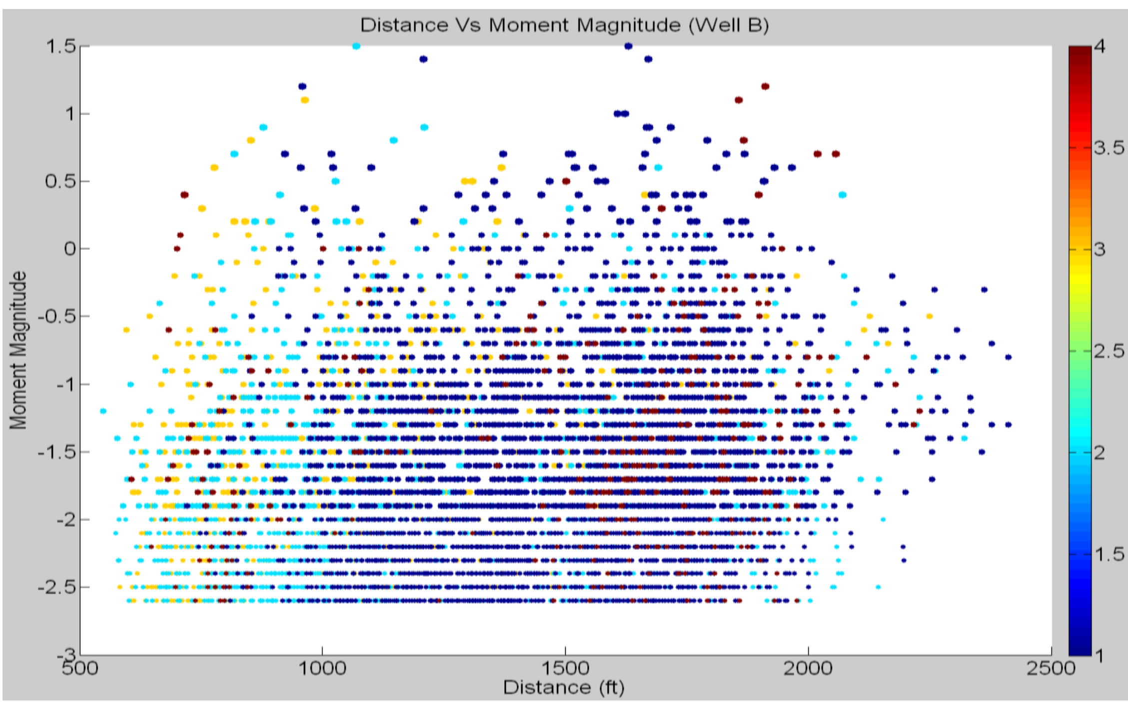

Figure 31. Microseismic event distance versus magnitude crossplot for Well B after removing the location biased points. The color bar indicates the stage during the fracturing process when the events were recorded. The size indicates the moment magnitude. The color bar indicates the fracturing stage.

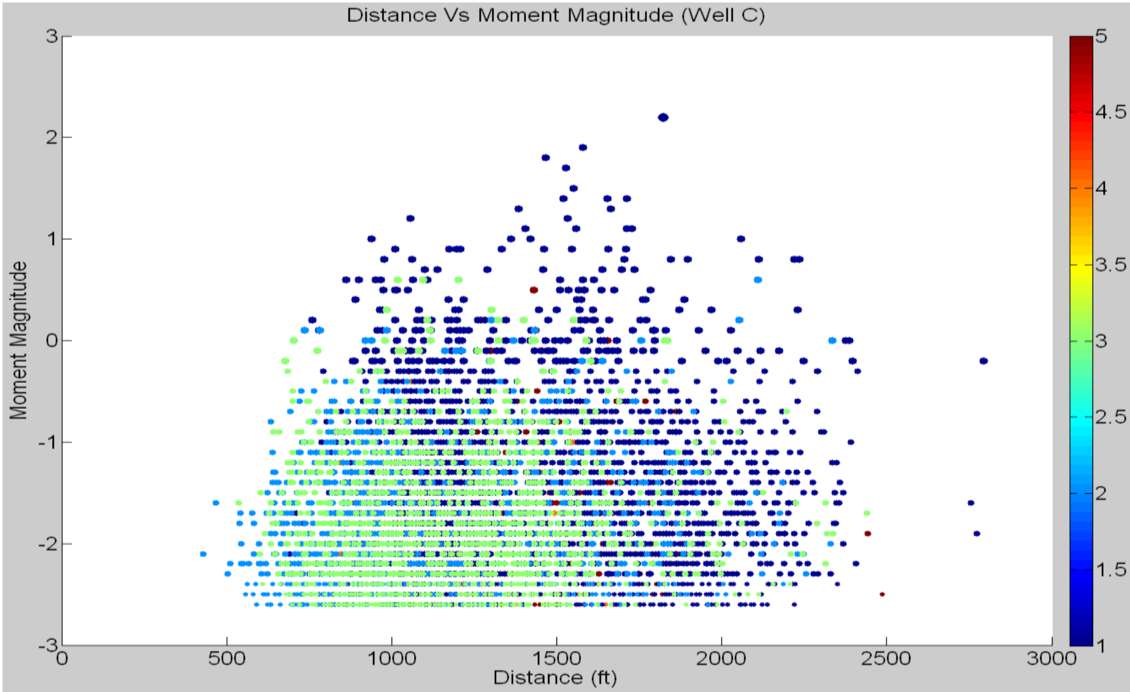

Figure 32. Microseismic event distance versus magnitude crossplot for Well C after removing the location biased points. The color bar indicates the stage during the fracturing process when the events were recorded. The size indicates the moment magnitude. The color bar indicates the fracturing stage.

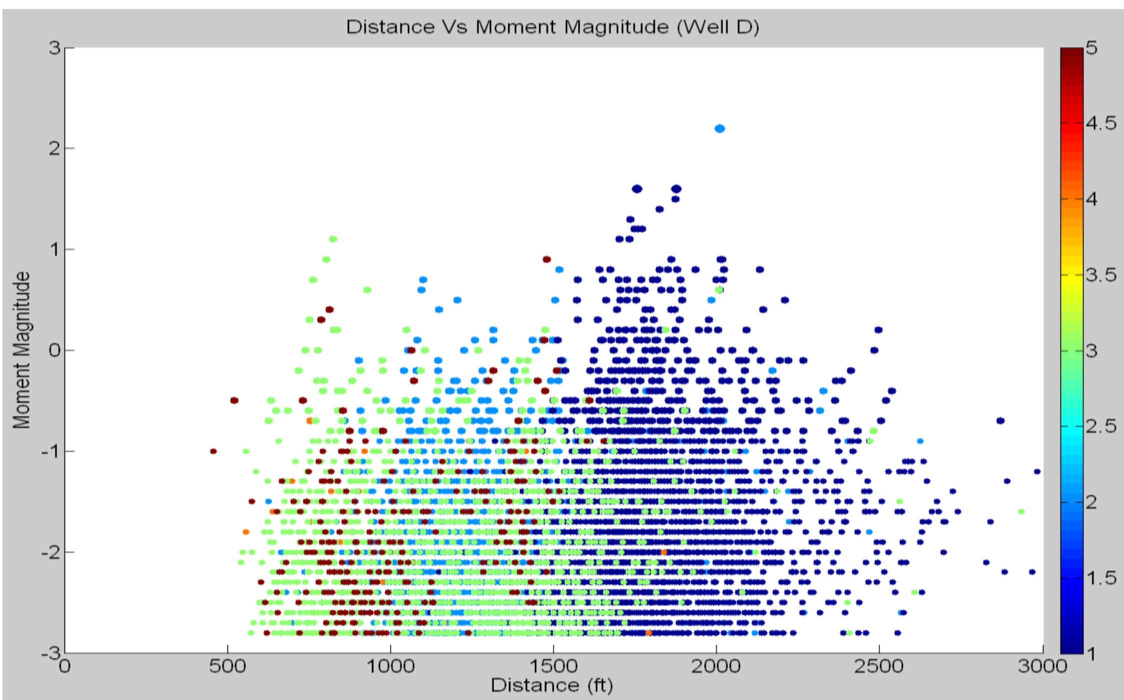

Figure 33. Microseismic event distance versus magnitude crossplot for Well D after removing the location biased points. The color bar indicates the stage during the fracturing process when the events were recorded. The size indicates the moment magnitude. The color bar indicates the fracturing stage.

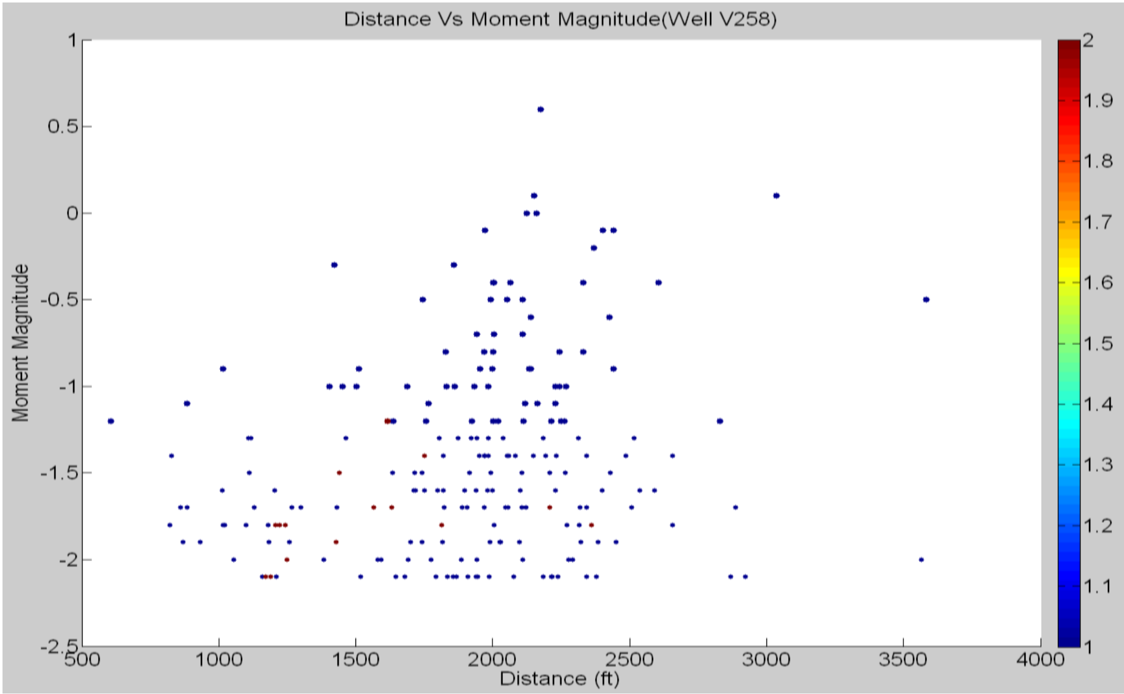

Figure 34. Microseismic event distance versus magnitude crossplot for Well V258 after removing the location biased points. The color bar indicates the stage during the fracturing process when the events were recorded. The size indicates the moment magnitude. The color bar indicates the fracturing stage.

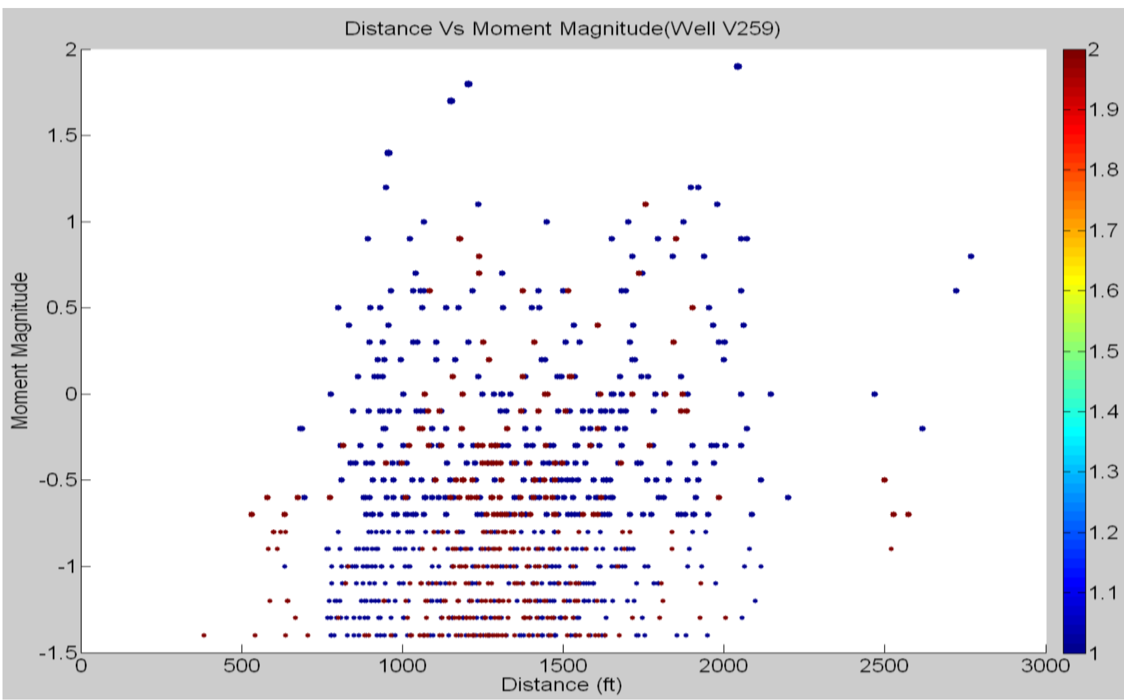

Figure 35. Microseismic event distance versus magnitude crossplot for Well V259 after removing the location biased points. The color bar indicates the stage during the fracturing process when the events were recorded. The size indicates the moment magnitude. The color bar indicates the fracturing stage.

Chapter 5

Methodology, Results, and Analysis

Methodology

Perez et al. (2011) developed “heuristic” rock physics templates that can be used to guide the interpretation of seismically inverted properties in unconventional reservoirs. The particular case reported is for a shale varying in composition from 60/40% quartz/clay to 100% quartz and porosity varying from 0% to 20% (Figure 36), but the concept is valid for any other composition. On the Lambda-rho/Mu-rho cross plot, the gas-in-place will track the porosity increase. The change in rock composition is also directly related to the brittleness of the rock, with quartz-rich rocks being brittle and clay and carbonate-rich rocks ductile. The brittleness of the rock controls the effectiveness of the hydraulic fracture completion. The Recovery factor (Rf) or fraction of hydrocarbons in place that can be produced vary accordingly. Brittle rocks can sustain propped fractures effectively, while ductile rocks will heal themselves against the proppant.

Based on the link between mineralogy and rock properties, plus the gas rates and rock properties associated to each producing zone (Figures 43 to 46), I found that seismically inverted Poisson’s ratio is an excellent discriminator between brittle and ductile zones in the Lower Barnett. Brittle zones exhibit low values of Poisson’s ratio (high completion efficiency-high gas rates) while on the other end of the spectrum, ductile rocks exhibit high values of Poisson's ratio (low completion efficiency-low gas rates) (Figures 37 and 42).

Numerous workers have documented the relationship between elastic properties such as the Young's modulus and reservoir quality properties such as porosity and Total Organic Carbon (TOC). For example Takahashi and Tanaka (2010) showed that both static as well as dynamic Young's modulus exhibit an inverse relationship to porosity in soft sedimentary rocks. Kumar et al. (2012) showed that in some shale plays there is an inverse relationship between Young's modulus and porosity, TOC, and clay content. They carried out nano-indentation tests on samples from the Woodford Shale, the Haynesville Shale, the Eagle Ford Shale, and the Barnett Shale; finding similar trends for all plays. Based on these previous studies and based on the total gas production per well and the average rock properties associated to the near wellbore rock (Table 5 and Figures 43 to 46), I also found very reasonable to use the seismically inverted Young's modulus as an indicator of rock richness.

Using iso-Poisson's ratio lines as lines of similar mineralogy composition, and then I can expect that the variation in the Young's modulus along these lines is a consequence of the TOC and the porosity. Therefore, fixing the value of the Poisson's ratio, rich rocks will exhibit lower values of Young's modulus while poor, low-porosity rocks, will show high values of Young's modulus (Figure 38).

Cross plots in Figures 37, 38, and 39 represent the seismically inverted rock properties of the Lower Barnett Shale across the entire seismic survey. These properties where computed from the shear and compressional wave velocities according to equations 6, 7, 8, and 9 in Chapter 3. To compute the Young's modulus in equation 9, a 2.5 g/cm^3 density value representative of the Lower Barnett was used. To create these plots, the seismic data were resampled into a geologic model discretized into 792 x 540 x 532 (xyz) grid cells. Due to high the number of cells (~2.3 x 10^8), the number of operations and the amount of memory required to storage the resampled data, the most suitable method to achieve the resampling in the interpretation package is called *closest point*. In this method each property cell will be contributed to only by the closest (or most central) seismic cell.

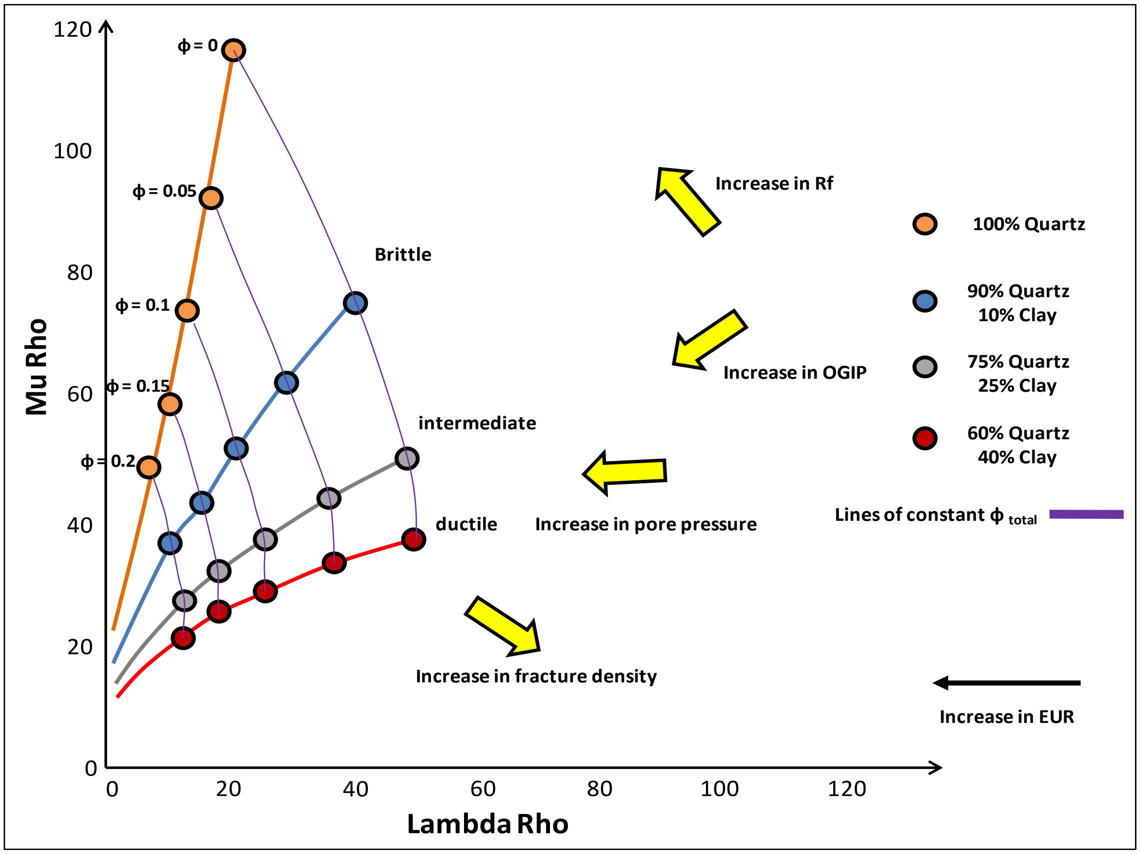

Figure 36. Heuristic template to interpret seismic, well log, or laboratory rock properties in terms of EUR, Original Gas in place (OGIP), recovery factor (Rf), pore pressure, and fracture density. After Perez et al. (2011).

This method is computationally efficient, but since it is considering only the closest seismic cell, a small amount (less than 1%) of spurious data resulted in the resampled volume. This is why in Figure 39, there are points classified as Group "0" falling in the Group 1, Group 2 or Group 3 regions. The same observation is valid for any of the other three groups. The definition of each one of these groups follows.

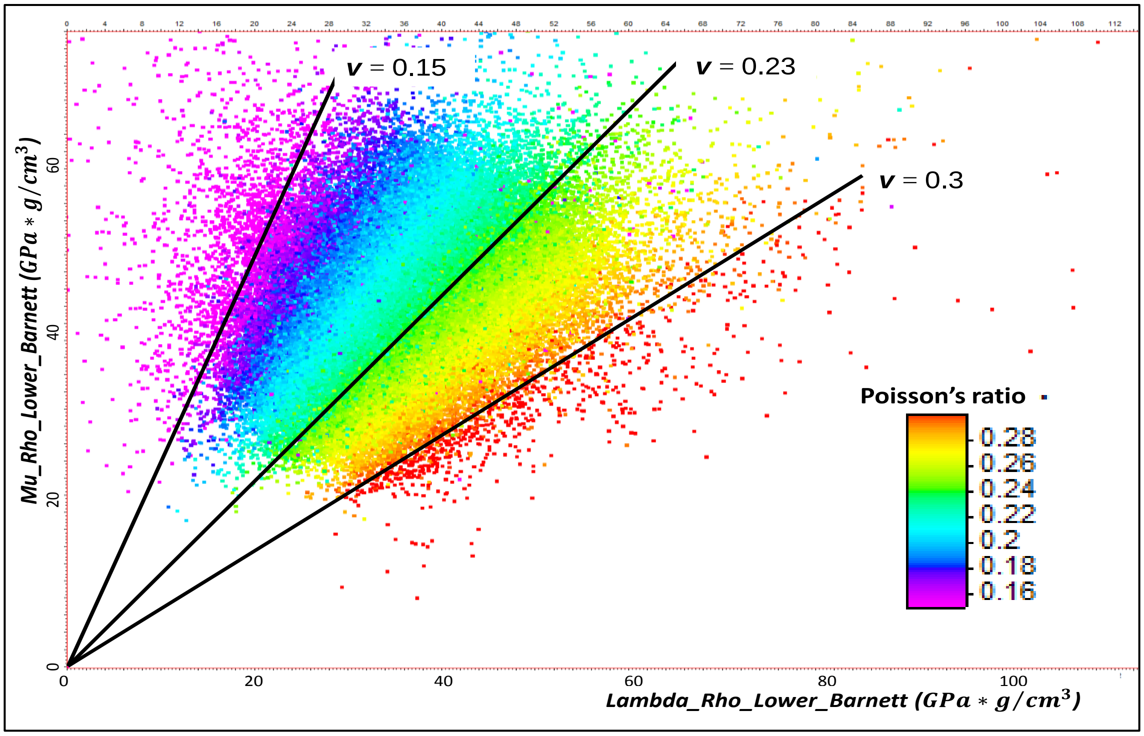

Figure 37. Lambda-rho/Mu-rho cross plot for the Lower Barnett Shale. Color indicates the Poisson's ratio, *ν*. Lines of fixed Poisson's ratio converge at the origin.

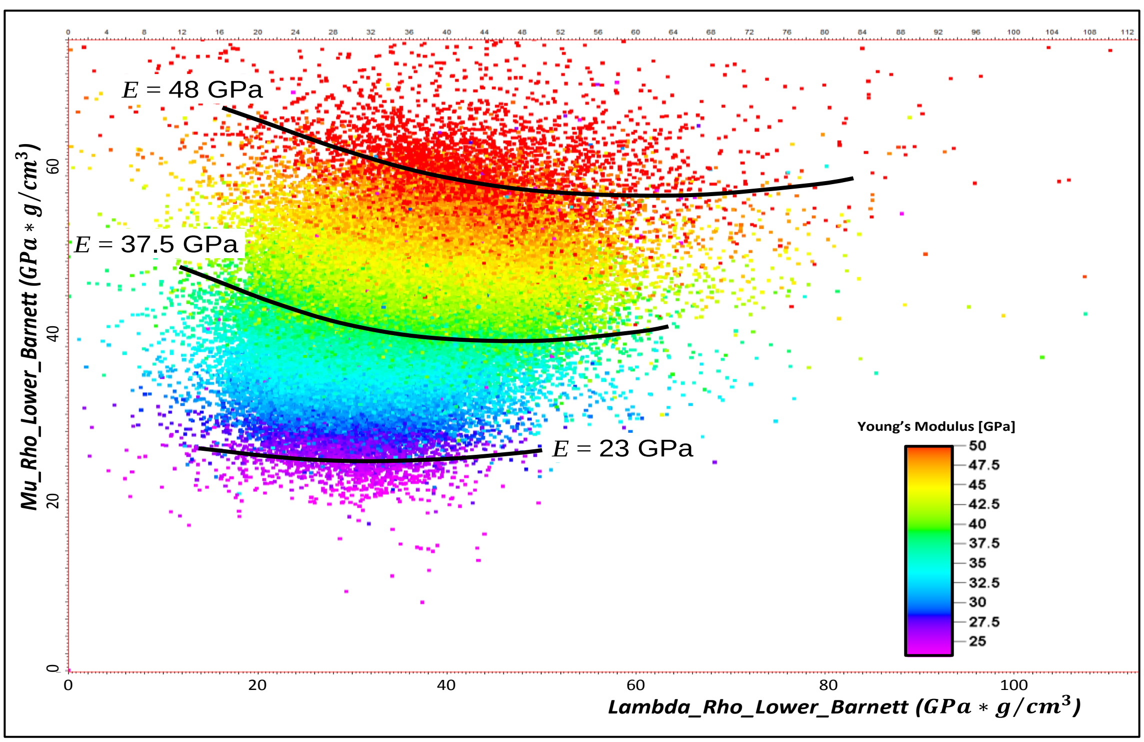

Figure 38. Seismic Lambda-rho/Mu-rho crossplot for the Lower Barnett Shale. Color indicates the Young's modulus, *E*, decreasing towards the origin.

Using the Young's modulus (Figure 38) and the Poisson's ratio (Figure 37) on the Lambda-rho/Mu-rho cross plot, I propose the following reservoir quality classification (Figure 39): Group "0" or Brittle and Rich (red points) are those portions of the Barnett Shale having low values of Poisson's ratio and low values of Young's modulus; Group 1 or Rich and Ductile (yellow points) are those regions of the shale play characterized by high values of Poisson's ratio and low values of Young's modulus; in Group 2 or Brittle and Poor (green points) fall all portions of the shale play exhibiting low values of Poisson's ratio and high values of Young's modulus; and Group 3 or Ductile and Poor (blue points) are those parts of the shale play with high Poisson's ratio and high Young's modulus.

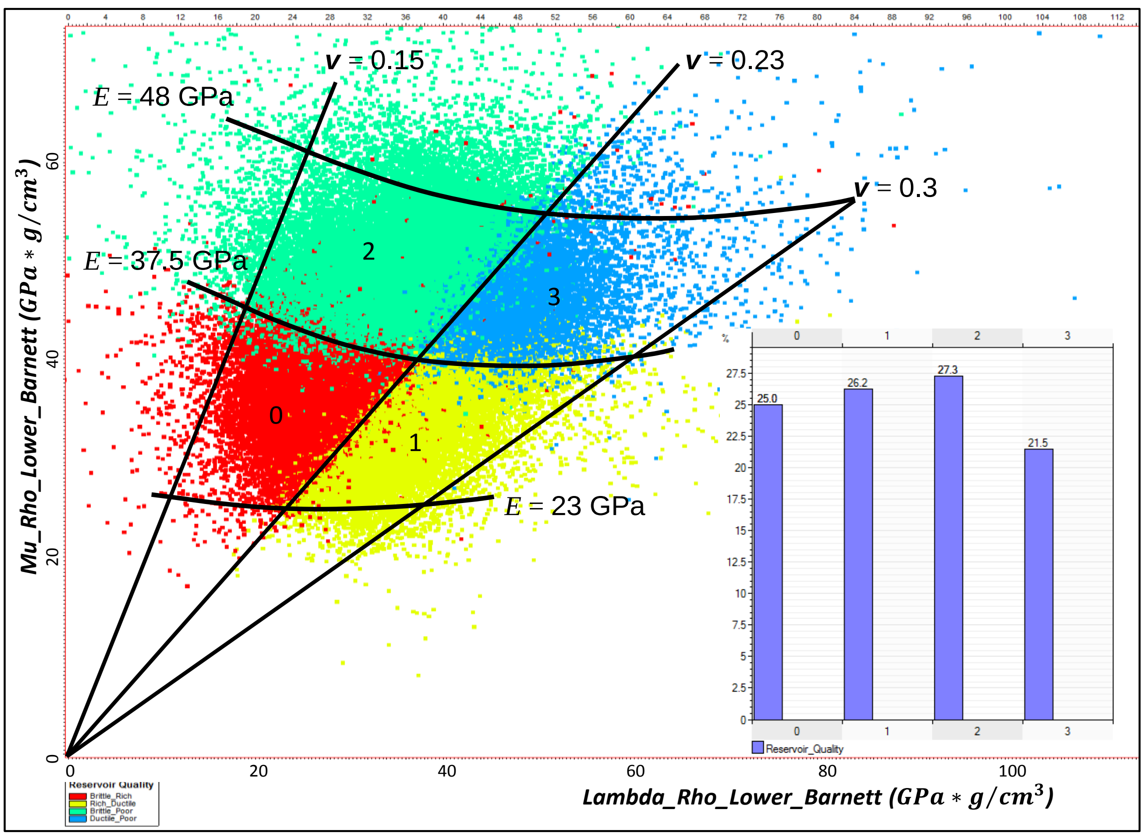

Figure 39. Lower Barnett reservoir quality classification based on seismically inverted rock properties. Four groups are defined: Group "0" or Brittle and Rich, Group 1 or Rich and Ductile, Group 2 or Brittle and Poor, and Group 3 or Ductile and Poor. Cut offs selected to make each group as even as possible.

Results and Analysis

On the Lambda-rho/Mu-rho cross plot, the production rates coming from each individual perforation show a clear clustering. The most prolific zones are clustered towards the origin with lower producing zones exhibiting higher values of Lambda-rho and Mu-rho (Figure 40).

Figure 41 shows the same plot as in Figure 40 but now the color represents the temperature of the well. Basically what can be observed is that the higher the gas rate, the higher the well temperature. In other words, the temperature in the well is being driven by the hot gas coming in. This is why WELL B, which produces the highest gas rates, is also the one exhibiting greatest well temperatures.

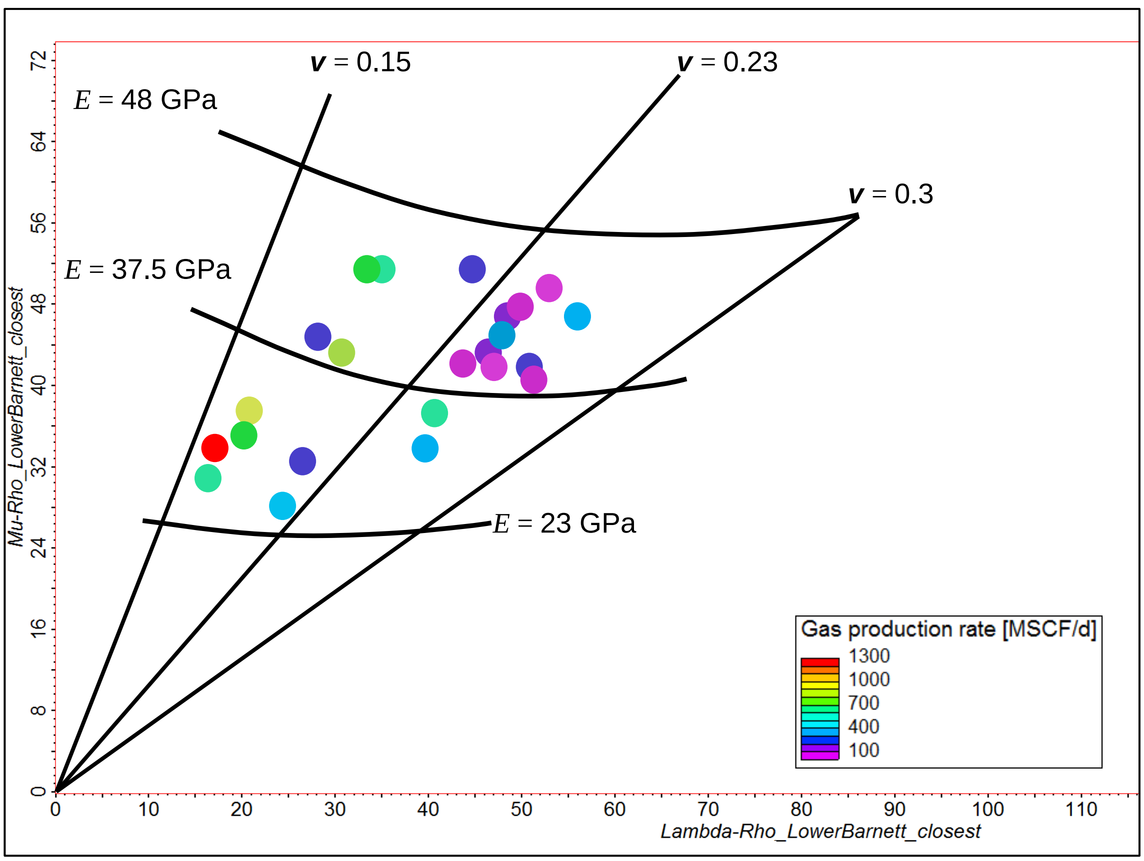

Figure 40. Seismic Lambda-rho/Mu-rho extracted along the wellbores with production logs. The color indicates the gas rate at each individual perforation.

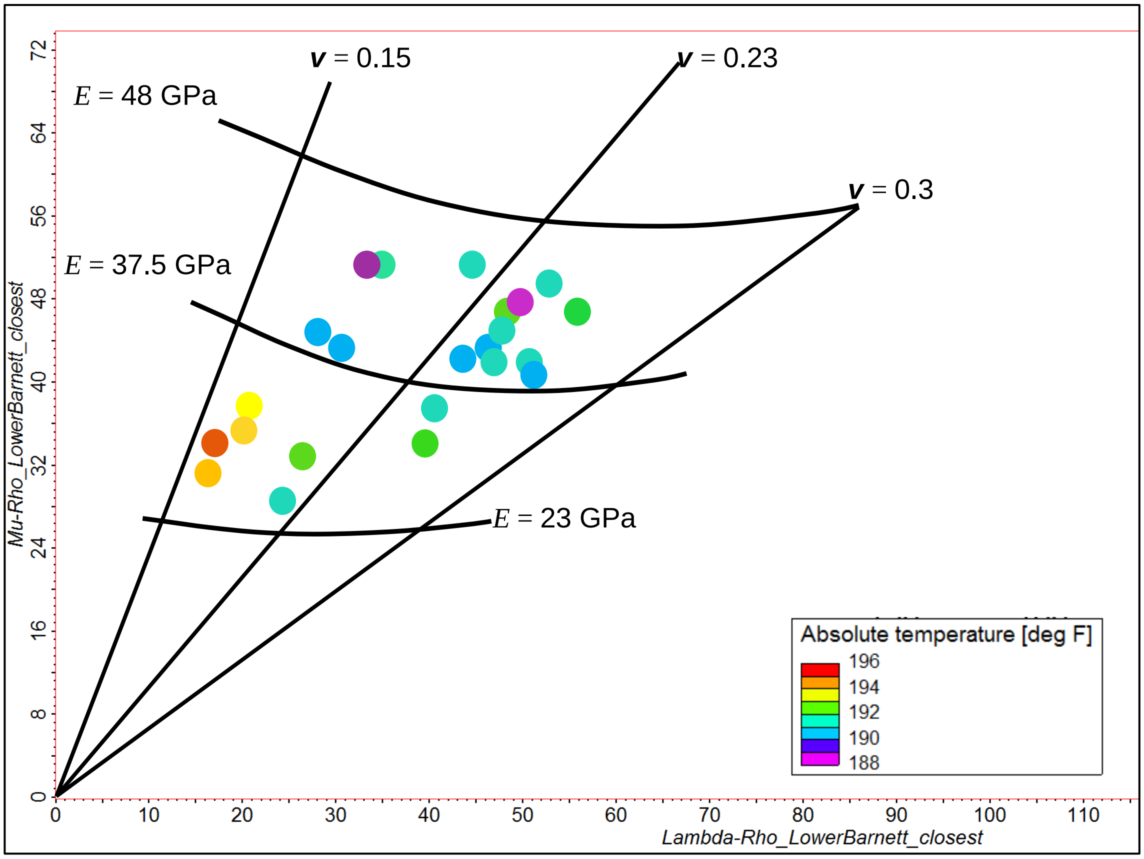

Figure 41. Seismic Lambda-rho/Mu-rho extracted along the wellbores with production logs. The color indicates the well temperature at each individual perforation.

Figure 42 shows the Lambda-rho/Mu-rho cross plot for the Lower Barnett displaying well defined color bands representing portions of the data having similar Poisson's ratio. The highest stage gas rates are located in portions of the wells where the Poisson's ratio is smaller. Conversely, the lowest individual gas rates are coming from zones where the rock is more ductile (where the Poisson's ratio is 0.24 or larger). The ovals are enclosing the observed values along the perforated zones in WELL A, WELL B, WELL C and WELL D.

Figure 42 also shows that there is a strong correlation between the Poisson's ratio and the well production rate. For example, WELL B, which is the one that exhibited the highest total gas rate during the production logging, is also the one whose Lambda-rho/Mu-rho points fall in the region with smallest Poisson's ratios. At least one of the points in WELL C and WELL D plot in the low Poisson's ratio region and the production rate for both of them is in between the production of WELL A and WELL B

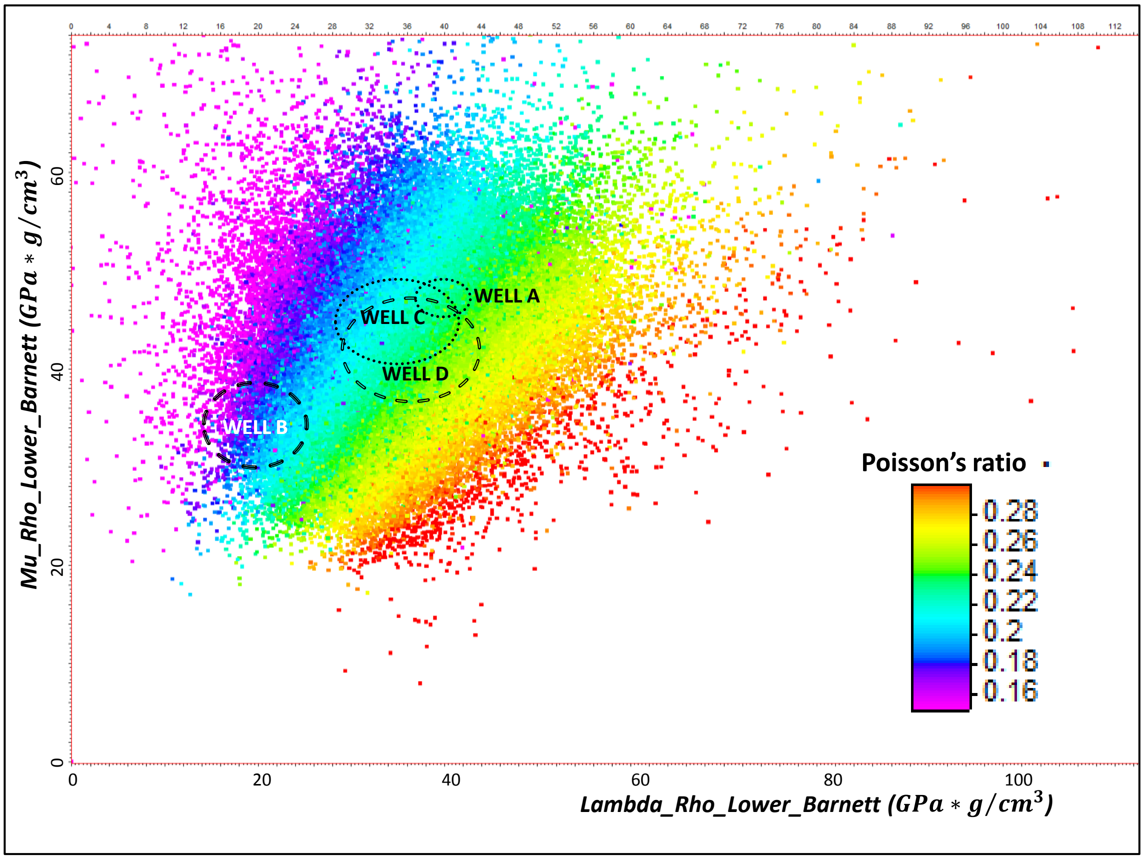

Figure 42. Lambda-rho/mu-rho cross plot for the Lower Barnett Shale. Color indicates the Poisson's ratio. Ovals indicate the range of values observed in the producing zones for each well.

Figures 43, 44, 45, and 46 display the same information shown in Figure 40 but discriminate the points by well. Examining each well individually shows that higher producing zones exhibit lower Poisson's ratios. In other words, the probability of having a more effective completion (hydraulic fracture) increases by placing the well in zones where the rock is more brittle.

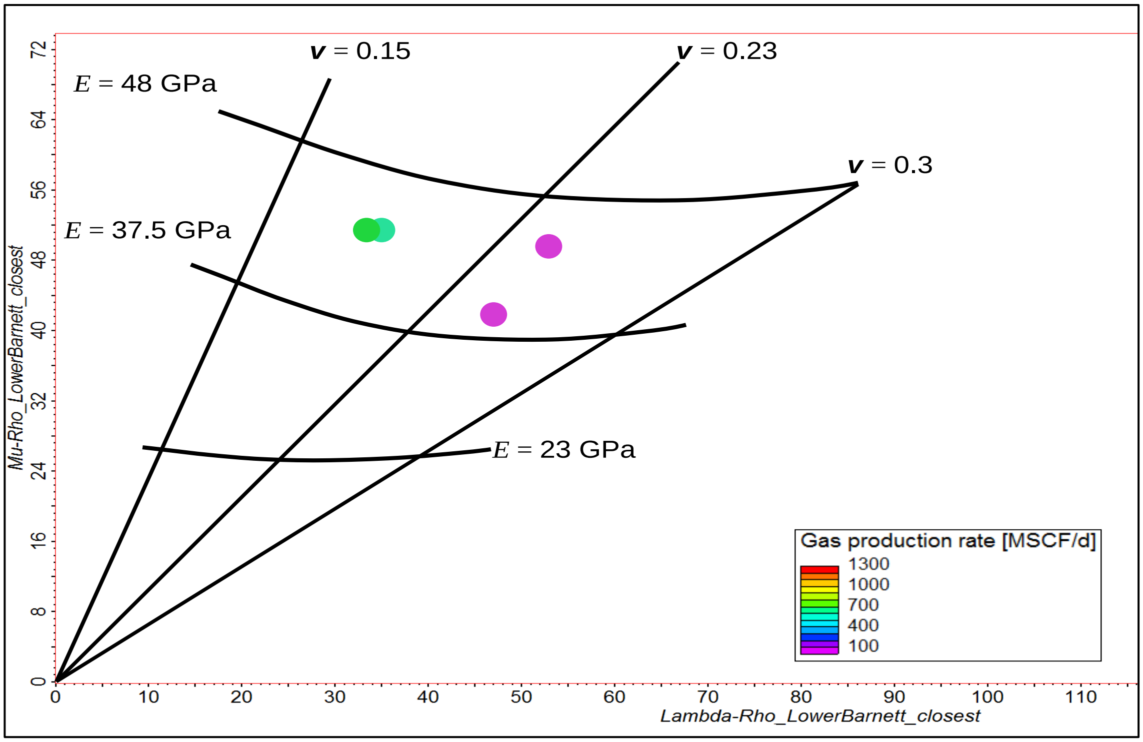

Figure 43. Seismic Lambda-rho/Mu-rho extracted along the wellbores with production logs. The color indicates the gas rate at each individual perforation in WELL A.

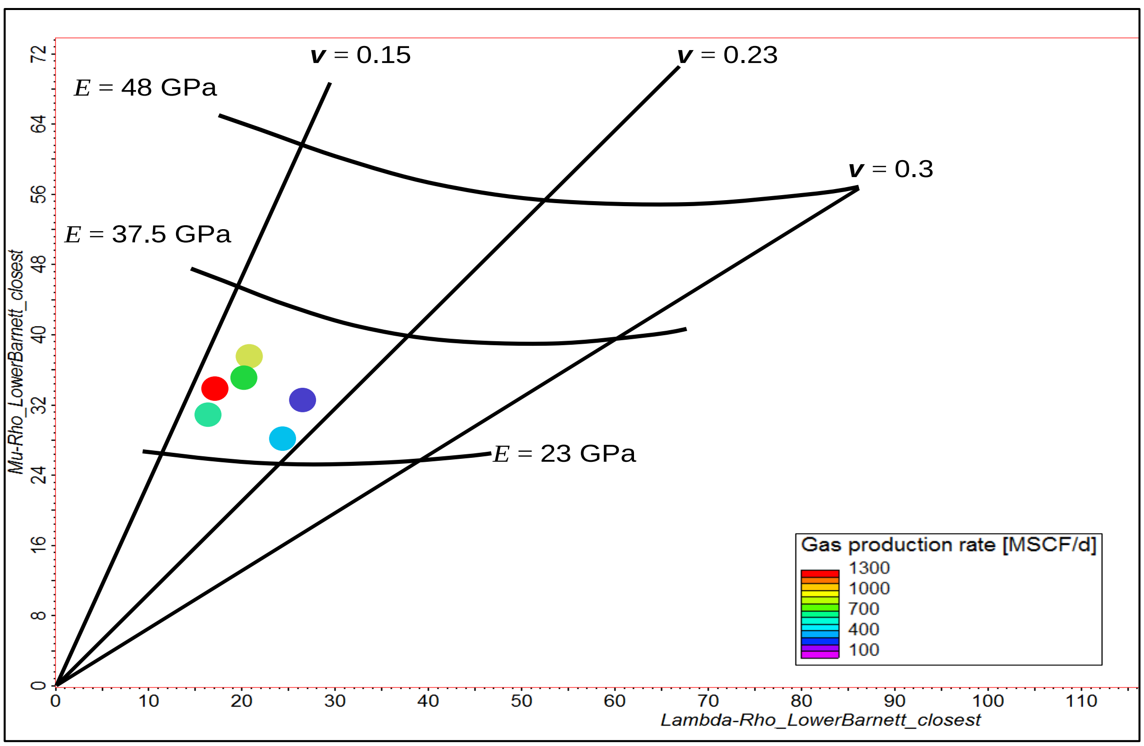

Figure 44. Seismic Lambda-rho/Mu-rho extracted along the wellbores with production logs. The color indicates the gas rate at each individual stage in WELL B.

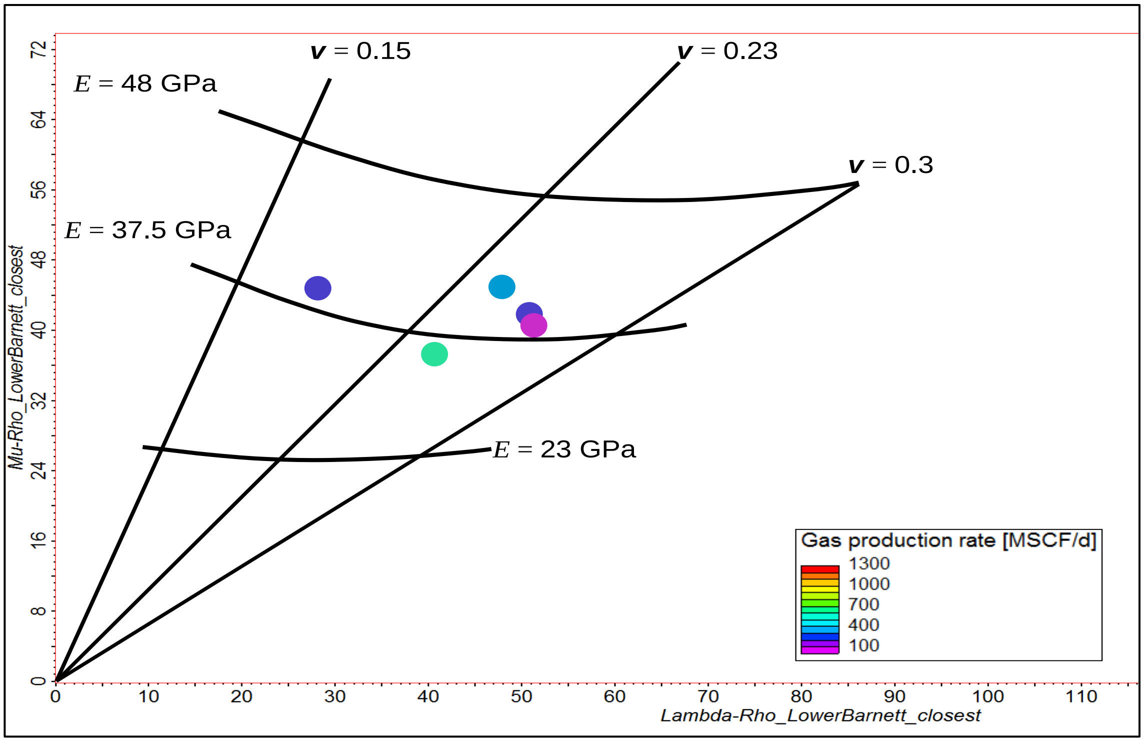

Figure 45. Seismic Lambda-rho/Mu-rho extracted along the wellbores with production logs. The color indicates the gas rate at each individual stage in WELL C.

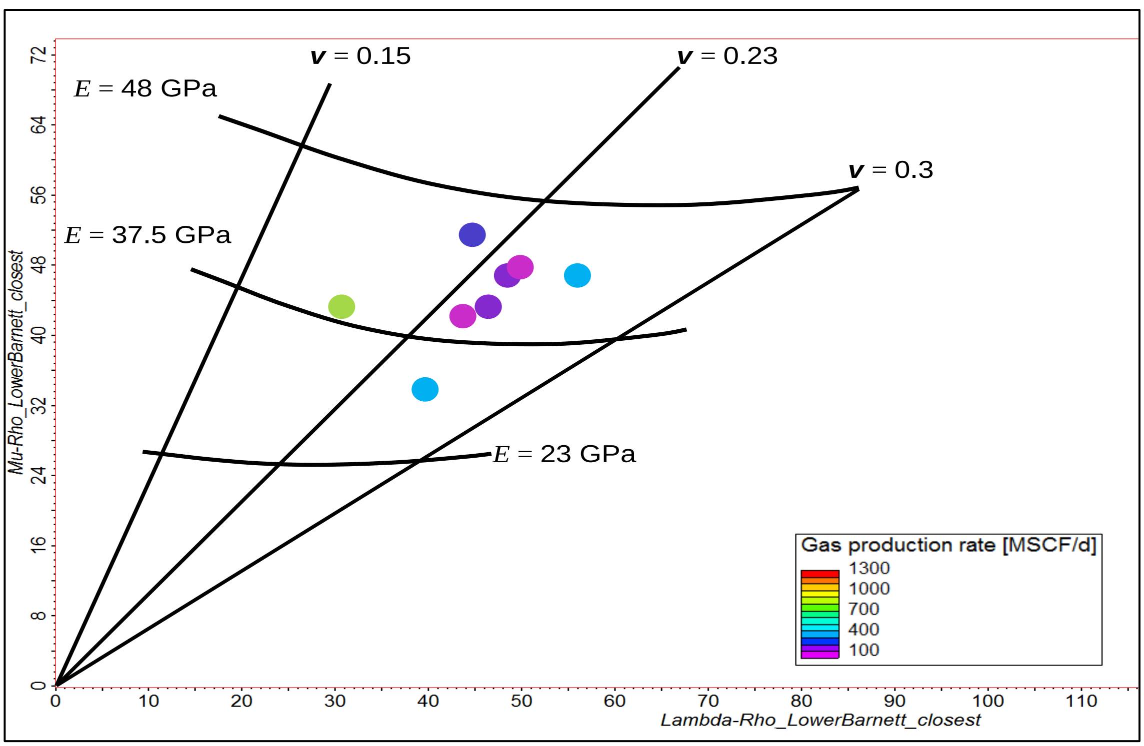

Figure 46. Seismic Lambda-rho/Mu-rho extracted along the wellbores with production logs. The color indicates the gas rate at each individual stage in WELL D.

I used the microseismic data to map the stimulated volume of rock (Figures 13-17) and to confirm that the rock classification is consistent. According to the rock classification, most of WELL A,WELL C, and WELL D are completed in a layer defined as ductile and poor; while WELL B, lays in a brittle and rich layer (Figure 47). Figure 48 shows a stratal slice passing by the depth where most of wells A, C, and D are completed on the top right corner. Figure 49 shows a stratal slice passing by the depth where the whole Well B is completed on the top right corner. Well B is structurally lower than the other three wells. The colors on the maps follow the reservoir quality classification defined in this thesis.

In Figures 50, 51, 52, and 53; I provide more detailed map views of the stratal slices corresponding to the layers where Well A, B, C, and D are completed correspondingly.

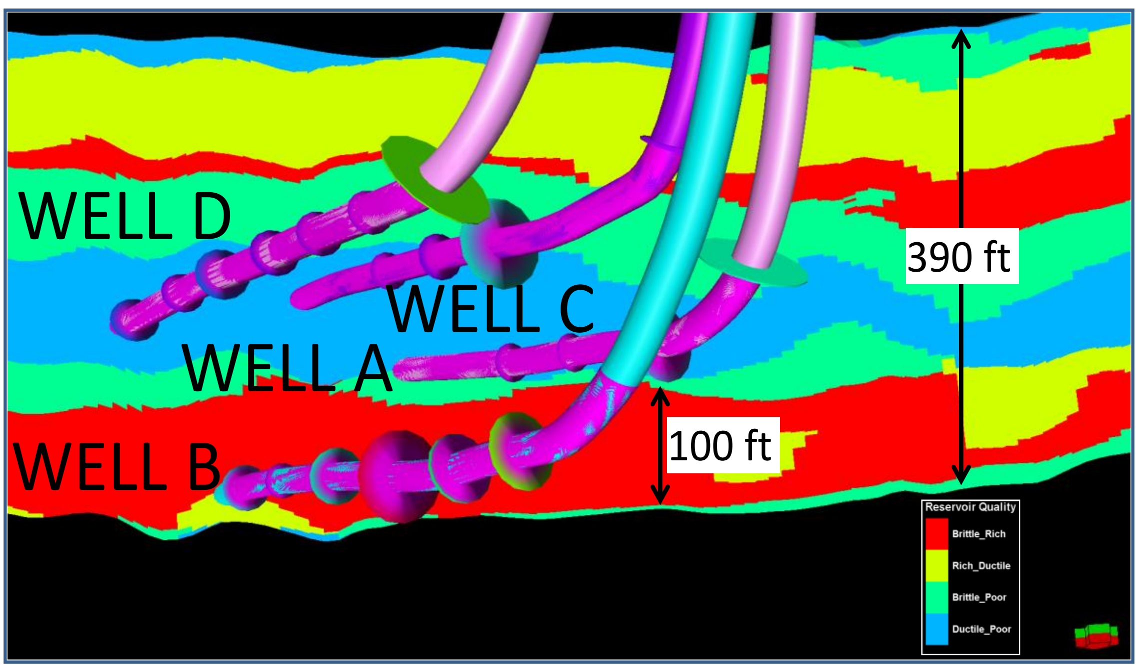

Figure 47. East-west vertical slice through the reservoir quality volume showing the location of the wells having production logs. The color in the layers is following the rock classification proposed. WELL B is entirely completed in a Brittle-Rich (red) layer, while most of WELL A, WELL C, and WELL D rest in a Ductile-Poor (blue) layer.

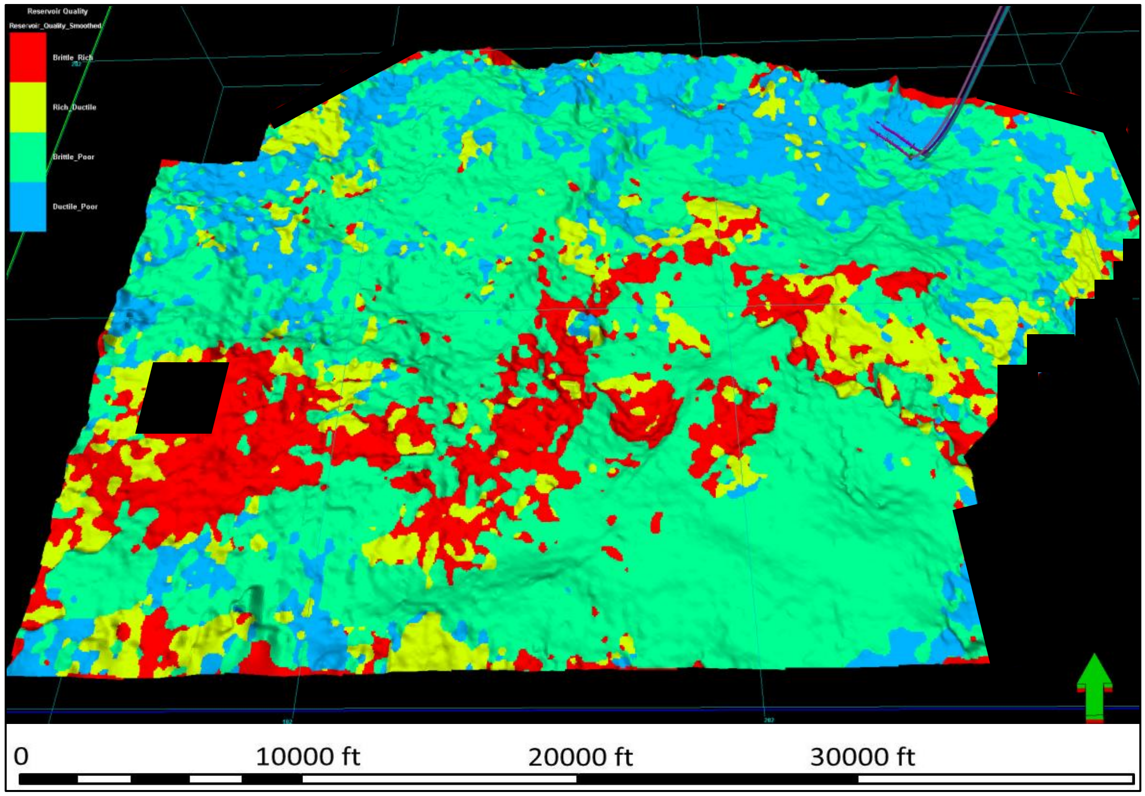

Figure 48. Stratal slice through the reservoir quality volume at the level where most of Well A, C, and D are completed (top right corner). The colors represent the rock quality distribution according to the rock classification proposed. The black square corresponds to a "no permit" zone where seismic data are missing.

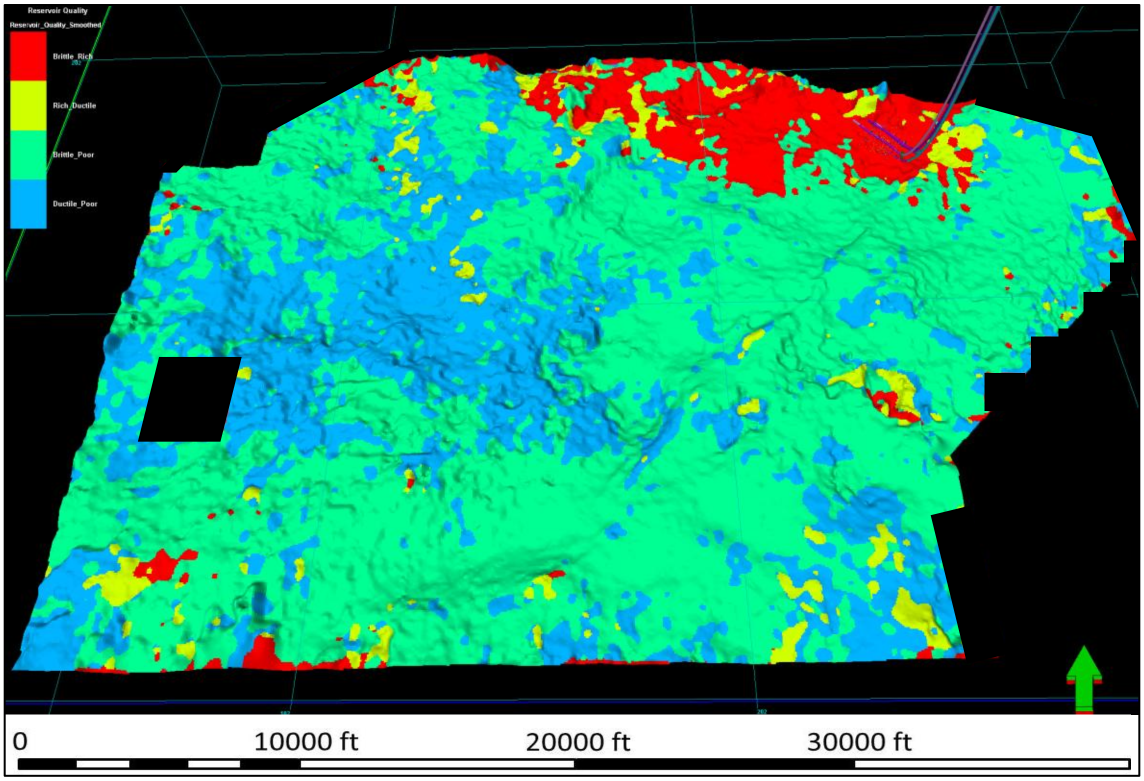

Figure 49. Stratal slice through the reservoir quality volume at the level where most of Well B is completed (top right corner). The colors represent the rock quality distribution according to the rock classification proposed. The black square corresponds to a "no permit" zone where seismic data are missing.

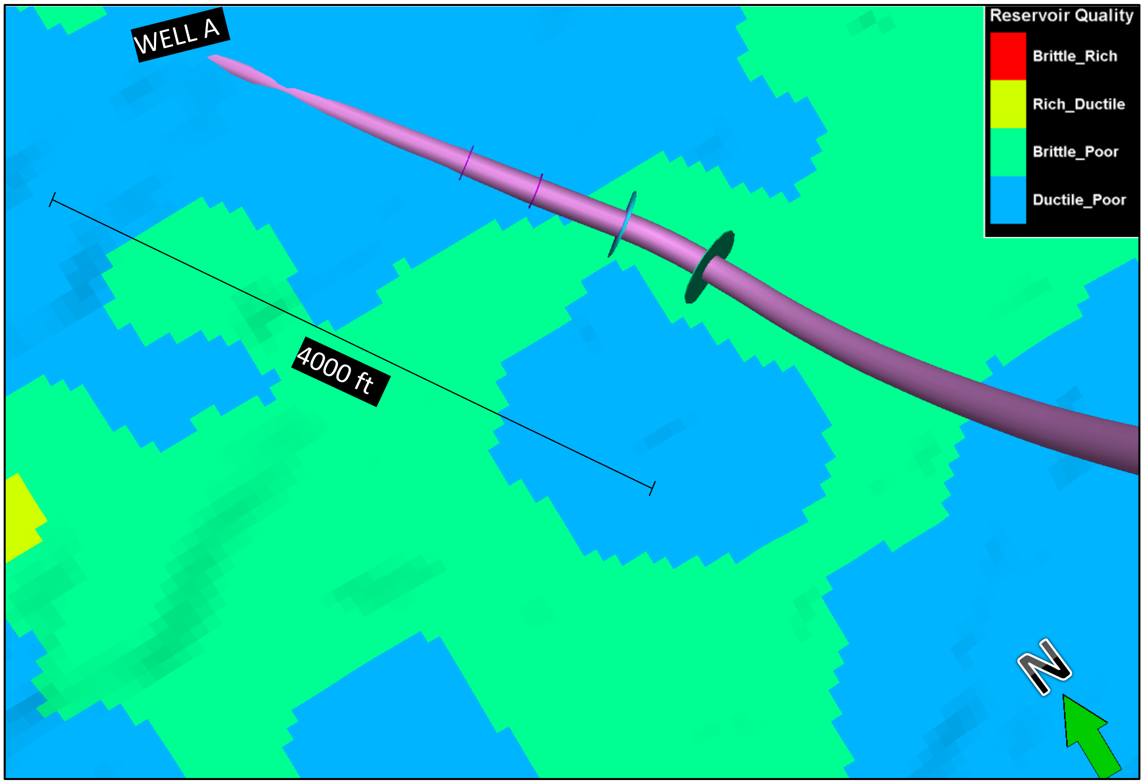

Figure 50. Map view of the stratal slice through the reservoir quality volume at the level where Well A is completed. The colors represent the rock quality distribution according to the rock classification proposed.

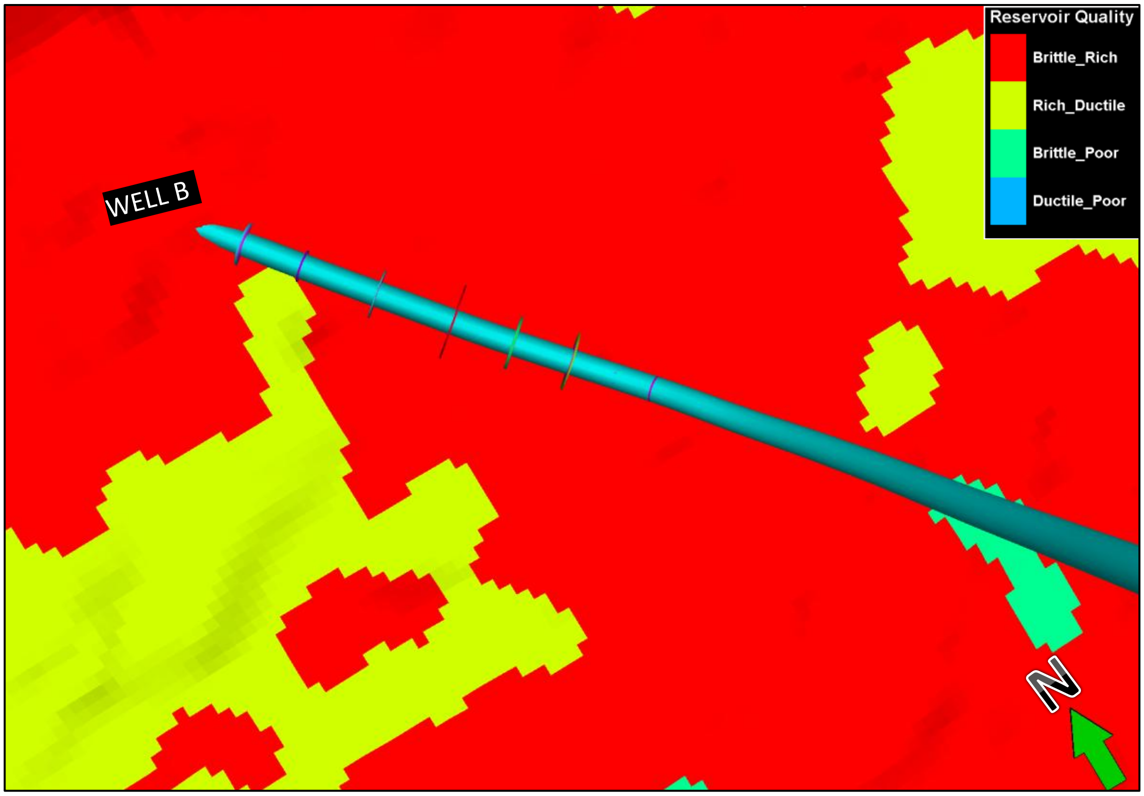

Figure 51. Map view of the stratal slice through the reservoir quality volume at the level where Well B is completed. The colors represent the rock quality distribution according to the rock classification proposed.

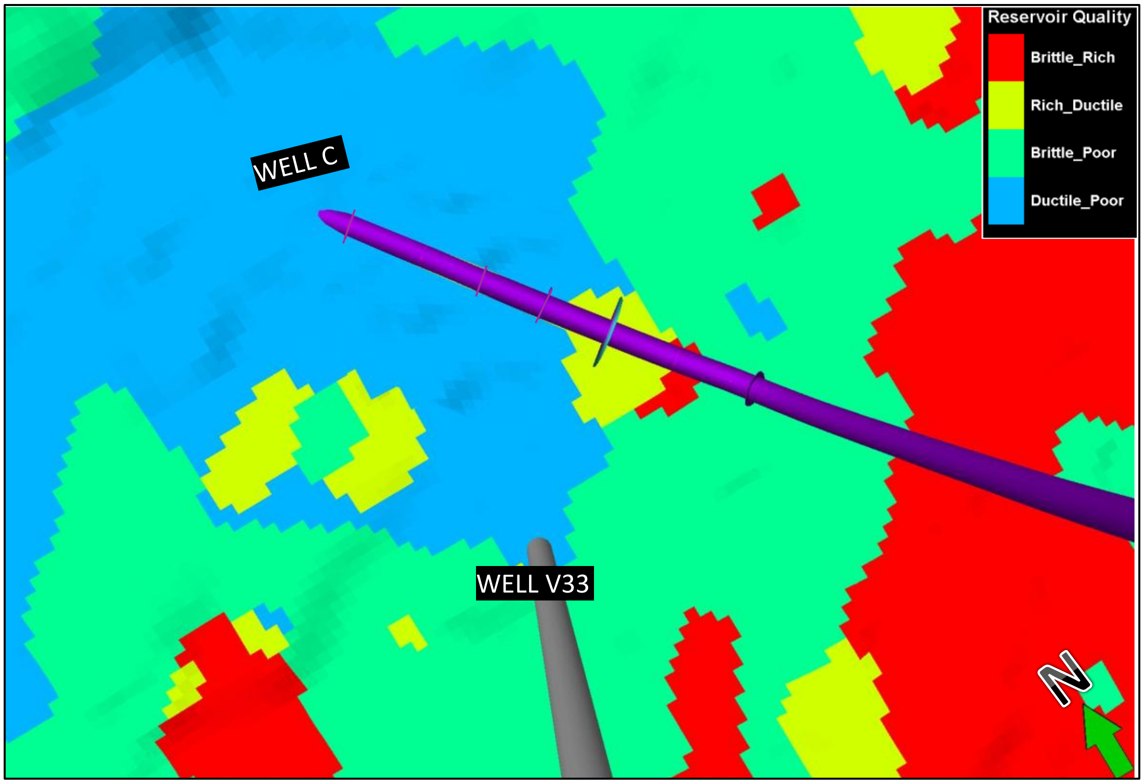

Figure 52. Map view of the stratal slice through the reservoir quality volume at the level where Well C is completed. The colors represent the rock quality distribution according to the rock classification proposed.

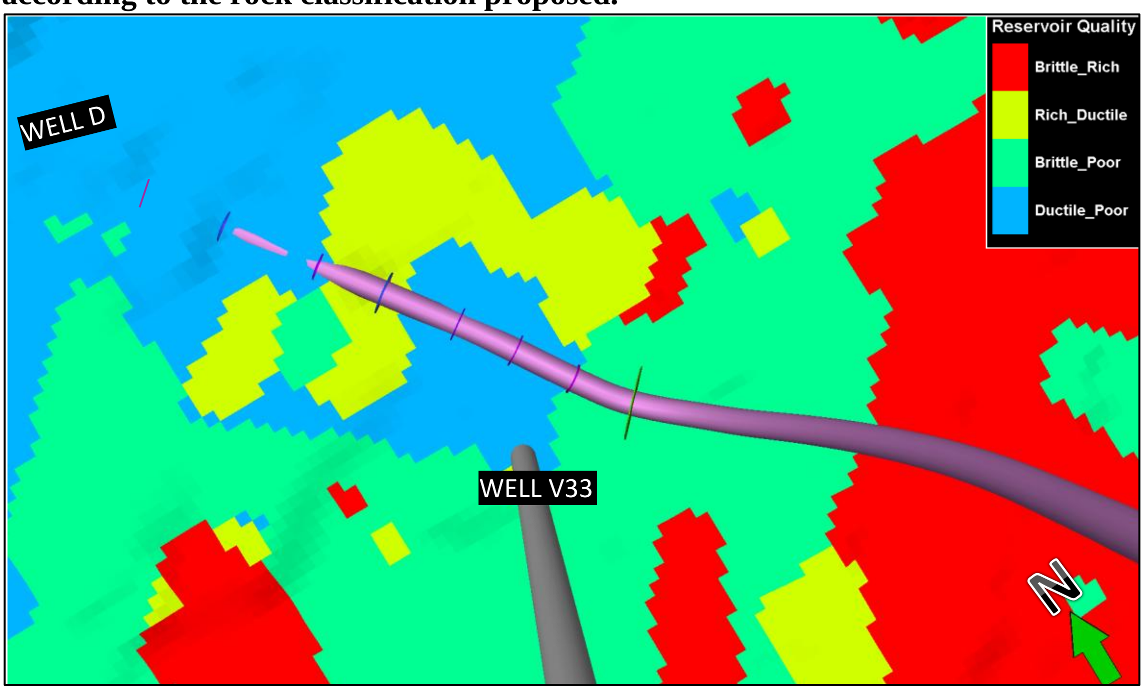

Figure 53. Map view of the stratal slice through the reservoir quality volume at the level where Well D is completed. The colors represent the rock quality distribution according to the rock classification proposed.

Cross-plotting Lambda-rho/Mu-rho values corresponding to microseismic events measured for WELL A (Figure 54), WELL B (Figure 55), WELL C (Figure 56), and WELL D (Figure 57), Note that no matter where the well is completed, the fracture will preferentially grow towards the brittle rock. Around 65 to 70% of the events are recorded in the brittle red and green clusters. The two other horizontal wells in the lower Barnett Shale having microseismic data, Well H18 and Well H3 also show the same trend. Fifty seven percent (57%) and sixty two percent (62%) of the events are recorded in the brittle (red and green) clusters (Figures 58 and 59).

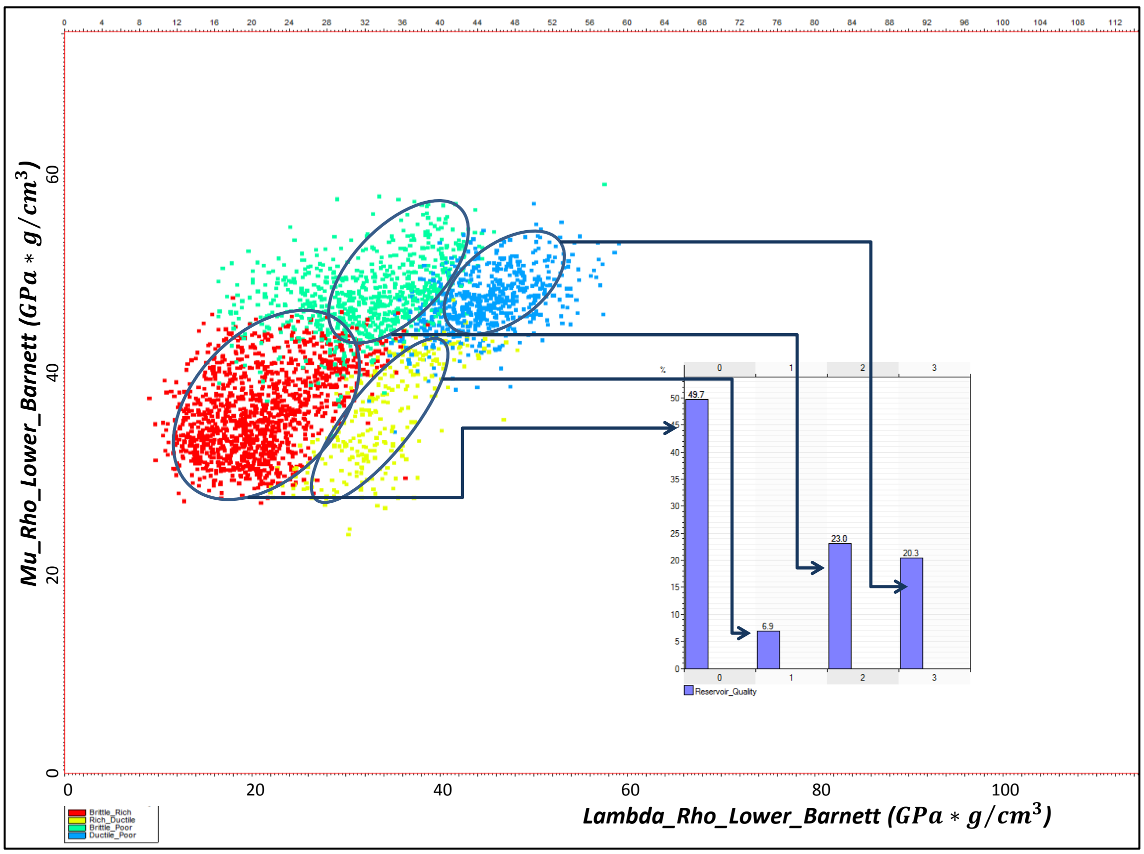

Figure 54. Lambda-rho/Mu-rho cross plots showing the microseismic events recorded while hydraulically fracturing WELL A. About 73% of the microseismic events recorded while stimulating WELL A fall in portions of the rock classified as Brittle according to this reservoir quality classification. Compare to Figure 43 which shows the stages were completed in Brittle-Poor and Ductile-Poor zones.

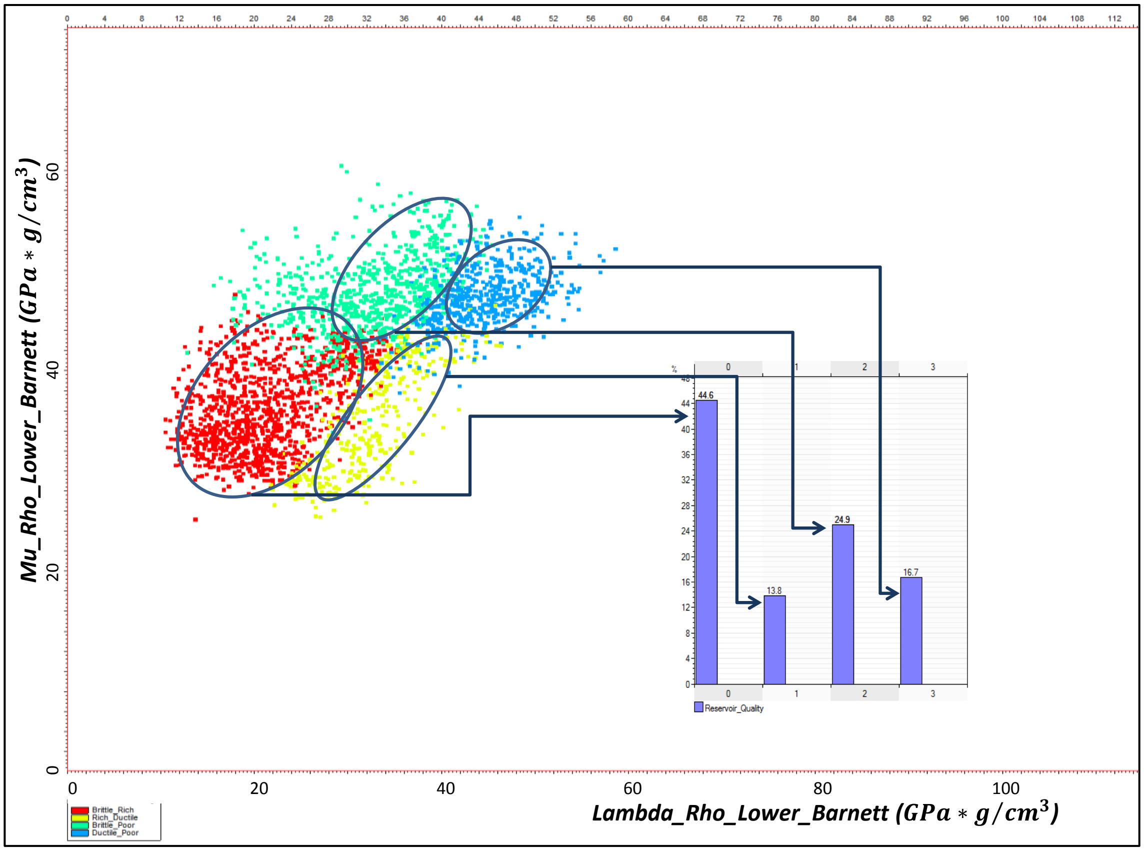

Figure 55. Lambda-rho/Mu-rho cross plots showing the microseismic events recorded while hydraulically fracturing WELL B. About 70% of the MS events recorded while stimulating WELL B fall in portions of the rock classified as Brittle according to this reservoir quality classification. Compare to Figure 44 which shows the stages were completed in Brittle-Rich zones.

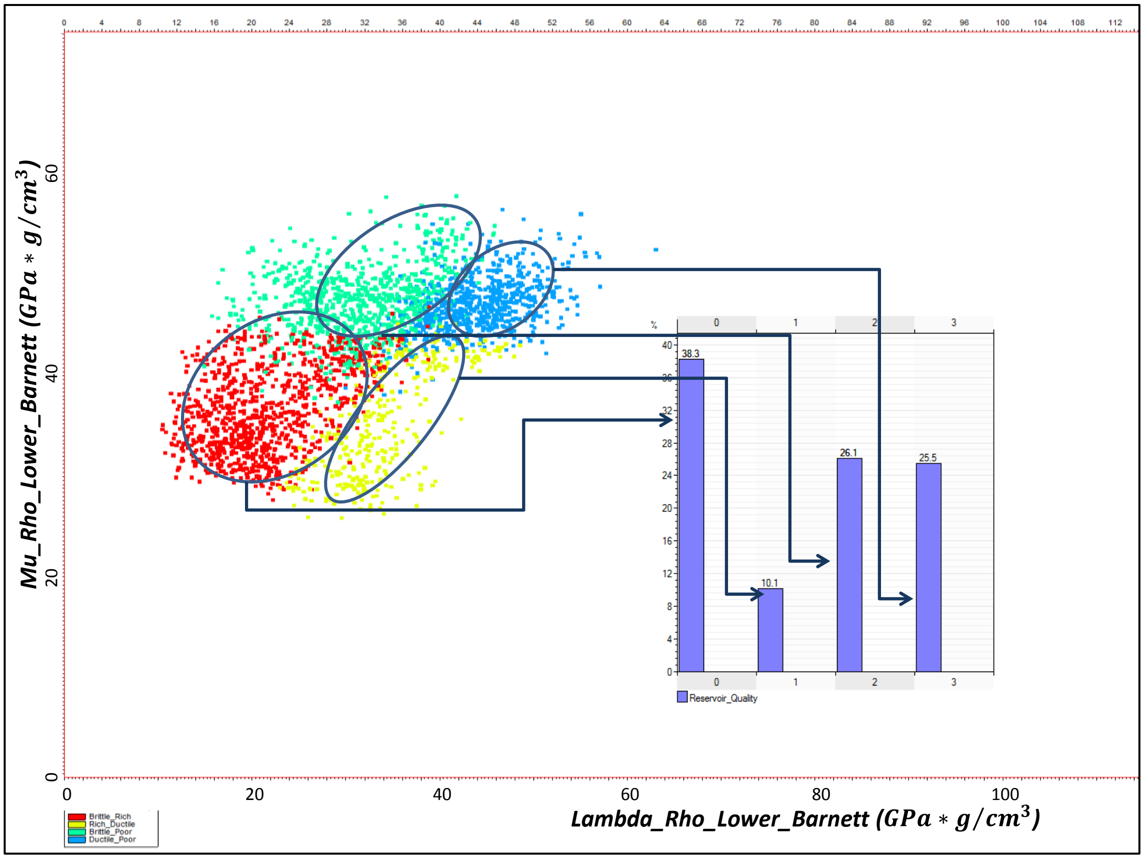

Figure 56. Lambda-rho/Mu-rho cross plots showing the microseismic events recorded while hydraulically fracturing WELL C. About 64% of the MS events recorded while stimulating Well C fall in portions of the rock classified as Brittle according to this reservoir quality classification. Compare to Figure 45 which shows the stages were completed in Brittle-Poor, Ductile-Poor, and Rich-Ductile zones.

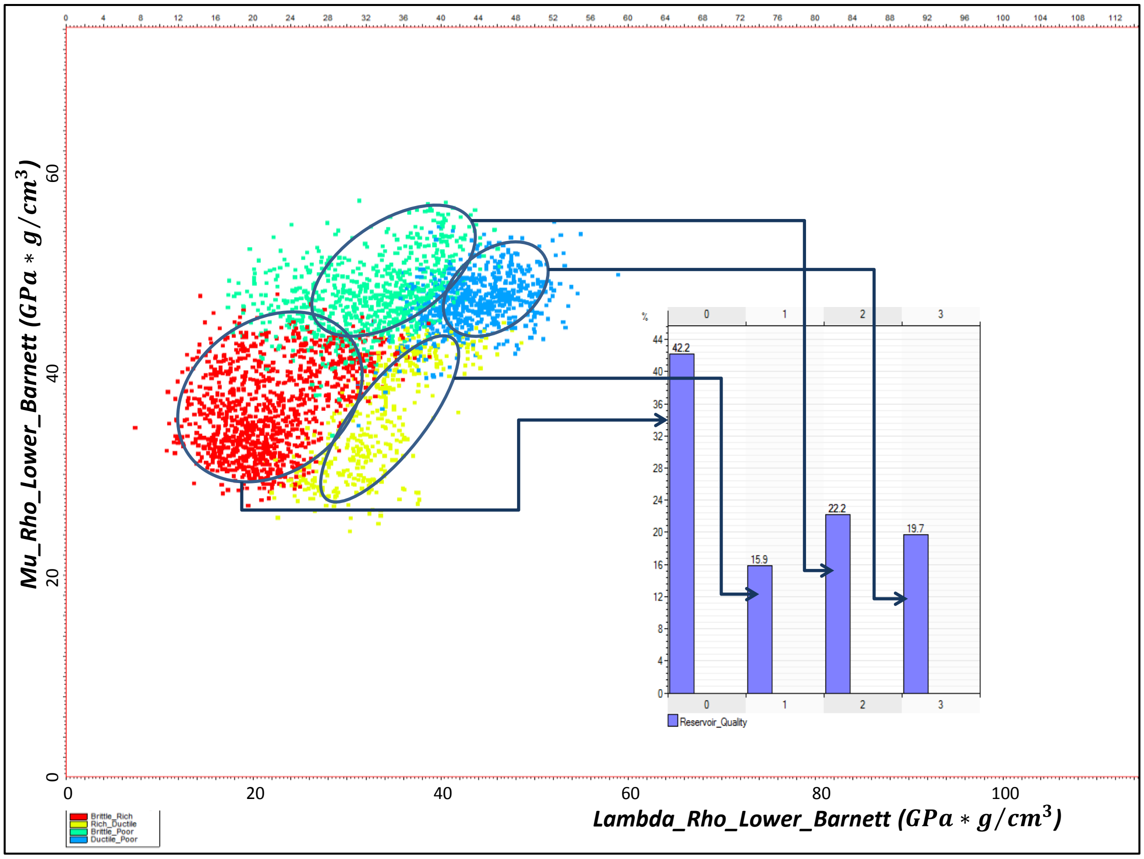

Figure 57. Lambda-rho/Mu-rho cross plots showing the microseismic events recorded while hydraulically fracturing WELL D. About 65% of the microseismic events recorded while stimulating Well D fall in portions of the rock classified as Brittle according to this reservoir quality classification. Compare to Figure 46 which shows the stages were completed in Brittle-Poor, Ductile-Poor, and Rich-Ductile zones.

Although the percentage of microseismic events in the brittle reservoir volumes for each of the four wells is similar, there are significant differences in the gas production between the four wells as seen in Table 5. The total number of events recorded in each of the wells is also similar. These differences may be attributed to the following:

- WELL B is completed in a rich layer while most of WELL A,WELL C, and WELL Dare completed in a poor zone (Figures 47, 48, and 49), but more importantly;

• WELL B is completed in a brittle, fracture prone region, while WELL A, WELL C, and WELL D are completed in a ductile zone (Figures 47, 48, and 49) and therefore in the near wellbore region where the rock is exposed to higher stresses due to production, the rock is likely not competent enough to maintain the hydraulic fractures open to flow. Consequently, my recommendation is that wells be completed in Brittle-Rich rock (red) or Brittle-Poor rock (green) if such layer is underlain/overlain by rock with high gas content or rich rock.

Table 5 records the produced gas rates across each of the individual perforations in WELL A,WELL B,WELL C, and WELL D. Table 5 also shows the total production per well and a well ranking based on these numbers. I also identify the location of the perforation cluster within the reservoir and extract the rock type in the corresponding near wellbore region. These are recorded in Column 5 of Table 5 and shows excellent correlation with the individual fracture stage productivity with around 90% accuracy. One stage in Well B, one stage in Well C, and one stage in Well D do not confirm to this classification. However, in general, the classification correlates with productivity very satisfactorily and Well B, which is by far the most prolific, is entirely completed in a Brittle and Rich zone. Within the other three wells, the perforations completed in zones with good fracability (green) are distinct from the majority of the other stages completed in poor and ductile regions (blue) in terms of productivity.

Table 5. Gas production rate per well and perforation. The colored cells are following the reservoir quality classification proposed.

Well name	***Gas rate per perforation [MSCF/d]***	***Well gas rate [MSCF/d]***	***Rank***	***Reservoir Quality***	***Gas rate per perforation [MSCF/d]***
Well A	650	1260	4	Brittle-Poor	650
	450			Brittle-Poor	450
	80			Ductile-Poor	80
	80			Ductile-Poor	80
Well B	650	4000	1	Brittle-Rich	650
	1250			Brittle-Rich	1250
	700			Brittle-Rich	700
	800			Brittle-Rich	800
	400			Brittle-Rich	400
	200			Brittle-Rich	200
Well C	250	1600	3	Brittle-Poor	250
	650			Rich_Ductile	650
	350			Ductile-Poor	350
	100			Ductile-Poor	100
	250			Ductile-Poor	250
Well D	850	2400	2	Brittle-Poor	850
	100			Ductile-Poor	100
	150			Ductile-Poor	150
	400			Rich_Ductile	400
	250			Brittle-Poor	250
	150			Ductile-Poor	150
	100			Ductile-Poor	100
	400			Ductile-Poor	400

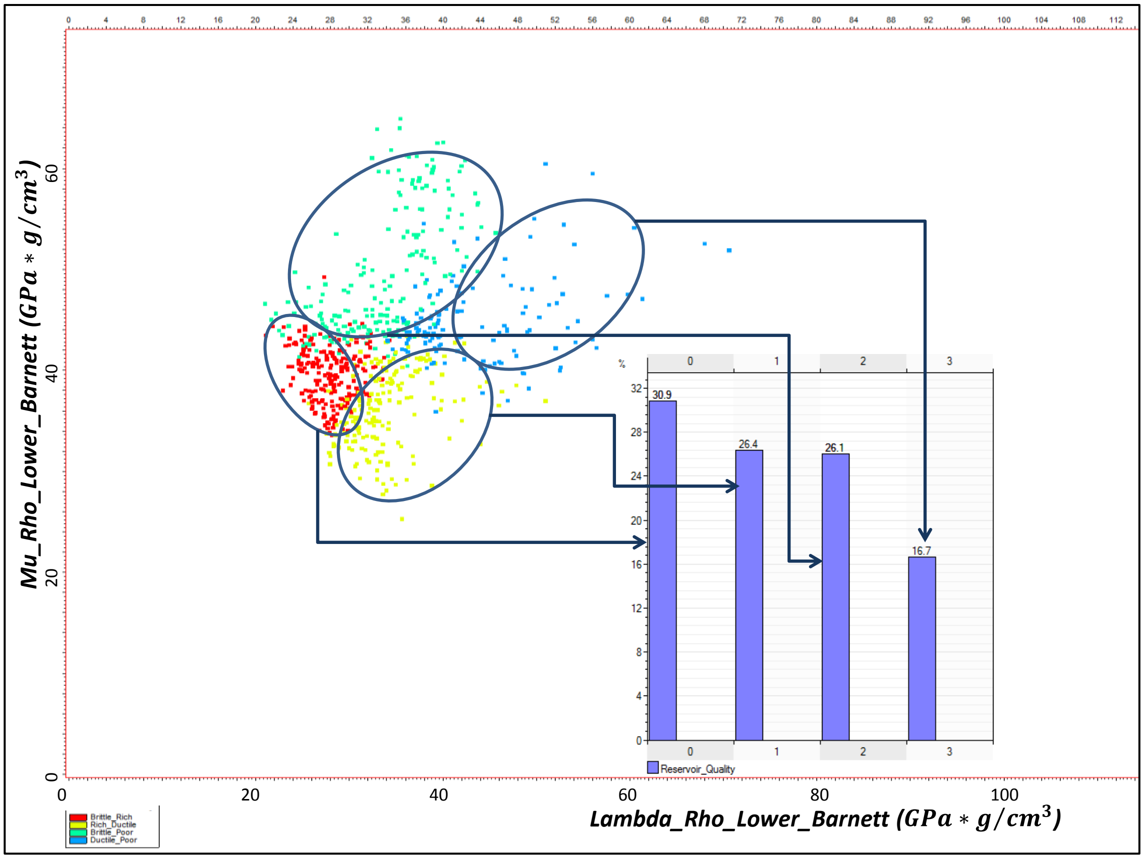

Figure 58. Lambda-rho/Mu-rho cross plots showing the microseismic events recorded while hydraulically fracturing WELL H18. About 57% of the microseismic events recorded while stimulating the well fall in portions of the rock classified as Brittle according to this reservoir quality classification.

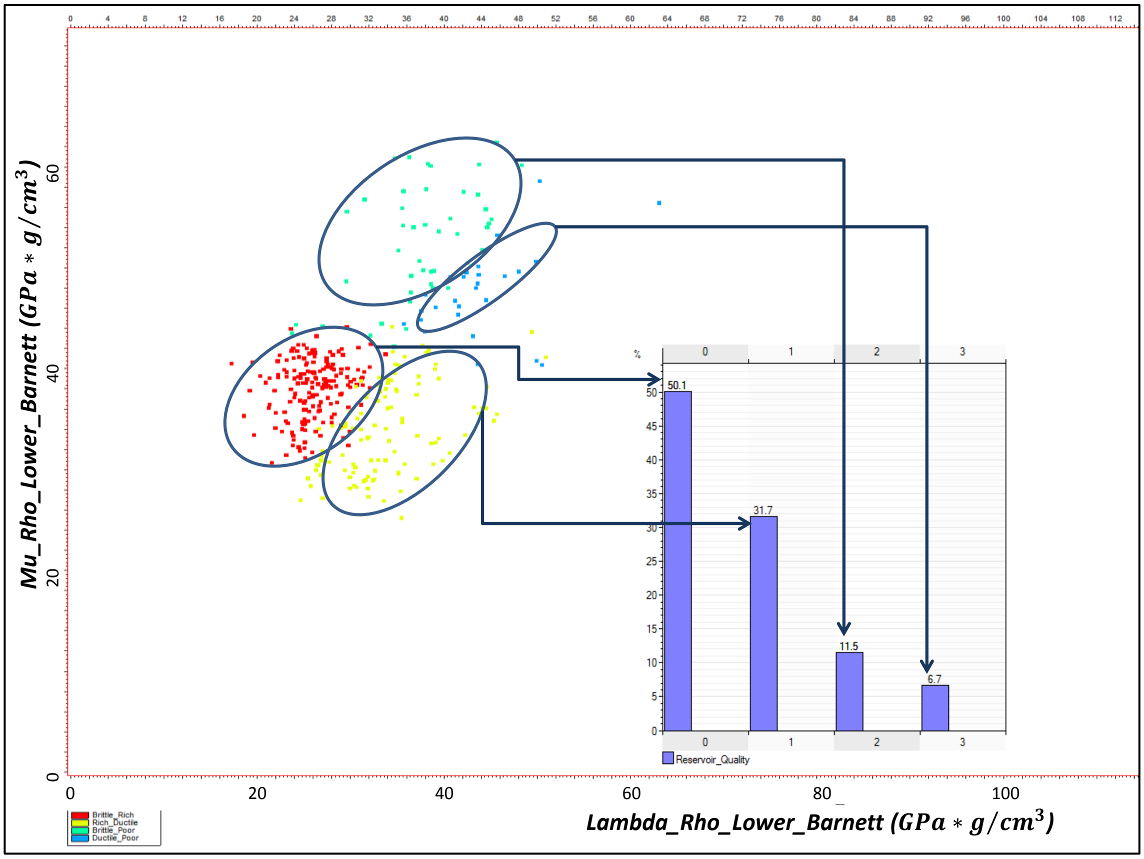

Figure 59. Lambda-rho/Mu-rho cross plots showing the microseismic events recorded while hydraulically fracturing WELL H3. About 62% of the microseismic events recorded while stimulating the well fall in portions of the rock classified as Brittle according to this reservoir quality classification.

Conclusions

The work presented in this thesis shows a unique approach that merges production logs, which enable us to analyze the completion effectiveness variation along the horizontal section of the wellbores, with microseismic and 3D surface seismic data. By using seismically inverted Lambda-rho/Mu-rho cross plots I was able to decouple the completion effectiveness (fracability) effect from the reservoir quality (rock richness) effect.

Iso-Poisson's ratio lines on the Lambda-rho/Mu-rho cross plot can be used as a brittleness discriminator when calibrated with the microseismic events distribution. About 70% of the microseismic events fall in reservoir rock zones having Poisson's ratio values of 0.23 and smaller.

Because of the particular mineralogy and porosity distribution in the Barnett Shale and its relationship to rock properties I found that on the Lambda-rho/Mu-rho cross plot, the Young's modulus helps to distinguish between rich and poor rock.

Gas production rates measured in the production logs and the distribution of the microseismic events corroborate that Lambda-rho/Mu-rho cross plots computed from surface seismic data can predict where the reservoir hydraulic fracturing will be the most effective. The best well is linked to zones that are both brittle and rich.

Fractures will preferentially grow towards the brittle rock no matter where the well is completed. For instance, Well C and Well D are almost fully (more than 90% of the horizontal section) completed in ductile (blue and yellow) rock. However, the majority (65%) of the microseismic events recorded while hydraulically fracturing them appeared in adjacent brittle rocks.

Fractures stages placed in brittle rock perform better than fractures placed in ductile and poor rock. Eleven perforation clusters completed in brittle rock produced an average of 403 MSCF/d of gas each, while ten perforation clusters completed in ductile and poor rock produced an average of 176 MSCF/d of gas each.

Ideally, the horizontal section of the wells should be centered in layers characterized as brittle because in the near wellbore region where the rock is exposed to higher stresses due to production, the rock needs to be competent enough to maintain the hydraulic fractures open to flow. Consequently, my recommendation is that wells be completed in Brittle-Rich rock or Brittle-Poor rock if such layer is underlain/overlain by rock with high gas content or rich rock.

References

Agrawal, A., Wei, Y., and Holditch, S.A. 2012. A Technical and Economic Study of Completion Techniques in Five Emerging US Gas Shales: A Woodford Shale Example. *SPE Drill & Compl* (March 2012): 39-49. SPE 135396. http://dx.doi.org/10.2118/135396-PA

Alzate, J.H., Perez, R., Devegowda, D., and Marfurt, K.J. 2012a. Production Logging Plus 3D Seismic Attributes to Characterize a Shale Play. Oral presentation given at the 2012 SEG Development and Production Forum on Unconventional Resources: Multiscale, Multidisciplinary Integration of Subsurface Data, Banff, Alberta, 15-19 July.

Alzate, J.H., Perez, R., Devegowda, D., and Marfurt, K.J. 2012b. The Value of Production Logging Combined with 3D Surface Seismic in Unconventional Plays Characterization. Submitted to the 82nd SEG Annual International Meeting, Las Vegas, Nevada, 4-9 November.

Arbenz, J.K. 1989. The Ouachita System, in Bally, A.W., and Palmer, A.R., eds., The Geology of North America: an overview, The Geological Society America, p. 371–396.

Baig, A. and Urbancic, T. 2010. Magnitude Determination, Event Detectability, and Assessing the Effectiveness of Microseismic Monitoring Programs in Petroleum Applications. *CSEG Recorder*, (February): 22-26.

Bennett, L., LeCalvez, J., Sarver, D.R., Tanner, K., Birk, W.S., Waters, G., Drew, J., Michaud, G., Primiero, P., Eisner, L., Jones, R., Leslie, D., Williams, M.J., Govenlock, J., Klem, R.C., and Tezuka, K. 2006. The Source for Hydraulic Fracture Characterization, *Oilfield Review*, (Winter 2005/2006): 42-57.

Blakey, R. 2005. Paleogeography and geologic evolution of North America, http://jan.ucc.nau.edu/~rcb7/RCB.html (accessed May 2011)

Boyer, C., Kieschnick, J., Suarez-Rivera, R., Lewis R.E., and Waters, G. 2006.Producing gas from its source, *Oilfield Review*, (Autumn): 36-49

Bruner, Kathy R. and Smosna, R. 2011. A Comparative Study of the Mississippian Barnett Shale, Fort Worth Basin, and Devonian Marcellus Shale, Appalachian Basin. Technical Report DOE/NETL-2011/1478, National Energy Technology Laboratory (NETL) for The United States Department of Energy (April 2011).

Bust, V. K., Majid, A.A., Oletu, J.U., and Worthington, P.F. 2012. The Petrophysics of Shale Gas Reservoirs: Technical Challenges and Pragmatic Solutions. Paper IPTC 14631 presented at the International Petroleum Technology Conference, Bangkok, Thailand, 7-9 February.

Chopra, S. and Marfurt, K.J. ed. 2007. *Seismic Attributes for Prospect Identification and Reservoir Characterization,* 208-210. Tulsa: Society of Exploration Geophysicists.

Cipolla, C., Warpinski, N.R., Mayerhofer, M.J., Lolon, E.P., and Vincent, M.C. 2008. The Relationship Between Fracture Complexity, Reservoir Properties, and Fracture Treatment Design. Paper SPE 115769 presented at the 2008 SPE Annual Technical Conference and Exhibition, Denver, Colorado, 21-24 September.

Cipolla, C., Lewis, R., Maxwell S., and Mack, M. 2011a. Appraising Unconventional Resource Plays: Separating Reservoir Quality from Completion Effectiveness. Paper IPTC 14677 presented at the International Petroleum Technology Conference, Bangkok, Thailand, 7-9 February.

Cipolla, C., Maxwell S., and Downie R. 2011b. A Practical Guide to Interpreting Microseismic Measurements. Paper SPE 144067 presented at the SPE North American Unconventional Gas Conference and Exhibition, The Woodlands, Texas, 14-16 June.

Cipolla, C., Maxwell, S., and Mack, M. 2012. Engineering Guide to the Application of Microseismic Interpretations. Paper SPE 152165 presented at the SPE Hydraulic Fracturing Conference, The Woodlands, Texas, 6-8 February.http://dx.doi.org/10.2118/152165-MS.

Daniels, J., Waters, G., LeCalvez, J., Lassek, J., and Bentley, D. 2007. Contacting More of the Barnett Shale Through an Integration of Real-Time Microseismic Monitoring, Petrophysics and Hydraulic Fracture Design. Paper SPE 110562 presented at the 2007 SPE Annual Technical Conference and Exhibition, Anaheim, California, 12-14 October.

Daugherty, J. and Urbancic, T. 2009. Microseismic Monitoring of a Carbon Sequestration Field Test. In Frontiers + Innovation: Proceedings of the 2009 CSPG CSEG CWLS Convention, Calgary, Alberta.

Dufor, J., Squires, J., Goodway, W. N., Edmunds, A., and Shook, I. 2002. Integrated Geological and Geophysical Interpretation Case Study and Lame Rock Parameter Extractions Using AVO Analysis on the Blacfoot 3C-3D Seismic Data, South Alberta, Canada. *Geophysics,* **67**: 27-37.

Durham, L.S. 2005. Barnett Shale Play Still going Strong. *American Association Petroleum Geologists Bulletin*, **86**: 1,921–1,938.

Elebiju, O.O., Keller, G.R., and Marfurt, K.J. 2010. Investigation of Links Between Precambrian Basement Structure and Paleozoic Strata in the Fort Worth Basin, Texas, U.S.A., Using High-Resolution Aeromagnetic (HRAM) Data and Seismic Attributes. *Geophysics* **75 (4)**: B157-B168.

Energy Information Administration (EIA). 2011. Natural Gas Production. Washington, DC.

Gao, C. 2011. Multiscale Ensemble Kalman Filter for History Matching and Characterization of Barnett Shale. MS Thesis, University of Oklahoma, Norman, Oklahoma (2011).

Goodway, B., Chen, T., and Downton, J. 1997. Improved AVO Fluid Detection and Lithology Discrimination Using Lame Petrophysical Parameters; "λρ', "μρ", & "λ/μ" Fluid Stack, from P and S Inversions: Expanded abstract presented at the 67th SEG Annual International Meeting, Dallas, Texas, 2-7 November.

Goodway, B. 2012. Microseismic: Monitoring Induced Seismicity. Oral presentation given at the Microseismic User Group (MUG), Inaugural meeting, Canadian Society of Exploration Geophysicists. 28 February.

Gunter, G. W., Finneran, J.M., Hartmann, D.J., and Miller, J.D. 1997. Early Determination of Reservoir Flow Units Using an Integrated Petrophysical Method. Paper SPE 38679 presented at the Annual Technical Conference and Exhibition, San Antonio, Texas, 5-8 October.

Guo, Q., Ji, L., Rajabov, V., Friedheim, J., Portella, C., and Wu, R. 2012. Shale Gas Drilling Experience and Lessons Learned from Eagle Ford. Paper SPE 155542 presented at the Americas Unconventional Resources Conference, Pittsburgh, Pennsylvania, 5-7 June. http://dx.doi.org/10.2118/155542-MS.

Gupta, N., Kiv, S., and Devegowda, D. 2012. Identifying Potential Sweet-spots Using Conventional Wireline Logs in the Barnett Shale Play. Submitted to *The Journal of Canadian Petroleum Technology* for peer review.

Gutschick, R.C., and Sandberg, C.A. 1983. Mississippian Continental Margins of the Conterminous United States, in Stanley, D.J., and Moore, G.T., eds., The Shelfbreak Margin—Critical Interface on Continental Margins,: Society of Economic Paleontologists and Mineralogists, Special Publication, 33: 79–96.

Halliburton. 2008. U.S. Shale Gas: An Unconventional Resource, Unconventional Challenges, http://www.halliburton.com/public/solutions/contents/shale/related_docs/H063771 pdf (downloaded 21 February 2012).

Hampson-Rusell^{TM}, version HRS-9 R1.3. 2011. Houston, Texas: CGGVeritas.

Hampson, D.P. and Rusell, T.E. 2005. Simultaneous Inversion of Pre-stack Seismic Data. Expanded abstract presented at the 75th SEG annual meeting, Houston, Texas, 6-11 November.

Hanks, T.C. and Kanamori, H. 1979. A Moment Magnitude Scale. *Journal of Geophysical Research* **84** (B5): 2348-2350.

Hayden, J., and Pursell, D. 2005. The Barnett Shale, Visitors Guide to the Hottest Gas Play in the US: Pickering Energy Partners, Inc., http://www.tudorpickering.com/pdfs/TheBarnettShaleReport.pdf (accessed January 2012).

Hill, D.H. 1990. *Production Logging-Theoretical and Interpretive Elements*, Vol. 14, 145 p. Richardson, Texas: Monograph Series, SPE.

Hoeve, M.V., Meyer, S.C., Preusser, J., and Makowitz, A.2011. Basin-Wide Delineation of Gas Shale "Sweet Spots" Using Density and Neutron Logs; Implications for Qualitative and Quantitative Assessment of Gas Shale Resources. Presented at the AAPG Hedberg Conference, Austin, Texas, 5-10December.

Kale, S. 2009. Petrophysical characterization of Barnett Shale play. MS Thesis, University of Oklahoma, Norman, Oklahoma (2009)

Kale, S., Rai, C.S., and Sondergeld, C.H. 2010a. Petrophysical Characterization of Barnett Shale. Paper SPE 131770 presented at the SPE Unconventional Gas Conference, Pittsburgh, Pennsylvania, 23-25 February.

Kale, S., Rai, C.S., and Sondergeld, C.H. 2010b. Rock Typing in Gas Shales. Paper SPE 134539 presented at the SPE Annual Technical Conference and Exhibition, Florence, Italy, 19-22 September.

Kidney, R.L., Zimmer, U., and Boroundmand, N. 2010. Impact of Distance-Dependent Location Dispersion Error on the Interpretation of Microseismic Event Distributions. *The Leading Edge* (March): 284-289.

Kumar, V., Sondergeld, C.H., and Rai, C.S. 2012. Nano to Macro Mechanical Characterization of Shale. Paper SPE 159808-PP submitted to the SPE Annual Technical Conference and Exhibition, San Antonio, Texas,8-10October.

Lancaster, D.E., McKetta, S., and Lowry, P.H. 1993. Research Findings Help Characterize Fort Worth Basin's Barnett Shale. *Oil & Gas Journal*, **91** (10): 59–64.

Loucks, R.G. and Ruppel, S.C. 2007. Mississippian Barnett Shale: Lithofacies and Depositional Setting of a Deep-water Shale-gas Succession in the Fort Worth Basin, Texas. *American Association Petroleum Geologists Bulletin*, **91** (4): 579–601.DOI:10.1306/11020606059.

Maity, D. and Aminzadeh, F. 2012. Reservoir Characterization of an Unconventional Reservoir by Integrating Microseismic, Seismic, and Well Log Data. Paper SPE 154339 presented at the SPE Western Regional Meeting, Bakersfield, California, 19-23 March.

Matlab®, version 7.12. 2011. Natick, Massachusetts: The Mathworks, Inc.

Mayerhofer, M.J., Lolon, E.P., Warpinski, N.R., Cipolla, C.L., Waiser, D., and Rightmire, C.M. 2010. What Is Stimulated Reservoir Volume*? SPE Prod & Oper* (February 2010): 89-98.

McGillivray, P. 2005. Microseismic and Time-lapse Seismic Monitoring of a Heavy Oil Extraction Process at Peace River, Canada. *CSEG Recorder*, **5** (January): 5-9.

Microsoft® Office, version 14.0.6112.5000. 2010. Redmond, Washington: Microsoft Corporation.

Montgomery, S.L., Jarvie, D.M., Bowker, K.A., and Pollastro, R.M. 2005. Mississippian Barnett Shale, Fort Worth Basin, North-central Texas: Gas-shale play with multi-million cubic foot potential. *American Association Petroleum Geologists Bulletin*, **89**: 155–175.

Noe, J. 2011.Microseismic Frac Mapping: Moving Beyond the Dots from an Engineering Perspective. Oral presentation given at The OGS Shales Moving Forward Workshop, Norman, Oklahoma, 21 July.

Perez, R. 2010. Application of LMR Inversion and Clustering Analysis in the Barnett Shale. SEG Expanded abstract presented at the 80th SEG Annual Meeting, Denver, Colorado, 18-22 October.

Perez, M., Close, D., Goodway, B., and Purdue G. 2011. Developing Templates for Integrating Quantitative Geophysics and Hydraulic Fracture Completions Data: Part I - Principles and Theory. Presented at the 81th SEG Annual International Meeting, San Antonio, Texas, 18-23 September.

Petrel®, version 2011.2.3. 2011. Houston, Texas: Schlumberger Limited.

Pollastro, R.M., Hill, R.J., Jarvie, D.M., and Henry, M.E. 2003. Assessing Undiscovered Resources of the Barnett-Paleozoic Total Petroleum System, Bend Arch-Fort Worth Basing Province, Texas. Online adaptation of presentation at AAPG Southwest Section Meeting, Fort Worth, Texas, 1-4 March.

Pollastro, R.M. 2007. Total Petroleum System Assessment of Undiscovered Resources in the Giant Barnett Shale Continuous (Unconventional) Gas Accumulation, Fort Worth Basin, Texas. *American Association Petroleum Geologists Bulletin*, **91** (4): 551–578.

Ramakrishnan, H., Yuyan, R., and Belhadi, J. 2011. Real-Time Completion Optimization of Multiple Laterals in Gas Shale Reservoirs: Integration of Geology, Log, Surface Seismic, and Microseismic Information. Paper SPE 140542 presented at the SPE Hydraulic Fracturing Technology Conference and Exhibition, The Woodland, Texas, 24-25 January.

Refunjol, X. E. 2010. Hydraulically-Induced Microseismic Fracture Characterization From Surface Seismic Attributes and Seismic Inversion: A North Texas Barnett Shale Case Study. MS thesis, The University of Oklahoma, Norman, Oklahoma.

Refunjol, X.E., Keranen, K.M., LeCalvez, J.H., and Marfurt, K.J. 2012. Integration of Hydraulically Induced Microseismic Events Location with Active Seismic Attributes: A North Texas Barnett Shale Case Study. *Geophysics*, **77** (3): KS1-KS12.

Review of Emerging Resources: U.S. Shale Gas and Shale Oil Plays. Report prepared for Office of Energy Analysis, Energy Information Administration, and U.S. Department of Energy, INTEK, Inc., Washington D.C., USA (July 2011).

Schenk, C.J. and Pollastro, R.M. 2002. Natural Gas Production in the United States: National Assessment of Oil and Gas Series. USGS Fact Sheet FS-113-01, Denver, Colorado, January.

Shemeta, J. and Anderson, P. 2010. It’s a Matter of Size: Magnitude and Moment Estimates for Microseismic Data. *The Leading Edge* (March): 296-302.

Singh, P. 2008. Lithofacies and Sequence Stratigraphic framework of the Barnett Shale, Northeast Texas. PhD dissertation, The University of Oklahoma, Norman, Oklahoma (2008).

Sondergeld, C.H., Newshan, K.E., Comisky, J. ., Rice, M.C., and Rai, C.S. 2010. Petrophysical Considerations in Evaluating and Producing Shale Gas Resources. Paper SPE 131768 presented at the SPE Unconventional Gas Conference, Pittsburgh, Pennsylvania, 23-25 February.

Sullivan, E.C., Marfurt, K.J., Lacazette, A., and Ammerman, M. 2006. Application of New Seismic Attributes to Collapse Chimneys in the Fort Worth Basin. *Geophysics* **71** (4): B11-B119.

Takahashi, T. and Tanaka, S. 2010. Rock Physics Model for Interpreting Dynamic and Static Young’s Moduli of Soft Sedimentary Rocks. Paper IRSM presented at the IRSM International Symposium 2010 and 6th Asian Mechanics Symposium on Advances in Rock Engineering, New Delhi, India, 23-27 October.

Thompson A.M. 2010. Induced Fracture Detection in the Barnett Shale, FT. Worth Basin, Texas. MS thesis, The University of Oklahoma, Norman, Oklahoma.

Walker, J.D. and Geissman, J.W. 2009. Geologic Time Scale: The Geological Society of America, doi: 10.1130/2009.CTS004R2C.

Warpinski, N. 2009. Microseismic Monitoring: Inside and Out. *J. Pet Tech* (November): 80-85. SPE-118537.

Waters, G., Ramakrishnan, H., Daniels, J., Bently, D., Belhadi, J., and Sparkman, D. 2009. Utilization of Real Time Microseismic Monitoring and Hydraulic Fracture Diversion Technology in the Completion of Barnett Shale Horizontal Wells. Paper OTC 20268 presented at the 2009 Offshore Technology Conference, Houston, Texas, 4-7 May.

Yu, G., and Aguilera, R. 2012. 3D Analytical Modeling of hydraulic Fracturing Stimulated Reservoir Volume. Paper SPE 153486 presented at the SPE Latin American and Caribbean Petroleum Engineering Conference, Mexico City, Mexico, 16-18 April.

Zimmer, U. 2011. Calculating Stimulated Reservoir Volume (SRV) with Consideration of Uncertainties in Microseismic-Event Locations. Paper CSUG/SPE 145610 presented at the Canadian Unconventional Resources Conference, Calgary, Alberta, 15-17 November.

Appendix A: MATLAB Code

Appendix A1: Reading the Data

This subroutine, saved under the name “importfile2.m”, opens the file “MS_Nine_Wells_Matlab_Corrected.xlsb” which contains all the microseismic raw data, reads all the information contained in it, and assigns array variable to each of the columns in the file. The following code can be run in MATLAB® 7.12.

```
function importfile2(~)
%IMPORTFILE1(FILETOREAD1)
%  Imports data from the specified file
%  FILETOREAD1:  file to read

%  Auto-generated by MATLAB on 03-Mar-2012 17:01:51

% Import the file
fileToRead1='MS_Nine_Wells_Matlab_Corrected.xlsb';
sheetName='Nine_Wells_MSLocations';
[numbers, strings, raw] = xlsread(fileToRead1, sheetName);
if ~isempty(numbers)
   newData1.data =  numbers;
end

if ~isempty(strings) && ~isempty(numbers)
   [strRows, strCols] = size(strings);
   [numRows, numCols] = size(numbers);
   likelyRow = size(raw,1) - numRows;
% Break the data up into a new structure with one field per column.
if strCols == numCols && likelyRow > 0 && strRows >= likelyRow
      newData1.colheaders = strings(likelyRow, :);
end
end

% Create new variables in the base workspace from those fields.
for i = 1:size(newData1.colheaders, 2)
   assignin('base', genvarname(newData1.colheaders{i}), newData1.data(:,i));
end
```

Appendix A2: Filtering the Data

This subroutine, saved under the name "createfigure2_viewing_limit.m", does basically three global operations on the microseismic raw data. Firstly, it searches and discards all the microseismic events that do not have the magnitude reading. Then, it computes the distance between the microseismic event and the monitoring array; and finally, it removes all the microseismic points whose magnitudes are below the viewing limit determined independently for each stimulated well. Within the code, the three operations are named as:

- "NaN" Cleaning
- Distance calculation and partitioning the data.
- Removing data below the viewing limit

The following code can be run in MATLAB® 7.12. This code also generates two plots of distance versus magnitude for each well independently; one before and one after the data are filtered.

"NaN" Cleaning

This part of the code is in charge of deleting any entry in the data that does not have a magnitude reading. It is, only the points having all the relevant information such as Moment Magnitude, Moment log and Coordinates are preserved. The rest is cleared.

```
x = EventXCoordinate0x28ft0x29;
y = EventYCoordinate0x28ft0x29;
z = EventTVDSubsea0x28ft0x29;
EventDate=EventDate+datenum('30-Dec-1899');
ABA=find(isnan(magnitude0x28Euc0x29(:,1)));
EUC=zeros(size(magnitude0x28Euc0x29,1)-size(ABA,1),1);
x=zeros(size(magnitude0x28Euc0x29,1)-size(ABA,1),1);
y=zeros(size(magnitude0x28Euc0x29,1)-size(ABA,1),1);
z=zeros(size(magnitude0x28Euc0x29,1)-size(ABA,1),1);
AZI=zeros(size(magnitude0x28Euc0x29,1)-size(ABA,1),1);
Date=zeros(size(magnitude0x28Euc0x29,1)-size(ABA,1),1);
Time=zeros(size(magnitude0x28Euc0x29,1)-size(ABA,1),1);
Density=zeros(size(magnitude0x28Euc0x29,1)-size(ABA,1),1);
```

```
MaxAZI=zeros(size(magnitude0x28Euc0x29,1)-size(ABA,1),1);
minAZI=zeros(size(magnitude0x28Euc0x29,1)-size(ABA,1),1);
MaxINC=zeros(size(magnitude0x28Euc0x29,1)-size(ABA,1),1);
minINC=zeros(size(magnitude0x28Euc0x29,1)-size(ABA,1),1);
MD=zeros(size(magnitude0x28Euc0x29,1)-size(ABA,1),1);
Moment=zeros(size(magnitude0x28Euc0x29,1)-size(ABA,1),1);
Angle=zeros(size(magnitude0x28Euc0x29,1)-size(ABA,1),1);
Reliability=zeros(size(magnitude0x28Euc0x29,1)-size(ABA,1),1);
Distance=zeros(size(magnitude0x28Euc0x29,1)-size(ABA,1),1);
VertDis=zeros(size(magnitude0x28Euc0x29,1)-size(ABA,1),1);
WellC=zeros(size(magnitude0x28Euc0x29,1)-size(ABA,1),1);
StageC=zeros(size(magnitude0x28Euc0x29,1)-size(ABA,1),1);
counter=1;
counter2=1;
for che=1:size(magnitude0x28Euc0x29,1)
if counter2<=size(ABA,1)
if che==ABA(counter2,1)
        counter2=counter2+1;
else
        EUC(counter,1)=magnitude0x28Euc0x29(che,1);
        x(counter,1)=EventXCoordinate0x28ft0x29(che,1);
        y(counter,1)=EventYCoordinate0x28ft0x29(che,1);
        z(counter,1)=EventTVDSubsea0x28ft0x29(che,1);
        AZI(counter,1)=Azimuth0x28dega0x29(che,1);
        Date(counter,1)=EventDate(che,1);
        Time(counter,1)=EventTime(che,1);
        Density(counter,1)=EventDensity(che,1);
        MaxAZI(counter,1)=MaxStressAzimuth0x28dega0x29(che,1);
        minAZI(counter,1)=MinStressAzimuth0x28dega0x29(che,1);
        MaxINC(counter,1)=MaxStressInclination0x28dega0x29(che,1);
        minINC(counter,1)=MinStressInclination0x28dega0x29(che,1);
        MD(counter,1)=MeasuredDepth0x28ft0x29(che,1);
        Moment(counter,1)=MomentLog0x28J0x29(che,1);
        Angle(counter,1)=PolarAngle0x28dega0x29(che,1);
        Reliability(counter,1)=Reliability0x28Euc0x29(che,1);
        VertDis(counter,1)=VerticalDist0x28ft0x29(che,1);
        WellC(counter,1)=Well(che,1);
        StageC(counter,1)=Stage(che,1);
        counter=counter+1;
end
else
   EUC(counter,1)=magnitude0x28Euc0x29(che,1);
   x(counter,1)=EventXCoordinate0x28ft0x29(che,1);
   y(counter,1)=EventYCoordinate0x28ft0x29(che,1);
   z(counter,1)=EventTVDSubsea0x28ft0x29(che,1);
   AZI(counter,1)=Azimuth0x28dega0x29(che,1);
   Date(counter,1)=EventDate(che,1);
   Time(counter,1)=EventTime(che,1);
   Density(counter,1)=EventDensity(che,1);
   MaxAZI(counter,1)=MaxStressAzimuth0x28dega0x29(che,1);
   minAZI(counter,1)=MinStressAzimuth0x28dega0x29(che,1);
   MaxINC(counter,1)=MaxStressInclination0x28dega0x29(che,1);
   minINC(counter,1)=MinStressInclination0x28dega0x29(che,1);
   MD(counter,1)=MeasuredDepth0x28ft0x29(che,1);
   Moment(counter,1)=MomentLog0x28J0x29(che,1);
   Angle(counter,1)=PolarAngle0x28dega0x29(che,1);
```

```
    Reliability(counter,1)=Reliability0x28Euc0x29(che,1);
    VertDis(counter,1)=VerticalDist0x28ft0x29(che,1);
    WellC(counter,1)=Well(che,1);
    StageC(counter,1)=Stage(che,1);
    counter=counter+1;
end
%che = che+1;

end
```

Distance calculation and partitioning the data.

This part of the program computes the distance of each event recorded with respect to the observation well. At the same time it partitions the data. The objective of sectioning the data is to be able to create a scatter plot for each well independently.

```
zo=6700;
counter3=1;
counter10=1;
counter15=1;
counter18=1;
counter30=1;
counter115=1;
counter116=1;
counter121=1;
counter126=1;
counter258=1;
counter259=1;
for che=1:(size(magnitude0x28Euc0x29,1)-size(ABA,1))
switch WellC(che)
case 3
        xo=2035793.67;
yo=538201.74;
        Distance(che,1)=((x(che,1)-xo)^2+(y(che,1)-yo)^2+(z(che,1)-zo)^2)^.5;
EUC3(counter3)=EUC(che);
        Dist3(counter3)=Distance(che);
        Stage3(counter3)=StageC(che);
        x3(counter3,1)=x(che,1);
        y3(counter3,1)=y(che,1);
        z3(counter3,1)=z(che,1);
        AZI3(counter3,1)=AZI(che,1);
        Date3(counter3,1)=Date(che,1);
        Time3(counter3,1)=Time(che,1);
        Density3(counter3,1)=Density(che,1);
        MaxAZI3(counter3,1)=MaxAZI(che,1);
        minAZI3(counter3,1)=minAZI(che,1);
        MaxINC3(counter3,1)=MaxINC(che,1);
        minINC3(counter3,1)=minINC(che,1);
        MD3(counter3,1)=MD(che,1);
        Moment3(counter3,1)=Moment(che,1);
        Angle3(counter3,1)=Angle(che,1);
```

```
        Reliability3(counter3,1)=Reliability(che,1);
        VertDis3(counter3,1)=VertDis(che,1);
        counter3=counter3+1;
case 10
        xo=2021138.98;
        yo=533221.83;
Distance(che,1)=((x(che,1)-xo)^2+(y(che,1)-yo)^2+(z(che,1)-zo)^2)^.5;
EUC10(counter10)=EUC(che);
        Dist10(counter10)=Distance(che);
        Stage10(counter10)=StageC(che);
        x10(counter10,1)=x(che,1);
        y10(counter10,1)=y(che,1);
        z10(counter10,1)=z(che,1);
        AZI10(counter10,1)=AZI(che,1);
        Date10(counter10,1)=Date(che,1);
        Time10(counter10,1)=Time(che,1);
        Density10(counter10,1)=Density(che,1);
        MaxAZI10(counter10,1)=MaxAZI(che,1);
        minAZI10(counter10,1)=minAZI(che,1);
        MaxINC10(counter10,1)=MaxINC(che,1);
        minINC10(counter10,1)=minINC(che,1);
        MD10(counter10,1)=MD(che,1);
        Moment10(counter10,1)=Moment(che,1);
        Angle10(counter10,1)=Angle(che,1);
        Reliability10(counter10,1)=Reliability(che,1);
        VertDis10(counter10,1)=VertDis(che,1);
        counter10=counter10+1;
case 15
        xo=2037369.67;
        yo=529578.64;
Distance(che,1)=((x(che,1)-xo)^2+(y(che,1)-yo)^2+(z(che,1)-zo)^2)^.5;
EUC15(counter15)=EUC(che);
        Dist15(counter15)=Distance(che);
        Stage15(counter15)=StageC(che);
        x15(counter15,1)=x(che,1);
        y15(counter15,1)=y(che,1);
        z15(counter15,1)=z(che,1);
        AZI15(counter15,1)=AZI(che,1);
        Date15(counter15,1)=Date(che,1);
        Time15(counter15,1)=Time(che,1);
        Density15(counter15,1)=Density(che,1);
        MaxAZI15(counter15,1)=MaxAZI(che,1);
        minAZI15(counter15,1)=minAZI(che,1);
        MaxINC15(counter15,1)=MaxINC(che,1);
        minINC15(counter15,1)=minINC(che,1);
        MD15(counter15,1)=MD(che,1);
        Moment15(counter15,1)=Moment(che,1);
        Angle15(counter15,1)=Angle(che,1);
        Reliability15(counter15,1)=Reliability(che,1);
        VertDis15(counter15,1)=VertDis(che,1);
        counter15=counter15+1;
case 18
        xo=2029687.97;
        yo=529194.04;
Distance(che,1)=((x(che,1)-xo)^2+(y(che,1)-yo)^2+(z(che,1)-zo)^2)^.5;
EUC18(counter18)=EUC(che);
```

```
        Dist18(counter18)=Distance(che);
        Stage18(counter18)=StageC(che);
        x18(counter18,1)=x(che,1);
        y18(counter18,1)=y(che,1);
        z18(counter18,1)=z(che,1);
        AZI18(counter18,1)=AZI(che,1);
        Date18(counter18,1)=Date(che,1);
        Time18(counter18,1)=Time(che,1);
        Density18(counter18,1)=Density(che,1);
        MaxAZI18(counter18,1)=MaxAZI(che,1);
        minAZI18(counter18,1)=minAZI(che,1);
        MaxINC18(counter18,1)=MaxINC(che,1);
        minINC18(counter18,1)=minINC(che,1);
        MD18(counter18,1)=MD(che,1);
        Moment18(counter18,1)=Moment(che,1);
        Angle18(counter18,1)=Angle(che,1);
        Reliability18(counter18,1)=Reliability(che,1);
        VertDis18(counter18,1)=VertDis(che,1);
        counter18=counter18+1;
case 30
        xo=2042872.97;
        yo=533326.04;
Distance(che,1)=((x(che,1)-xo)^2+(y(che,1)-yo)^2+(z(che,1)-zo)^2)^.5;
EUC30(counter30)=EUC(che);
        Dist30(counter30)=Distance(che);
        Stage30(counter30)=StageC(che);
        x30(counter30,1)=x(che,1);
        y30(counter30,1)=y(che,1);
        z30(counter30,1)=z(che,1);
        AZI30(counter30,1)=AZI(che,1);
        Date30(counter30,1)=Date(che,1);
        Time30(counter30,1)=Time(che,1);
        Density30(counter30,1)=Density(che,1);
        MaxAZI30(counter30,1)=MaxAZI(che,1);
        minAZI30(counter30,1)=minAZI(che,1);
        MaxINC30(counter30,1)=MaxINC(che,1);
        minINC30(counter30,1)=minINC(che,1);
        MD30(counter30,1)=MD(che,1);
        Moment30(counter30,1)=Moment(che,1);
        Angle30(counter30,1)=Angle(che,1);
        Reliability30(counter30,1)=Reliability(che,1);
        VertDis30(counter30,1)=VertDis(che,1);
        counter30=counter30+1;
case 115
        xo=2050452.01;
        yo=540731.15;
Distance(che,1)=((x(che,1)-xo)^2+(y(che,1)-yo)^2+(z(che,1)-zo)^2)^.5;
EUC115(counter115)=EUC(che);
        Dist115(counter115)=Distance(che);
        Stage115(counter115)=StageC(che);
        x115(counter115,1)=x(che,1);
        y115(counter115,1)=y(che,1);
        z115(counter115,1)=z(che,1);
        AZI115(counter115,1)=AZI(che,1);
        Date115(counter115,1)=Date(che,1);
        Time115(counter115,1)=Time(che,1);
```

```
        Density115(counter115,1)=Density(che,1);
        MaxAZI115(counter115,1)=MaxAZI(che,1);
        minAZI115(counter115,1)=minAZI(che,1);
        MaxINC115(counter115,1)=MaxINC(che,1);
        minINC115(counter115,1)=minINC(che,1);
        MD115(counter115,1)=MD(che,1);
        Moment115(counter115,1)=Moment(che,1);
        Angle115(counter115,1)=Angle(che,1);
        Reliability115(counter115,1)=Reliability(che,1);
        VertDis115(counter115,1)=VertDis(che,1);
        counter115=counter115+1;
case 116
        xo=2049618.18;
        yo=539055.96;
Distance(che,1)=((x(che,1)-xo)^2+(y(che,1)-yo)^2+(z(che,1)-zo)^2)^.5;
EUC116(counter116)=EUC(che);
        Dist116(counter116)=Distance(che);
        Stage116(counter116)=StageC(che);
        x116(counter116,1)=x(che,1);
        y116(counter116,1)=y(che,1);
        z116(counter116,1)=z(che,1);
        AZI116(counter116,1)=AZI(che,1);
        Date116(counter116,1)=Date(che,1);
        Time116(counter116,1)=Time(che,1);
        Density116(counter116,1)=Density(che,1);
        MaxAZI116(counter116,1)=MaxAZI(che,1);
        minAZI116(counter116,1)=minAZI(che,1);
        MaxINC116(counter116,1)=MaxINC(che,1);
        minINC116(counter116,1)=minINC(che,1);
        MD116(counter116,1)=MD(che,1);
        Moment116(counter116,1)=Moment(che,1);
        Angle116(counter116,1)=Angle(che,1);
        Reliability116(counter116,1)=Reliability(che,1);
        VertDis116(counter116,1)=VertDis(che,1);
        counter116=counter116+1;
case 121
        xo=2050452.01;
        yo=540731.15;
Distance(che,1)=((x(che,1)-xo)^2+(y(che,1)-yo)^2+(z(che,1)-zo)^2)^.5;
EUC121(counter121)=EUC(che);
        Dist121(counter121)=Distance(che);
        Stage121(counter121)=StageC(che);
        x121(counter121,1)=x(che,1);
        y121(counter121,1)=y(che,1);
        z121(counter121,1)=z(che,1);
        AZI121(counter121,1)=AZI(che,1);
        Date121(counter121,1)=Date(che,1);
        Time121(counter121,1)=Time(che,1);
        Density121(counter121,1)=Density(che,1);
        MaxAZI121(counter121,1)=MaxAZI(che,1);
        minAZI121(counter121,1)=minAZI(che,1);
        MaxINC121(counter121,1)=MaxINC(che,1);
        minINC121(counter121,1)=minINC(che,1);
        MD121(counter121,1)=MD(che,1);
        Moment121(counter121,1)=Moment(che,1);
        Angle121(counter121,1)=Angle(che,1);
```

```
        Reliability121(counter121,1)=Reliability(che,1);
        VertDis121(counter121,1)=VertDis(che,1);
        counter121=counter121+1;
case 126
        xo=2049618.18;
        yo=539055.96;
Distance(che,1)=((x(che,1)-xo)^2+(y(che,1)-yo)^2+(z(che,1)-zo)^2)^.5;
EUC126(counter126)=EUC(che);
        Dist126(counter126)=Distance(che);
        Stage126(counter126)=StageC(che);
        x126(counter126,1)=x(che,1);
        y126(counter126,1)=y(che,1);
        z126(counter126,1)=z(che,1);
        AZI126(counter126,1)=AZI(che,1);
        Date126(counter126,1)=Date(che,1);
        Time126(counter126,1)=Time(che,1);
        Density126(counter126,1)=Density(che,1);
        MaxAZI126(counter126,1)=MaxAZI(che,1);
        minAZI126(counter126,1)=minAZI(che,1);
        MaxINC126(counter126,1)=MaxINC(che,1);
        minINC126(counter126,1)=minINC(che,1);
        MD126(counter126,1)=MD(che,1);
        Moment126(counter126,1)=Moment(che,1);
        Angle126(counter126,1)=Angle(che,1);
        Reliability126(counter126,1)=Reliability(che,1);
        VertDis126(counter126,1)=VertDis(che,1);
        counter126=counter126+1;
case 258
        xo=2018025.66;
        yo=519275.17;
Distance(che,1)=((x(che,1)-xo)^2+(y(che,1)-yo)^2+(z(che,1)-zo)^2)^.5;
EUC258(counter258)=EUC(che);
        Dist258(counter258)=Distance(che);
        Stage258(counter258)=StageC(che);
        x258(counter258,1)=x(che,1);
        y258(counter258,1)=y(che,1);
        z258(counter258,1)=z(che,1);
        AZI258(counter258,1)=AZI(che,1);
        Date258(counter258,1)=Date(che,1);
        Time258(counter258,1)=Time(che,1);
        Density258(counter258,1)=Density(che,1);
        MaxAZI258(counter258,1)=MaxAZI(che,1);
        minAZI258(counter258,1)=minAZI(che,1);
        MaxINC258(counter258,1)=MaxINC(che,1);
        minINC258(counter258,1)=minINC(che,1);
        MD258(counter258,1)=MD(che,1);
        Moment258(counter258,1)=Moment(che,1);
        Angle258(counter258,1)=Angle(che,1);
        Reliability258(counter258,1)=Reliability(che,1);
        VertDis258(counter258,1)=VertDis(che,1);
        counter258=counter258+1;
case 259
        xo=2018772.81;
        yo=518917.61;
Distance(che,1)=((x(che,1)-xo)^2+(y(che,1)-yo)^2+(z(che,1)-zo)^2)^.5;
EUC259(counter259)=EUC(che);
```

```
            Dist259(counter259)=Distance(che);
            Stage259(counter259)=StageC(che);
            x259(counter259,1)=x(che,1);
            y259(counter259,1)=y(che,1);
            z259(counter259,1)=z(che,1);
            AZI259(counter259,1)=AZI(che,1);
            Date259(counter259,1)=Date(che,1);
            Time259(counter259,1)=Time(che,1);
            Density259(counter259,1)=Density(che,1);
            MaxAZI259(counter259,1)=MaxAZI(che,1);
            minAZI259(counter259,1)=minAZI(che,1);
            MaxINC259(counter259,1)=MaxINC(che,1);
            minINC259(counter259,1)=minINC(che,1);
            MD259(counter259,1)=MD(che,1);
            Moment259(counter259,1)=Moment(che,1);
            Angle259(counter259,1)=Angle(che,1);
            Reliability259(counter259,1)=Reliability(che,1);
            VertDis259(counter259,1)=VertDis(che,1);
            counter259=counter259+1;
otherwise
            warning('The data corresponding to this well is not recorded');
end
end
EUCN = (EUC - min(EUC)+1)*10;
n=1;
if counter3 >1
    EUCN3 = (EUC3 - min(EUC3)+1)*10;
    figure(n)
    scatter(Dist3,EUC3,EUCN3,Stage3,'filled');
    xlabel('Distance (ft.)')
    ylabel ('Moment Magnitude')
    title ('Distance Vs Moment Magnitude (Well H3)')
    colorbar
    n=n+1;
else
    warning('The microseismic Magnitudes corresponding to Well H3 were not recorded');
end
%
if counter10 > 1
    EUCN10 = (EUC10 - min(EUC10)+1)*10;
    figure(n)
    scatter(Dist10,EUC10,EUCN10,Stage10,'filled');
    n=n+1;
else
    warning('The microseismic Magnitudes corresponding to Well H10 were not recorded');
end
if counter15 >1
    EUCN15 = (EUC15 - min(EUC15)+1)*10;
    figure(n)
    scatter(Dist15,EUC15,EUCN15,Stage15,'filled');
    xlabel('Distance (ft.)')
    ylabel ('Moment Magnitude')
    title ('Distance Vs Moment Magnitude(Well H15)')
    colorbar
    n=n+1;
else
```

```
    warning('The microseismic Magnitudes corresponding to Well H15 were not recorded');
end
if counter18 >1
    EUCN18 = (EUC18 - min(EUC18)+1)*10;
    figure(n)
    scatter(Dist18,EUC18,EUCN18,Stage18,'filled');
    xlabel('Distance (ft.)')
    ylabel ('Moment Magnitude')
    title ('Distance Vs Moment Magnitude(Well H18)')
    colorbar
    n=n+1;
else
    warning('The microseismic Magnitudes corresponding to Well H18 were not recorded');
end
if counter30>1
    EUCN30 = (EUC30 - min(EUC30)+1)*10;
    figure(n)
    scatter(Dist30,EUC30,EUCN30,Stage30,'filled');
    xlabel('Distance (ft.)')
    ylabel ('Moment Magnitude')
    title ('Distance Vs Moment Magnitude(Well H30)')
    colorbar
    n=n+1;
else
    warning('The microseismic Magnitudes corresponding to Well H30 were not recorded');
end
if counter115>1
    EUCN115 = (EUC115 - min(EUC115)+1)*10;
    figure(n)
    scatter(Dist115,EUC115,EUCN115,Stage115,'filled');
    xlabel('Distance (ft.)')
    ylabel ('Moment Magnitude')
    title ('Distance Vs Moment Magnitude(Well H115)')
    colorbar
    n=n+1;
else
    warning('The microseismic Magnitudes corresponding to Well H115 were not recorded');
end
if counter116>1
    EUCN116 = (EUC116 - min(EUC116)+1)*10;
    figure(n)
    scatter(Dist116,EUC116,EUCN116,Stage116,'filled');
    xlabel('Distance (ft.)')
    ylabel ('Moment Magnitude')
    title ('Distance Vs Moment Magnitude(Well H116)')
    colorbar
    n=n+1;
else
    warning('The microseismic Magnitudes corresponding to Well H116 were not recorded');
end
if counter121>1
    EUCN121 = (EUC121 - min(EUC121)+1)*10;
    figure(n)
    scatter(Dist121,EUC121,EUCN121,Stage121,'filled');
    xlabel('Distance (ft.)')
    ylabel ('Moment Magnitude')
```

```
    title ('Distance Vs Moment Magnitude(Well H121)')
    colorbar
    n=n+1;
else
    warning('The microseismic Magnitudes corresponding to Well H121 were not recorded');
end
if counter126>1
    EUCN126 = (EUC126 - min(EUC126)+1)*10;
    figure(n)
    scatter(Dist126,EUC126,EUCN126,Stage126,'filled');
    xlabel('Distance (ft.)')
    ylabel ('Moment Magnitude')
    title ('Distance Vs Moment Magnitude(Well H126)')
    colorbar
    n=n+1;
else
    warning('The microseismic Magnitudes corresponding to Well H126 were not recorded');
end
if counter258>1
    EUCN258 = (EUC258 - min(EUC258)+1)*10;
    figure(n)
    scatter(Dist258,EUC258,EUCN258,Stage258,'filled');
    xlabel('Distance (ft.)')
    ylabel ('Moment Magnitude')
    title ('Distance Vs Moment Magnitude(Well V258)')
    colorbar
    n=n+1;
else
    warning('The microseismic Magnitudes corresponding to Well V258 were not recorded');
end
if counter259>1
    EUCN259 = (EUC259 - min(EUC259)+1)*10;
    figure(n)
    scatter(Dist259,EUC259,EUCN259,Stage259,'filled');
    xlabel('Distance (ft.)')
    ylabel ('Moment Magnitude')
    title ('Distance Vs Moment Magnitude(Well V259)')
    colorbar
    n=n+1;
else
    warning('The microseismic Magnitudes corresponding to Well V259 were not recorded');
end
```

Removing data below the viewing limit

This portion of the code removes the microseismic events whose magnitudes are below the viewing limit determined independently for each stimulated well. The viewing limit is determined as the smallest event that can be detected at the farthest point from the monitor array.

```
n=11;
if counter3>1
	Lim=find(EUC3>-1.9);  %Gets the index of values in EUC3 greater than -1.9
	EUC3=EUC3(Lim);       %discards entries of EUC3 that are smaller than or equal to -1.9
	EUCN3=EUCN3(Lim);
	Dist3=Dist3(Lim);
	Stage3=Stage3(Lim);
	x3=x3(Lim);
y3=y3(Lim);
	z3=z3(Lim);
AZI3=AZI3(Lim);
	Date3=Date3(Lim);
	Date3=Date3-datenum('30-Dec-1899');
	Time3=Time3(Lim);
	Density3=Density3(Lim);
	MaxAZI3=MaxAZI3(Lim);
	minAZI3=minAZI3(Lim);
	MaxINC3=MaxINC3(Lim);
	minINC3=minINC3(Lim);
	MD3=MD3(Lim);
	Moment3=Moment3(Lim);
	Angle3=Angle3(Lim);
	Reliability3=Reliability3(Lim);
	VertDis3=VertDis3(Lim);
	counter3=size(Lim,2);
	figure(n)
	scatter(Dist3,EUC3,EUCN3,Stage3,'filled');
	xlabel('Distance (ft.)')
	ylabel ('Moment Magnitude')
	title ('Distance Vs Moment Magnitude (Well H3)')
	colorbar
	n=n+1;
else
	warning('The microseismic Magnitudes corresponding to Well H3 were not recorded');
end
if counter10>1
	Lim=find(EUC10>-1.9);
	EUC10=EUC10(Lim);
	EUCN10=EUCN10(Lim);
	Dist10=Dist10(Lim);
	Stage10=Stage10(Lim);
x10=x10(Lim);
	y10=y10(Lim);
z10=z10(Lim);
	AZI10=AZI10(Lim);
	Date10=Date10(Lim);
	Date10=Date10-datenum('30-Dec-1899');
	Time10=Time10(Lim);
	Density10=Density10(Lim);
	MaxAZI10=MaxAZI10(Lim);
	minAZI10=minAZI10(Lim);
	MaxINC10=MaxINC10(Lim);
	minINC10=minINC10(Lim);
	MD10=MD10(Lim);
	Moment10=Moment10(Lim);
	Angle10=Angle10(Lim);
```

```
        Reliability10=Reliability10(Lim);
        VertDis10=VertDis10(Lim);
        counter10=size(Lim,2);
        figure(n)
        scatter(Dist10,EUC10,EUCN10,Stage10,'filled');
        n=n+1;
else
        warning('The microseismic Magnitudes corresponding to Well H10 were not recorded');
end
if counter15>1
        Lim=find(EUC15>-1.9);
        EUC15=EUC15(Lim);
        EUCN15=EUCN15(Lim);
        Dist15=Dist15(Lim);
        Stage15=Stage15(Lim);
x15=x15(Lim);
        y15=y15(Lim);
z15=z15(Lim);
        AZI15=AZI15(Lim);
        Date15=Date15(Lim);
        Date15=Date15-datenum('30-Dec-1899');
        Time15=Time15(Lim);
        Density15=Density15(Lim);
        MaxAZI15=MaxAZI15(Lim);
        minAZI15=minAZI15(Lim);
        MaxINC15=MaxINC15(Lim);
        minINC15=minINC15(Lim);
        MD15=MD15(Lim);
        Moment15=Moment15(Lim);
        Angle15=Angle15(Lim);
        Reliability15=Reliability15(Lim);
        VertDis15=VertDis15(Lim);
        counter15=size(Lim,2);
        figure(n)
        scatter(Dist15,EUC15,EUCN15,Stage15,'filled');
        xlabel('Distance (ft.)')
        ylabel ('Moment Magnitude')
        title ('Distance Vs Moment Magnitude(Well H15)')
        colorbar
        n=n+1;
else
        warning('The microseismic Magnitudes corresponding to Well H15 were not recorded');
end
if counter18>1
        Lim=find(EUC18>-1.8);
        EUC18=EUC18(Lim);
        EUCN18=EUCN18(Lim);
        Dist18=Dist18(Lim);
        Stage18=Stage18(Lim);
x18=x18(Lim);
        y18=y18(Lim);
z18=z18(Lim);
        AZI18=AZI18(Lim);
        Date18=Date18(Lim);
        Date18=Date18-datenum('30-Dec-1899');
        Time18=Time18(Lim);
```

```
        Density18=Density18(Lim);
        MaxAZI18=MaxAZI18(Lim);
        minAZI18=minAZI18(Lim);
        MaxINC18=MaxINC18(Lim);
        minINC18=minINC18(Lim);
        MD18=MD18(Lim);
        Moment18=Moment18(Lim);
        Angle18=Angle18(Lim);
        Reliability18=Reliability18(Lim);
        VertDis18=VertDis18(Lim);
        counter18=size(Lim,2);
        figure(n)
        scatter(Dist18,EUC18,EUCN18,Stage18,'filled');
        xlabel('Distance (ft.)')
        ylabel ('Moment Magnitude')
        title ('Distance Vs Moment Magnitude(Well H18)')
        colorbar
        n=n+1;
else
        warning('The microseismic Magnitudes corresponding to Well H18 were not recorded');
end
if counter30>1
        Lim=find(EUC30>-1.9);
        EUC30=EUC30(Lim);
        EUCN30=EUCN30(Lim);
        Dist30=Dist30(Lim);
        Stage30=Stage30(Lim);
x30=x30(Lim);
        y30=y30(Lim);
z30=z30(Lim);
        AZI30=AZI30(Lim);
        Date30=Date30(Lim);
        Date30=Date30-datenum('30-Dec-1899');
        Time30=Time30(Lim);
        Density30=Density30(Lim);
        MaxAZI30=MaxAZI30(Lim);
        minAZI30=minAZI30(Lim);
        MaxINC30=MaxINC30(Lim);
        minINC30=minINC30(Lim);
        MD30=MD30(Lim);
        Moment30=Moment30(Lim);
        Angle30=Angle30(Lim);
        Reliability30=Reliability30(Lim);
        VertDis30=VertDis30(Lim);
        counter30=size(Lim,2);
        figure(n)
        scatter(Dist30,EUC30,EUCN30,Stage30,'filled');
        xlabel('Distance (ft.)')
        ylabel ('Moment Magnitude')
        title ('Distance Vs Moment Magnitude(Well H30)')
        colorbar
        n=n+1;
else
        warning('The microseismic Magnitudes corresponding to Well H30 were not recorded');
end
if counter115>1
```

```
        Lim=find(EUC115>-2.7);
        EUC115=EUC115(Lim);
        EUCN115=EUCN115(Lim);
        Dist115=Dist115(Lim);
        Stage115=Stage115(Lim);
x115=x115(Lim);
        y115=y115(Lim);
z115=z115(Lim);
        AZI115=AZI115(Lim);
        Date115=Date115(Lim);
        Date115=Date115-datenum('30-Dec-1899');
        Time115=Time115(Lim);
        Density115=Density115(Lim);
        MaxAZI115=MaxAZI115(Lim);
        minAZI115=minAZI115(Lim);
        MaxINC115=MaxINC115(Lim);
        minINC115=minINC115(Lim);
        MD115=MD115(Lim);
        Moment115=Moment115(Lim);
        Angle115=Angle115(Lim);
        Reliability115=Reliability115(Lim);
        VertDis115=VertDis115(Lim);
        counter115=size(Lim,2);
        figure(n)
        scatter(Dist115,EUC115,EUCN115,Stage115,'filled');
        xlabel('Distance (ft.)')
        ylabel ('Moment Magnitude')
        title ('Distance Vs Moment Magnitude(Well H115)')
        colorbar
        n=n+1;
else
        warning('The microseismic Magnitudes corresponding to Well H115 were not recorded');
end
if counter116>1
        Lim=find(EUC116>-2.7);
        EUC116=EUC116(Lim);
        EUCN116=EUCN116(Lim);
        Dist116=Dist116(Lim);
        Stage116=Stage116(Lim);
x116=x116(Lim);
        y116=y116(Lim);
z116=z116(Lim);
        AZI116=AZI116(Lim);
        Date116=Date116(Lim);
        Date116=Date116-datenum('30-Dec-1899');
        Time116=Time116(Lim);
        Density116=Density116(Lim);
        MaxAZI116=MaxAZI116(Lim);
        minAZI116=minAZI116(Lim);
        MaxINC116=MaxINC116(Lim);
        minINC116=minINC116(Lim);
        MD116=MD116(Lim);
        Moment116=Moment116(Lim);
        Angle116=Angle116(Lim);
        Reliability116=Reliability116(Lim);
        VertDis116=VertDis116(Lim);
```

```
        counter116=size(Lim,2);
        figure(n)
        scatter(Dist116,EUC116,EUCN116,Stage116,'filled');
        xlabel('Distance (ft.)')
        ylabel ('Moment Magnitude')
        title ('Distance Vs Moment Magnitude(Well H116)')
        colorbar
        n=n+1;
else
        warning('The microseismic Magnitudes corresponding to Well H116 were not recorded');
end
%case 121
if counter121>1
        Lim=find(EUC121>-2.7);
        EUC121=EUC121(Lim);
        EUCN121=EUCN121(Lim);
        Dist121=Dist121(Lim);
        Stage121=Stage121(Lim);
x121=x121(Lim);
        y121=y121(Lim);
z121=z121(Lim);
        AZI121=AZI121(Lim);
        Date121=Date121(Lim);
        Date121=Date121-datenum('30-Dec-1899');
        Time121=Time121(Lim);
        Density121=Density121(Lim);
        MaxAZI121=MaxAZI121(Lim);
        minAZI121=minAZI121(Lim);
        MaxINC121=MaxINC121(Lim);
        minINC121=minINC121(Lim);
        MD121=MD121(Lim);
        Moment121=Moment121(Lim);
        Angle121=Angle121(Lim);
        Reliability121=Reliability121(Lim);
        VertDis121=VertDis121(Lim);
        counter121=size(Lim,2);
        figure(n)
        scatter(Dist121,EUC121,EUCN121,Stage121,'filled');
        xlabel('Distance (ft.)')
        ylabel ('Moment Magnitude')
        title ('Distance Vs Moment Magnitude(Well H121)')
        colorbar
        n=n+1;
else
        warning('The microseismic Magnitudes corresponding to Well H121 were not recorded');
end
%case 126
if counter126>1
        Lim=find(EUC126>-2.8);
        EUC126=EUC126(Lim);
        EUCN126=EUCN126(Lim);
        Dist126=Dist126(Lim);
        Stage126=Stage126(Lim);
x126=x126(Lim);
        y126=y126(Lim);
z126=z126(Lim);
```

```
        AZI126=AZI126(Lim);
        Date126=Date126(Lim);
        Date126=Date126-datenum('30-Dec-1899');
        Time126=Time126(Lim);
        Density126=Density126(Lim);
        MaxAZI126=MaxAZI126(Lim);
        minAZI126=minAZI126(Lim);
        MaxINC126=MaxINC126(Lim);
        minINC126=minINC126(Lim);
        MD126=MD126(Lim);
        Moment126=Moment126(Lim);
        Angle126=Angle126(Lim);
        Reliability126=Reliability126(Lim);
        VertDis126=VertDis126(Lim);
        counter126=size(Lim,2);
        figure(n)
        scatter(Dist126,EUC126,EUCN126,Stage126,'filled');
        xlabel('Distance (ft.)')
        ylabel ('Moment Magnitude')
        title ('Distance Vs Moment Magnitude(Well H126)')
        colorbar
        n=n+1;
else
        warning('The microseismic Magnitudes corresponding to Well H126 were not recorded');
end
if counter258>1
        Lim=find(EUC258>-2.1);
        EUC258=EUC258(Lim);
        EUCN258=EUCN258(Lim);
        Dist258=Dist258(Lim);
        Stage258=Stage258(Lim);
x258=x258(Lim);
        y258=y258(Lim);
z258=z258(Lim);
        AZI258=AZI258(Lim);
        Date258=Date258(Lim);
        Date258=Date258-datenum('30-Dec-1899');
        Time258=Time258(Lim);
        Density258=Density258(Lim);
        MaxAZI258=MaxAZI258(Lim);
        minAZI258=minAZI258(Lim);
        MaxINC258=MaxINC258(Lim);
        minINC258=minINC258(Lim);
        MD258=MD258(Lim);
        Moment258=Moment258(Lim);
        Angle258=Angle258(Lim);
        Reliability258=Reliability258(Lim);
        VertDis258=VertDis258(Lim);
        counter258=size(Lim,2);
        figure(n)
        scatter(Dist258,EUC258,EUCN258,Stage258,'filled');
        xlabel('Distance (ft.)')
        ylabel ('Moment Magnitude')
        title ('Distance Vs Moment Magnitude(Well V258)')
        colorbar
        n=n+1;
```

```
else
	warning('The microseismic Magnitudes corresponding to Well V258 were not recorded');
end
%case 259
if counter259>1
	Lim=find(EUC259>-1.5);
	EUC259=EUC259(Lim);
	EUCN259=EUCN259(Lim);
	Dist259=Dist259(Lim);
	Stage259=Stage259(Lim);
x259=x259(Lim);
	y259=y259(Lim);
z259=z259(Lim);
	AZI259=AZI259(Lim);
	Date259=Date259(Lim);
	Date259=Date259-datenum('30-Dec-1899');
	Time259=Time259(Lim);
	Density259=Density259(Lim);
	MaxAZI259=MaxAZI259(Lim);
	minAZI259=minAZI259(Lim);
	MaxINC259=MaxINC259(Lim);
	minINC259=minINC259(Lim);
	MD259=MD259(Lim);
	Moment259=Moment259(Lim);
	Angle259=Angle259(Lim);
	Reliability259=Reliability259(Lim);
	VertDis259=VertDis259(Lim);
	counter259=size(Lim,2);
	figure(n)
	scatter(Dist259,EUC259,EUCN259,Stage259,'filled');
	xlabel('Distance (ft.)')
	ylabel ('Moment Magnitude')
	title ('Distance Vs Moment Magnitude(Well V259)')
	colorbar
	n=n+1;
else
	warning('The microseismic Magnitudes corresponding to Well V259 were not recorded');
end
Total=counter3+counter15+counter18+counter115 ...
+counter116+counter121+counter126+counter258+counter259;

g = ksdensity(Density,'weights',Reliability);
```

Appendix A3: Exporting the Data

This subroutine, saved under the name “expordata.m”, creates the file “'Microseismic_filtered.xlsb” and exports the filtered data to this Excel binary file. It writes the information corresponding to each well into a different tab in the file. The following code can be run in MATLAB® 7.12.

```
WELL_H3 = [Stage3',Density3,Date3,Time3,z3,x3,y3,Moment3,VertDis3,AZI3,...
    EUC3',MaxAZI3,MaxINC3,MD3,minAZI3,minINC3,Angle3,Reliability3];
xlswrite('Microseismic_filtered.xlsb', WELL_H3, 'WELL H3', 'A1');
WELL_H15 = [Stage15',Density15,Date15,Time15,z15,x15,y15,Moment15,...
    VertDis15,AZI15,EUC15',MaxAZI15,MaxINC15,MD15,minAZI15,minINC15,...
    Angle15,Reliability15];
xlswrite('Microseismic_filtered.xlsb', WELL_H15, 'WELL H15', 'A1');
WELL_H18 = [Stage18',Density18,Date18,Time18,z18,x18,y18,Moment18,...
    VertDis18,AZI18,EUC18',MaxAZI18,MaxINC18,MD18,minAZI18,minINC18,...
    Angle18,Reliability18];
xlswrite('Microseismic_filtered.xlsb', WELL_H18, 'WELL H18', 'A1');
WELL_H115 = [Stage115',Density115,Date115,Time115,z115,x115,y115,Moment115,...
    VertDis115,AZI115,EUC115',MaxAZI115,MaxINC115,MD115,minAZI115,...
    minINC115,Angle115,Reliability115];
xlswrite('Microseismic_filtered.xlsb', WELL_H115, 'WELL H115', 'A1');
WELL_H116 = [Stage116',Density116,Date116,Time116,z116,x116,y116,Moment116,...
    VertDis116,AZI116,EUC116',MaxAZI116,MaxINC116,MD116,minAZI116,...
    minINC116,Angle116,Reliability116];
xlswrite('Microseismic_filtered.xlsb', WELL_H116, 'WELL H116', 'A1');
WELL_H121 = [Stage121',Density121,Date121,Time121,z121,x121,y121,Moment121,...
    VertDis121,AZI121,EUC121',MaxAZI121,MaxINC121,MD121,minAZI121,...
    minINC121,Angle121,Reliability121];
xlswrite('Microseismic_filtered.xlsb', WELL_H121, 'WELL H121', 'A1');
WELL_H126 = [Stage126',Density126,Date126,Time126,z126,x126,y126,Moment126,...
    VertDis126,AZI126,EUC126',MaxAZI126,MaxINC126,MD126,minAZI126,...
    minINC126,Angle126,Reliability126];
xlswrite('Microseismic_filtered.xlsb', WELL_H126, 'WELL H126', 'A1');
WELL_V258 = [Stage258',Density258,Date258,Time258,z258,x258,y258,Moment258,...
    VertDis258,AZI258,EUC258',MaxAZI258,MaxINC258,MD258,minAZI258,...
    minINC258,Angle258,Reliability258];
xlswrite('Microseismic_filtered.xlsb', WELL_V258, 'WELL V258', 'A1');
WELL_V259 = [Stage259',Density259,Date259,Time259,z259,x259,y259,Moment259,...
    VertDis259,AZI259,EUC259',MaxAZI259,MaxINC259,MD259,minAZI259,...
    minINC259,Angle259,Reliability259];
xlswrite('Microseismic_filtered.xlsb', WELL_V259, 'WELL V258', 'A1');
```

Appendix B: Geologic Time Scale

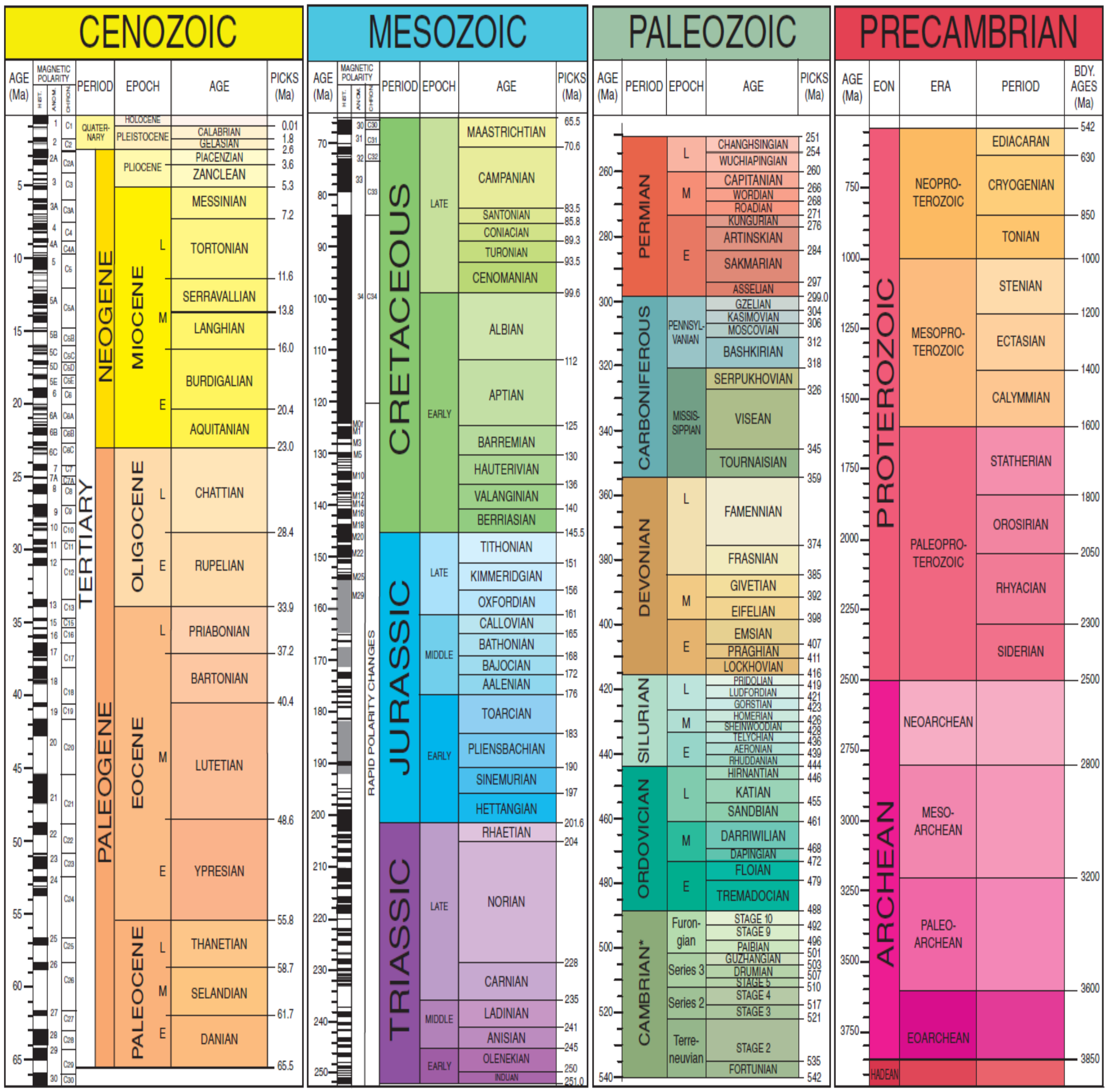

Figure 60. Geologic Time Scale: The Geological Society of America. Walkerand Geissman (2009).